DEXTRIN NANOCOMPOSITES AND DEEP EUTECTIC SOLVENTS AS MATRICES FOR SOLID DOSAGE FORMS

Justin Phillips

Dextrin nanocomposites and deep eutectic solvents as matrices for solid dosage forms

by

Justin Phillips

A dissertation submitted in partial fulfillment
of the requirements of the degree

Master of Engineering (Chemical Engineering)

in the

Department of Chemical Engineering
Faculty of Engineering, the Built Environment
and Information Technology

University of Pretoria

April 2020

Dextrin nanocomposites and deep eutectic solvents as matrices for solid dosage forms

Abstract

Controlled-release formulations for pesticide applications act as depot systems that continuously release the active ingredients into the environment over a specified period, usually from months to years. However, some applications require fast-dissolving drug delivery. The interest of this research is in fast-release of water-insoluble pesticides into aquatic environments. This study considered the use of dextrin starch and urea eutectics as fast release, solid dosage carrier forms that contain an active ingredient. The chosen active for this study is an acaricide called amitraz (N-methylbis-(2,4-xylyliminomethyl)-methylamine). The focus is on matrix-based dosage forms such as tablets, granules or fibres that either disintegrate or dissolve to release a water-insoluble active. These types of dosage forms can be fabricated using processes such as lyophilisation, spray drying, solvent casting, hot melt extrusion, compression moulding, wet granulation, compaction and electrospinning. A simple melt-casting procedure has been discussed in the present work.

Dextrin is a water-soluble form of partially hydrolysed starch and is a promising candidate matrix material for dissolving solid dosage forms. The molecular weight of the dextrin was analysed with MALDI-TOF methods and rheological relations. Glycerol-plasticized thermoplastic dextrin-based nanocomposites were prepared with a twin-screw extrusion-compounding process. The nanofillers included a layered double hydroxide (LDH), cellulose nanofibres (CNF) and stearic acid. The time-dependent retrogradation of the compounds was monitored by X-ray diffraction (XRD) and dynamic mechanical thermal analysis (DMA). XRD showed that the inclusion of stearic acid in the formulations led to the formation of an amylose-lipid complex and a stable crystallinity during ageing.

Dissolution rates in water for samples containing dextrin starch, were characterised using an iodine indicator and UV-visible spectroscopy. High pressure differential scanning calorimetry (HPDSC) indicated that the addition of stearic acid led to the formation of amylose-lipid complexes (ALC's). An additive system containing stearic acid and CNF was deemed suitable for compounding with amitraz. Compounding at temperatures above the melting point of the latter led, on dissolution in water, to the release of much finer particles of the acaricide, which was confirmed with particle size analysis (PSA).

The addition of the acaricide caused an apparent increase in the dissolution rate of the thermoplastic dextrin.

Two eutectic urea systems were considered for casting with amitraz. A eutectic system of urea and acetamide was found to display a melting point of 44 °C at a 37 wt.% urea composition. The other system consisting of urea and 1,3-dimethylurea displayed a eutectic point at 32 wt.% urea composition which melted at 59 °C. Differential scanning calorimetry (DSC), however, confirmed a melting point depression due to a high moisture content caused by the compounds high hygroscopicity. The endotherm of the sample containing no excess moisture showed a melting point of 70 °C. The 1,3-dimethylurea system was deemed suitable for casting with amitraz. XRD of the eutectic composition indicated a small amount of co-crystallisation. The samples were cast as disks of various diameters while keeping the height of the disks constant. The creation of the cast disks showed automatic generation of a finely dispersed form of the active through the process of melting the deep eutectic solvent, the dissolution of the active and its phase separation on cooling and solidification of the eutectic. This implies that fine grinding of the actives might not be necessary. Eutectic casts containing 20 wt.% amitraz dissolved at a slower rate than casts not containing the hydrophobic active ingredient. The advantageous features of these casts were exemplified using the acaricide incorporated into the urea & 1,3-dimethylurea eutectic.

This work provides two safe, biodegradable and water soluble materials for use as a matrix to contain active ingredients. One material, the eutectic organic salt casts, can be produced at low temperatures (<100 °C) and can be directly cast into storage containers. The complete dissolution of the cast compounded with a hydrophilic active is rapid (4-6 min). The second material, a thermoplastic dextrin, was melt compounded in an extruder at temperatures not exceeding 120 °C. This compound containing 20 wt.% of the active dissolved over a 12 hour period. Dextrin, known to be widely used as an adhesive, will aid in the adhesion of the active ingredient to the surface where it must be used.

Keywords: starch, dextrin, amitraz, acaricide, solid dosage form, cellulose nanofibres, layered double hydroxide

Acknowledgements

I'm deeply indebted to my parents and sister for their unwavering love and encouragement. I am extremely grateful to my mentors, professor Walter Focke and Elizbé du Toit, for their insightful tuition and abundant aid. I would also like to extend my deepest gratitude to Jaco-Louis Venter, for his tireless work and loyalty as a friend and colleague. Thanks should also go to Michelle Weldhagen for her hard work and invaluable insights. I also had great pleasure of working with Hester Oosthuizen, Maria Atanasova, James-Wesley Smith and professor Naushad Emmambux. Financial support from PAMSA and the Department of Science and Innovation under Grant DST/CON 0004/2019 is gratefully acknowledged. I would also like to thank Jan Mentz and Greenfield Additives for kindly donating the hydrocalumite grade B44 sample, the layered double hydroxide (LDH) used in this study.

Work as hard as you possibly can on at least one thing and see what happens.

Jordan Peterson

You have power over your mind - not outside events. Realize this, and you will find strength.

Marcus Aurelius

Be more than you seem to be.

Frederick II von Hohenzollern

Contents

List of Figures

List of Tables

List of symbols and abbreviations

Variables

A_P	Porter interaction coefficient	-
A	Margules interaction coefficient	-
a	Mark Houwink exponent	-
C	Concentration	$kg{\cdot}m^{-3}$
c	Concentration of polymer in solution	$g{\cdot}dL^{-1}$
D	Diffusion coefficient	$m^2{\cdot}s^{-1}$
d	Diameter	m
d	Diameter	m
H	Enthalpy of fusion	$J{\cdot}mol^{-1}$
h	Dissolution film thickness	m
H°	Standard enthalpy of fusion	$J{\cdot}mol^{-1}$
K	Mark Houwink constant	$dL{\cdot}g^{-1}$
k	Cube root rate constant	$kg^{\frac{1}{3}}{\cdot}s^{-1}$
k	Cube root rate constant	$kg^{\frac{1}{3}}{\cdot}s^{-1}$
k	Cube root rate constant	$kg^{\frac{1}{3}}{\cdot}s^{-1}$
k'	Intrinsic rate constant	$m{\cdot}s^{-1}$
k'	Intrinsic rate constant	$m{\cdot}s^{-1}$
M	Undissolved particle mass	kg
M	Undissolved particle mass	kg
M	Undissolved particle mass	kg
m	Dissolved mass	kg
$\overline{m}$	Slope of Mark Houwink regression	$mm^2{\cdot}dL{\cdot}g^{-1}{\cdot}s^{-1}$
M_w	Molar mass	$g{\cdot}mol^{-1}$

N	Number of particles	-
ν_0	Kinematic viscosity of solvent	$mm^2 \cdot s^{-1}$
R	Ideal gas constant	$J \cdot mol^{-1} \cdot K^{-1}$
S	Surface area	m^2
T	Temperature	K
t	Time	s
t	Time	s
t	Time	s
T°	Melting temperature	K
U	Additive crystallinity constant	-
V	Volume	m^3
w	Mass fraction	%
X	Steady state crystallinity	%
x	Mol fraction	-

Greek Symbols

γ	Activity coefficient	
Λ	Wilson interaction coefficient	-
$[\eta]$	Intrinsic viscosity of polymer solution	$g \cdot dL^{-1}$
γ	Interaction coefficient	-
ν	Kinematic viscosity of polymer solution	$mm^2 \cdot s^{-1}$
ϕ	Inner diameter	m
π	Archimedes' constant	-
ρ	Density	$kg \cdot m^{-3}$

Selected Abbreviations

ALC	Amylose lipid complex

CNC Cellulose nanocrystals

CNF Cellulose nanofibre

DE Dextrose equivalent

ICDD International Center for Diffraction Data

LDH Layered double hydroxide

MCC Microcrystalline Cellulose

PDF Powder Diffraction File

RPM Revolutions Per Minute

TPD Thermoplastic dextrin

TPS Thermoplastic starch

UAE Urea & acetamide eutectic

UDE Urea & 1,3-dimetylurea eutectic

Subscripts

0 Initial amount

0 Initial amount

0 Initial amount

i Component i

j Component j -

S Solubility limit

SP Indicates a specific parameter

1 Introduction

Ectoparasites of domestic animals and their impact on human health and agricultural economies are well documented and considered to be vectors of some of the most prolific viral diseases worldwide (Benelli *et al.* 2019; Dobler, 2018; Porter, Norman & Gilbert, 2011; Magnarelli, 2009; Jongejan & Uilenberg, 2004). As the world population rises, especially in dense urban regions and growing economies, the need for a consistent and robust source of nutrition becomes increasingly important (Lobell *et al.* 2008; Castro & D'Agnes, 2008; Delgado, 2003; Pelletier *et al.* 1995). In particular, tropical and sub-tropical countries are prone to tick-borne diseases and their deleterious effects (Jongejan & Uilenberg, 2004).

Tick borne infections may cause Lyme disease, relapsing fever, many haemorrhagic fevers, babesiosis, a wide variety of cattle fevers, ehrlichiosis, tularemia and ecephalitis (Piesman & Eisen, 2008). These diseases are known to affect humans. Around five thousand to six thousand tick-borne fevers are reported in the United States of America annually (US Department of Health & Human Services, 2019b).

The treatment of parasites that place themselves on the surface of the skin of animals are often implemented via a dip method, where the animal is completely immersed by the insecticide or repellent solution (Piesman & Eisen, 2008; Jongejan & Uilenberg, 2004). The dip method chemicals have been largely scrutinised due to human health risks, potential resistance and environmental impact (Kunz & Kemp, 1994). These dangerous active compounds (arsenic, hexachloride and lindane) have been banned or are being banned in many countries (Hansen, 2013; Y Li *et al.* 2016). In the past two decades, these compounds have been replaced by safer organophosphates, carbamates, organochlorines and pyrethroids (Jongejan & Uilenberg, 2004). These pesticides however are also known to be harmful to wildlife and many domestic species if used irresponsibly (Kunz & Kemp, 1994).

Several regulations have been implemented to ensure the correct and safe use of the active ingredient (Y Li *et al.* 2016). Regulations regarding the dip method currently include that the dosage forms need to be stable in formulation and in the dip solution, photostable, and that the dosage form would not separate from water in the dip tank (Fahmy *et al.* 2002; Hardee & Baggo, 1998).

N,N'-[(methylimino)dimethylidyne]di-2,4-xylidine, commonly known as amitraz, is mostly used as an acaricide for domesticated mammals, but is also the most commonly applied acaricide for honey bee parasites (Pohorecka *et al.* 2018). The compound inhibits ectoparasites from feeding (Jongejan & Uilenberg, 2004).

The purpose of this study is to produce a wide variety of matrices to carry the wettable form of Bayer's 98.5 % amitraz formulation. This study follows on some of the work done by Lushane Walburgh, where a urea based solid dosage form was designed containing at least 20 wt.% actives (Walbrugh, 2007). Bayer produces various cattle ectoparasite deterrents/pesticides. Liquid based pour-ons like Cylence® and Drastic Deadline®, powders such as Daz-Dust® and dip type products like Milbitraz® are sold by Bayer (Bayer Southern Africa, 2020). Powder and liquid form pesticides are often used ineffectively and have a direct impact on environmental pesticide pollution and contamination as well as the humans that apply them (Y Li *et al.* 2016; Kunz & Kemp, 1994).

The solid dosage form must contain at least 20 wt.% of the active ingredient. This specification is similar to the Milbitraz® plunge dip products currently on Bayer's market (Bayer Southern Africa, 2020). The specifications for a successful dosage form according to the requirements of Walbrugh (2007) are as follows: The composite must be photostable, stable when containing the active ingredient and stable when placed in room temperature water. The dispersion must also not form an oily phase (liquid-liquid phase separation). The resulting compound must have a melting point above 50 °C as to accommodate tropical and sub-tropical environments. The compound should deliver the pesticide in the designed dosage over a fixed time via a matrix that would fully dissolve in water. The matrix must also have no harmful effects to the environment and thus be fully biodegradable. The rate of dispersion is often classed as fast (± 5 min), intermediate (± 3 hours) or slow dissolution (*pm* 12 hours) (Walbrugh, 2007). In this work, two different solid dosage preparation methods, namely melt casting and melt extrusion are considered.

Eutectic salts containing urea as one constituent has been identified by Walbrugh (2007) due to its high solubility in water and low toxicity, as a suitable solid dosage form matrix. Urea decomposes prior to melting, thus the melting point reduction phenomenon of eutectic mixtures is exploited. The deep eutectic solvent can be melt cast, carrying the active ingredient in its solid form if the compound's melting point is well below that of amitraz. A combination of urea & 1,3-dimethylurea as well as urea & acetamide are considered to produce the solid matrix carrier formulation. This combination forms a eutectic mixture of acids and bases known as a deep eutectic/ionic solvent (Suriyanarayanan *et al.* 2019).

The casting method was used to produce the urea based formulations. The matrices were analysed at their eutectic composition to predict thermal stability and melting point. The dissolution rate of the selected formulation was quantified and interpreted. The selected formulation was cast with the active ingredient, and then analysed in a similar fashion, and then compared to the matrix properties. The residues of the dispersed particles was analysed using particle size analysis equipment.

A thermoplastic dextrin (TPD) was used as carrier material in the procedure where melt extrusion was investigated. Dextrin, a highly hydrolysed form of native corn or potato starch, is soluble in water at room temperature, and can be gelatinised to become extrudable at relatively low temperatures (Oliveira *et al.* 2017; S Wang, C Li, *et al.* 2015; Van Soest & Kortleve, 1999).

The stability of the resultant solid matrix may be compromised by the fact that TPD is known to retrograde (S Wang, C Li, *et al.* 2015; Yu & Christie, 2005). This phenomenon may cause a premature release of the active ingredient. In an attempt to combat retrogradation, the addition of certain nanofillers were considered. The effect of different combinations of nanoclays, nanocellulose and fatty acids were investigated.

The morphology, thermal stability and dissolution rate of various combinations of additives in TPD composites were documented. Based on the analysis methods mentioned, a suitable carrier matrix was identified. The chosen TPD formulation consisted of the base TPD composition (60 wt.% dextrin, 36 wt.% plasticiser) and 3 wt.% fatty acid combined with 1 wt.% nanocellulose. The residue particle size was also analysed to interpret what effect the active ingredient and other additive may have on the production and dissolution of the compounds.

2 Literature

2.1 Pesticides and their application in livestock

The Oxford English Dictionary defines a pest as a destructive insect or animal which attacks crops, food or livestock. Pesticides are often grouped by application or chemical structure. By application; pesticides are grouped as insecticides, herbicides, fungicides, miticides and acaricides (often considered a subgroup of insecticide even though they aren't insects), rodenticides, molluscicides, avicides, algaecides, plant growth regulators, and soil sterilants (Greene, 2013: XV)(Codex Alimentarius, 2020). Structural groups are classed as organochlorides, triazines, nitropesticides, carbamates, organophosphates, sulphonylureas and other lumbped classes (Codex Alimentarius, 2020; Garrido *et al.* 2004).

2.1.1 The main livestock parasite genus, *Ixodes*

For large livestock the most common pest threat is ticks (Greene, 2013: XVI). Ticks bring about infectious diseases by acting as carriers of that disease. Thus ticks are vectors for the infections listed in the Introduction section. These *acari* (a taxon of arachnids including ticks and mites (Fisher & Dowling, 2010)) latch on to the exterior of terrestrial and in some habitats, aquatic animals where they feed on dead organic matter on the skin or on blood (US Department of Health & Human Services, 2019a).

Ticks spread disease by transmitting pathogens that lead to disease while feeding. Figure 1 is an illustration showing stages of tick feeding. After finding a feeding spot (which takes 10 minutes to 2 hours), the tick will grasp onto the skin surface and pierce the skin of the animal with its feeding tube (**a)**). The second step **b)** shows the tick excreting saliva. This allows the parasite to feed on the blood and also is the medium for transmitting disease. In step **c)** the tick is feeding on the animal. During this 5-12 day period the arachnid will share bacteria with the animal transferring more of the disease it carries. In **d)** we see the tick growing. It will eventually detach to mate, lay eggs or latch on to another animal, where it may transfer a newly acquired disease (US Department of Health & Human Services, 2019a; No bite is right, 2017).

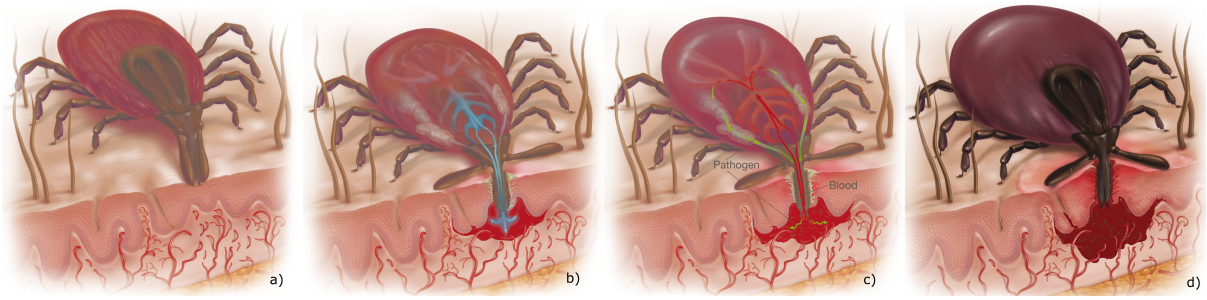

Figure 1: Tick feeding graphic (No bite is right, 2017).

2.1.2 Livestock treatment against tick-borne diseases

As stated in the Introduction, treatment against ticks come in the form of acaricides. These chemicals are applied as dip or spray, injection or backline pour as per product specification. The timing of the application of the acaricide is also key. If the treatment occurs early in season, it can reduce tick population explosions in spring time (US Department of Health & Human Services, 2019a; Greene, 2013). For the purpose of this study the plunge dip method will be investigated.

The plunge dip method is usually configured like a bath or narrow channel through which animals walk. The channel will be filled with the required dosage mixture of acaricide and water. When cattle enter the dip one after the other, they will be immersed (just below the jawline) in the liquid mixture. Plunge dipping has remained the most economic and easy way to treat large amounts of animals against external parasites (Junquera, 2015; Walbrugh, 2007). Figure 2 shows a schematic of a plunge dip whereby cattle run from right to left through a body of liquid (Grandin, 2010).

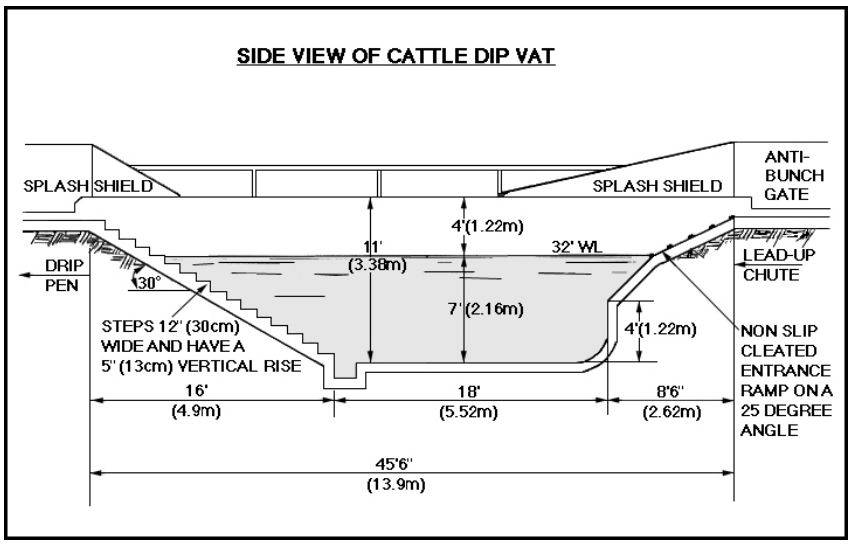

Figure 2: Plunge dip vat schematic (Grandin, 2010).

Grandin (2010) states that this application method has some disadvantages. It is often less effective against flying parasites. Plunge dips require the construction of either a permanent, usually concrete structure or a portable vat. Plunge dipping is also considered to be stressing for animals and can also be somewhat violent to livestock. If disposed incorrectly a the dip liquid may damage the environment, especially aquatic life (US Department of Health & Human Services, 2019a). The greatest risk however is a resistance to acaricides.

2.1.3 Acaricides

Acaricides are often referred to as ixodicides (specific to ticks) or miticides (specific to mites) (Mullen & Durden, 2009). Examples include permithrin, carbamates, ivermectin and organophosphates. amitraz, part of the (form)amidine family, is used as a pesticide for plants, animals and also for bees to fight against their parasites (Pohorecka *et al.* 2018; Jongejan & Uilenberg, 2004). It is known to be insoluble in water and to have synergistic compounds that aid in its application (Jongejan & Uilenberg, 2004).

Its use against crop pests is to control the population of whiteflies, aphids and plant mites and ticks (Corta *et al.* 1999). In animal applications, the pesticide inhibits ectoparasites from feeding and also encourage the detachment of prior ectoparasites (Jongejan & Uilenberg, 2004). It is speculated to do this by damaging the feeding tube of the parasite in stage **b)** and **c)** of Figure 1.

2.2 Solid dosage forms

Dosage forms are defined as a mixture of active ingredients and inactive components and excipients (Hess, 1985: 11). An excipient is the inactive fraction of a dosage form. Its simple purpose is to safely contain an active ingredient, and to maintain the release of the active to a certain rate. The classification of the dosage form is linked to its configuration and delivery (oral, topical, suppository etc.) and dose. A solid dosage form is a drug delivery system including pills, capsules, sachets, powders, granules and tablets (Banker & Rhodes, 1990: 355). Hess (1985: 11) explain that the combination of excipient and active must be:

1. Stable (chemical, physical, microbiological and to a lesser extent morphological stability) for long term storage.
2. Practical and simple to administer administration.
3. Chemically inactive to the extent that it does not display undesirable interaction with active ingredient.
4. Inert or have no harmful effects on the item of application.
5. Cost effective and rational to manufacture and package.
6. Able to deliver an accurate dosage of the active ingredient.

Active ingredients that are solid at room temperature are produced in an excipient as either a liquid dispersion or solid dispersion. Liquid dispersions are simply the solid active dispersed in a solvent to form a liquid solid mixture. These mixtures often need to be shaken/mixed/re-processed before administration in order to deliver the designed dosage of the active ingredient. A solid dispersion is the dispersion of one or more active ingredients in an inert carrier matrix at solid state (Chiou & Riegelman, 1971). A solid dosage form is either administered as is or dispersed into a solvent, where the active would be released into the liquid solvent (Mayersohn & Gibaldi, 1966). In both cases, solubility of the dosage form may be required. The direct application is geared toward individual application or applications on small populations. For larger populations, the dispersion of a solid form into a large solvent volume is more realistic. Solid dispersions in water-soluble carriers were shown to improve the dissolution rate and bioavailability of a range of hydrophobic drugs compared to conventional dosage forms (Chiou & Riegelman, 1971). The methods of preparation of these dispersions are highlighted:

1. Melting method; where a drug and carrier mixture is heated until molten, and then solidified. This method is often used to prepare fast release dosage forms (Sekiguchi & Obi, 1961).

2. Solvent method; whereby a mixture of two constituents is dissolved in a solvent, followed by evaporation of the solvent (Mayersohn & Gibaldi, 1966).

3. Melting-Solvent method; which involves incorporating a drug which is dissolved in a liquid solvent into a molten carrier without removing the solvent (Chiou & Riegelman, 1971).

2.2.1 Soluble excipients

In certain applications, the excipient must be fully soluble in water as in the case of pharmacological capsules containing an orally ingested medicine. Various polysaccharides have been used as binders, including starch and microcrystalline cellulose (MCC) (Mateescu, Ispas-Szabo & Assaad, 2015). For the plunge dip application, as discussed in the Livestock treatment against tick-borne diseases explanation, a liquid dispersion or solid dispersion can be used. However, solid dispersions are often preferred as this method allows for a more regulated active ingredient dosage throughout lengthy applications (Banker & Rhodes, 1990: 363). When a liquid dispersion is used, the active would already be completely released from the beginning of the application.

Thermoplastic starch (TPS) without additives in low molecular weights (sometimes referred to as thermoplastic dextrin (TPD)) are completely soluble in water. This in effect will mean that the starch will be completely digestible for human consumption. CNF's are not digestible, but are completely safe for human consumption at relatively low doses, as well as most nanoclays and fatty acids.

In the agricultural industry, the management of ectoparasites requires a fully soluble excipient to carry the active pesticide/acaricide. The possibility of TPD as a matrix carrying an active ingredient may lead to several future possibilities. The dissolution rate of TPD in water may also be manipulated with the addition of nano-fillers.

2.3 Starch background

For the past couple of decades, a strong replacement for petroleum-based plastics has become increasingly important. These substitutes need to fulfil several niche's and thus need to have similar physical properties to that of the oil-based counterparts that fulfil that application. There are three main reasons that petroleum-based polymers need to be replaced:

1. All petroleum-based polymers produced in current mainstream industry originate from non-renewable sources (Geyer, Jambeck & Law, 2017).
2. These plastics are very durable, even in saline environments, and may have a lifetime estimated to be hundreds to thousands of years (J Wang *et al.* 2016; Tokiwa *et al.* 2009).
3. Oil-based polymers form micro-plastics, fragments of plastics smaller than 5 mm in size that bio-accumulate and have effects not yet fully understood (Andrady, 2011).

Fully biodegradable plastics are plastics that entirely decompose via naturally occurring micro-organisms and leave no residues during and after decomposition. The decomposition of fully biodegradable plastics only form carbon dioxide and water. Along with extensive research into bio-fuels, starch and cellulose have been identified as suitable base materials for the preparation and production of bio-plastics (J Wang *et al.* 2016). Starch is a cheap and abundant bio-polymer used in packaging which unfortunately is hydrophilic and contains undesirable mechanical properties (Kvien *et al.* 2007). It is thus often reinforced by cellulose nano-crystals (CNC's) and/or cellulose nano-fibres (CNF's) which vastly improve its mechanical properties (Ferreira *et al.* 2018; Dufresne, Dupeyre & Vignon, 2000).

The abundance in nature and strong bio-degradability has made the starch and cellulose substitutes very attractive (Nafchi *et al.* 2013). Thermoplastic starch (TPS) is produced by the gelatinisation of starch. These thermoplastic starches have a strong tendency to undergo retrogradation, whereby the starch recrystallises as it ages (Kvien *et al.* 2007). The effect of various additives have negated some of the negative effects of retrogradation or halt the phenomenon entirely.

The properties of starch has also attracted research into a wide variety of possible uses for the compound. The fact that starch also displays very different properties at various degrees of polymerisation gives it a wider flexibility for each use. Some forms of starch

are completely soluble in water, while others may be used as packaging (Kvien *et al.* 2007).

Starch is a polysaccharide (composed of many glucose monomers) and thus consists of essentially carbon, hydrogen and oxygen. Figure 3 shows how amylose (a structure component of starch) and glycogen are composed of α-glucose and how cellulose is a polymer of β-glucose. Polysaccharides are known to degrade at relatively low temperatures ($<$ 100 °C) whereby a brown to black soot is formed (S Wang, C Li, *et al.* 2015).

Starch can be isolated from parts of plants containing large concentrations of the starch's molecular entities. These parts include fruits, roots, seeds, leaves and pollen (Zobel, 1988). Corn, wheat and potato are substrates most commonly used to extract starch. Each substrate has varying combinations of amylose and amylopectin, the components that make up starch (Yu & Christie, 2005).

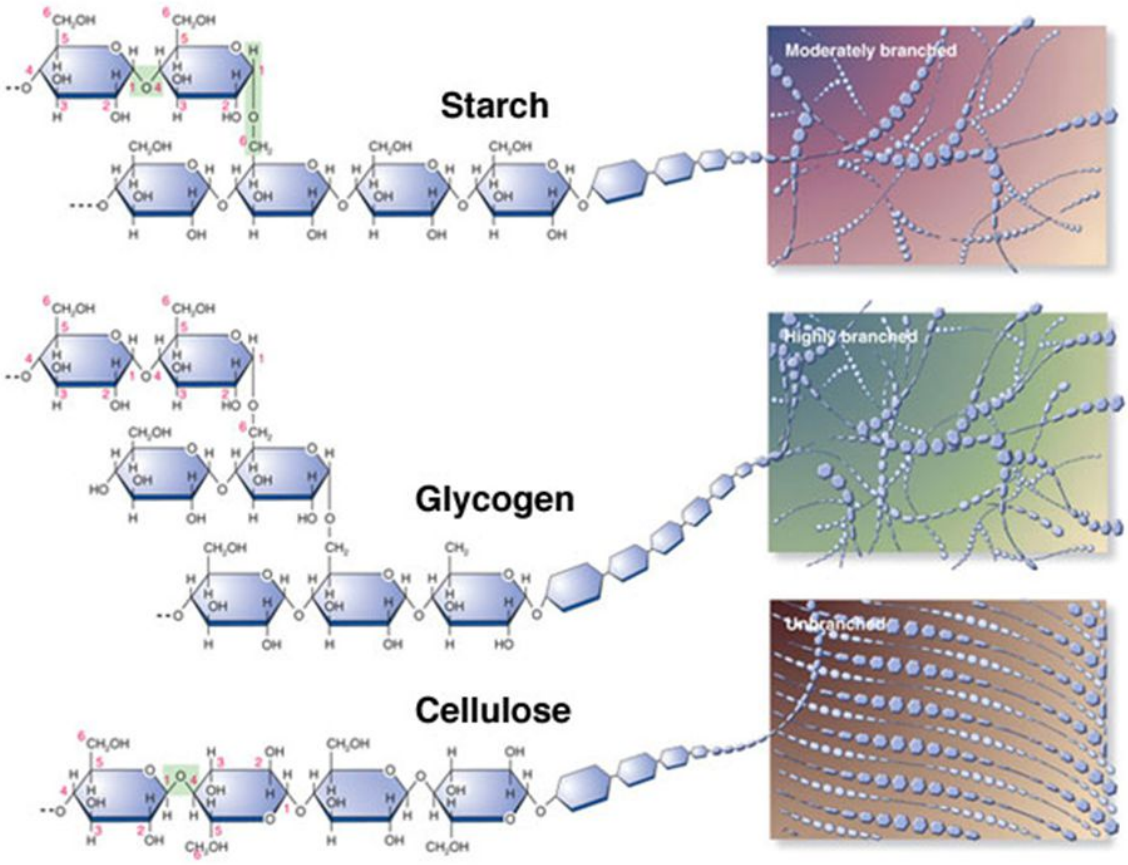

Figure 3: Schematic representation of amylose, glycogen and cellulose and how different there monomers are (Raniya, 2014)

.

2.3.1 Amylose and amylopectin

Starch, starch granules and starch polymers are heterogeneous. It contains amylose and amylopectin, two chemically distinct starch components. Physically it contains amorphous and crystalline regions. Amylose is a linear structure combination of α-1,4 linked glucose units, while amylopectin is a highly branched combination of the short α-1,4 backbone linked by α-1,6 glucose bonds (Yu & Christie, 2005).

Figure 4 shows schematically how amylose is connected by the units labelled 1 and 4, while the branched connection occurs at units labelled 1 and 6 (Pérez & Bertoft, 2010). Torsion angles are also shown and play a large role in the structure of amylose, and how it sometimes may form a single helical structure.

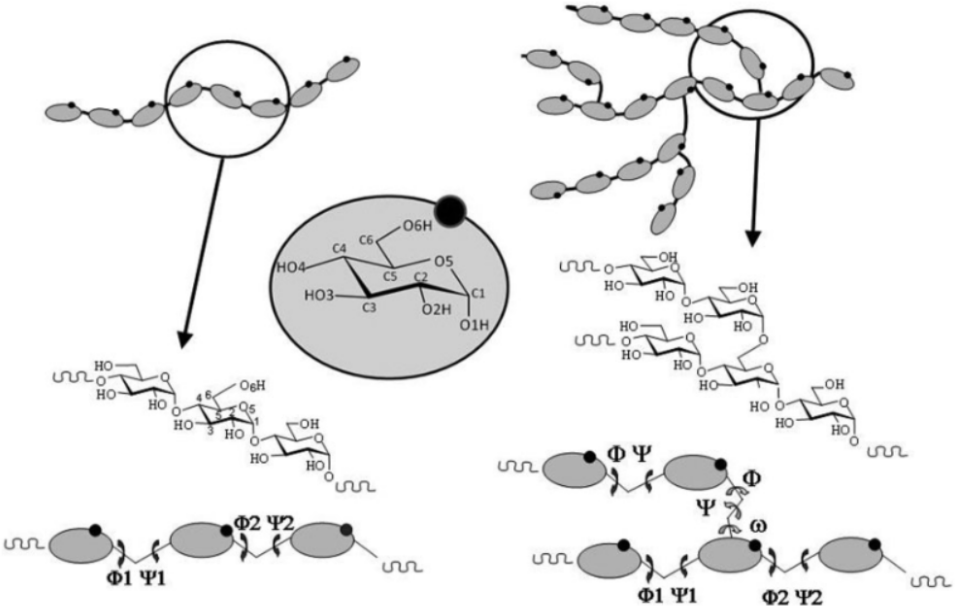

Figure 4: Schematic representation of amylose and amylopectin labelling atoms and torsion angles (Pérez & Bertoft, 2010).

Figure 5 depicts a representation of a cluster of amylopectin's branches. It is immediately noticeable that these branches display a double helical formation. These double helical branches usually pack closely alongside one another to create distinct crystalline regions.

Tanetrungroj & Prachayawarakorn (2015) found that thermoplastic starches made of high amylose native starches showed higher strength, hardness and degree of crystallisation. Cano *et al.* (2014) also discovered that rice starches with low amylose amounts were more elastic and less stiff than the high amylose rice films produced by Tanetrungroj & Prachayawarakorn (2015).

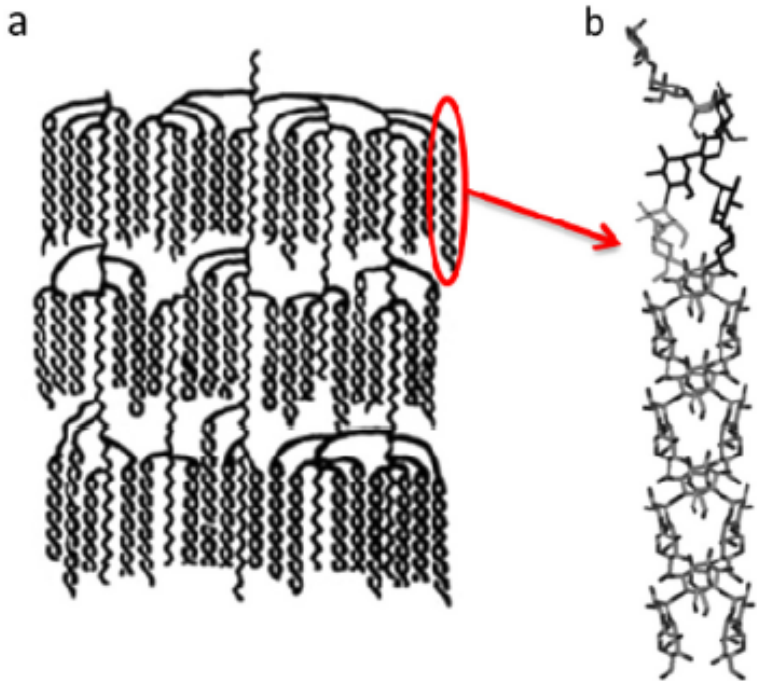

Figure 5: (a) Schematic representation of amylopectin; (b) Double helix crystalline amylose. Adapted from (Pérez & Bertoft, 2010).

2.3.2 Starch types

Starch can be hydrolysed to many types; including dextrin, maltodextrin, cyclodextrin, amylodextrin and highly branched cyclic dextrin. Dextrin is a group of low molecular weight polymer of less than twenty glucose units. It is widely produced in a powder form to be used in the adhesive industry. Dextrin is also greatly used in the papermaking industry where it is often used as a flocculant, retention aid and adhesive (Maurer, 2009).

After the process of hydrolysis, the resulting dextrins will have less glycosidic bonds. The glycosidic bonds connect the units as shown in Figure 4. The extent of conversion of the starch to dextrin is quantified by a term called the dextrose equivalent (DE). Lightly hydrolysed maltodextrin (DE 10 - 20) is easily digestible and is mostly used as a food additive. Figure 6 depicts a maltodextrin molecule where n (the monomer count) ranges between 2 and 20 for maltodextrin molecules.

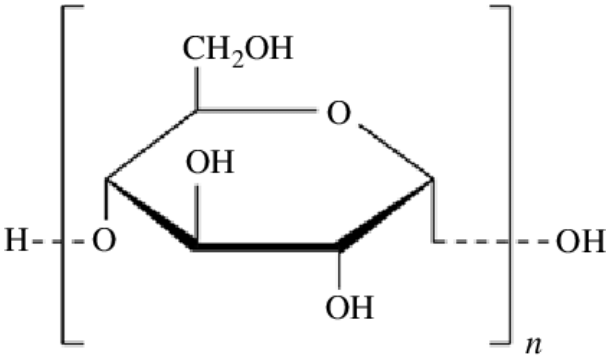

Figure 6: A single D-glucose unit representing a maltodextrin molecule, where 2 < n < 20 (Villermaux, Pistre & Lhuissier, 2013).

Maltodextrin is the form of starch most easily gelatinised and melt processed to form TPS (Nafchi *et al.* 2013; H Liu, Xie, *et al.* 2009). Higher DE starches include glucose syrups, dextrose and sugar alcohols.

2.3.3 Starch morphology

Starch is a semi-crystalline polymer. X-ray diffraction (XRD) data often displays noisy and broad diffraction peaks and a large amorphous baseline (Frost *et al.* 2009). Native starch crystal structures occur as two distinct polymorphs; A-type and B-type, depending on the origin of the starch. These structures are also present in thermoplastic starch (TPS). TPS is produced mostly by melt compounding in extruders. The processing technologies and properties of TPS are discussed later in the Thermoplastic starch processing and Retrogradation of thermoplastic starches subsections. This section of the literature survey is applicable to both native starch and processed starch.

Cheetham & Tao (1998) also introduces the C-type polymorph and classifies A-type as cereal starches, B-type as tuber starches and states that C-type is defined as a mixture of A-type and B-type starches. After melt processing and gelatinisation, retrogradation may occur, forming V-type amylose crystals (Chauhan, Sharma & Bains, 2003; Q Liu & Thompson, 1998). V-type starch results when amylose starch molecules are compounded with fatty acids (e.g. stearic acid (SA)), emulsifiers and iodine, and are also referred to as amylose-lipid complexes (ALC's) (Cheetham & Tao, 1998). V-type starch is sometimes referred to as processed crystalline starch and is often split into V_H-type starch (hydrated), V_A-type starch (anhydrous) and E_H-type starch (processed) (Lendvai, Sajó & Karger-Kocsis, 2019; Van Soest, Hulleman, *et al.* 1996). The V-structure occurs where amylose single helices co-crystallise with inclusion substances (water, fatty acids, alcohol etc.). The V_A form of this crystal contains less water and has more shrunken helices compared to the V_H form (Van Soest, Hulleman, *et al.* 1996).

Table 1: Starch polymorphs and their XRD crystalline peaks.

Starch polymorph	2θ (°)	Reference
A-type	15.2, 17.2/18.1, 22.9	(Area *et al.* 2019)
	15, 17/18, 22.5	(Lendvai, Sajó & Karger-Kocsis, 2019)
	15, 17/18*	(Cheetham & Tao, 1998)
B-type	5, 15, 16, 20, 22, 24	(Cheetham & Tao, 1998)
	5.5, 15, 17, 22, 24	(Zobel, 1988)
	5.7, 15.1, 17.7, 19.8, 22.3, 23.9, 26.3	(Zobel, 1988)
C-type	5, 15, 17, 19, 22	(Cheetham & Tao, 1998)
	5.6, 15, 17, 18, 23.5	(Xia, Li & Gao, 2016)
V_A-type	7.6, 13, 20	(Van Hung, Vien & Phi, 2016; Yoo & Jane, 2002)
	7, 13, 20	(Oliveira *et al.* 2017; Frost *et al.* 2009; Zobel, 1988)
	7.8, 13.6, 20.8	(Lendvai, Sajó & Karger-Kocsis, 2019; Van Soest, Hulleman, *et al.* 1996)
V_H-type	7.5, 12.7, 18.3, 19.5, 22.1	(Lendvai, Sajó & Karger-Kocsis, 2019)
	7.1, 12.6, 19.4, 22.1	(Van Soest, Hulleman, *et al.* 1996)
E_H-type	6.9, 12, 18.4, 24.9	(Nafchi *et al.* 2013; Van Soest, Hulleman, *et al.* 1996)

* / is used when describing a doublet at those peaks.

Lendvai, Sajó, *et al.* (2019) state that during ageing, under controlled conditions, two morphological changes occur. They state that V_A-type ages to V_H-type followed by V_H-type to A-type amylose crystals. This last transition is indicative of the retrogradation phenomenon.

The morphology of the TPS can also be measured via differential scanning calorimetry (DSC). DSC is a thermal analsis technique in which the heat needed to rase the temperature of a sample is measured. It is useful for applications in starch as it can be used to infer morphology by measuring at what temperature and to what extent crystal structures within the sample undergoes phase change (H Liu, Xie, *et al.* 2009; Yu & Christie, 2001). Yu & Christie (2001) state that the complexity of TPS make DSC analysis difficult, implying that sample preparation, pan type and measurement conditions cause large varieties in results. TPS undergoes several phase transitions and displays instability of water contained in TPS. DSC has however become the most suitable measure of gelatinisation of TPS (H Liu, Xie, *et al.* 2009). Figure 7 from (H Liu, Yu, *et al.* 2006) displays several endotherms of TPS that have varying moisture content.

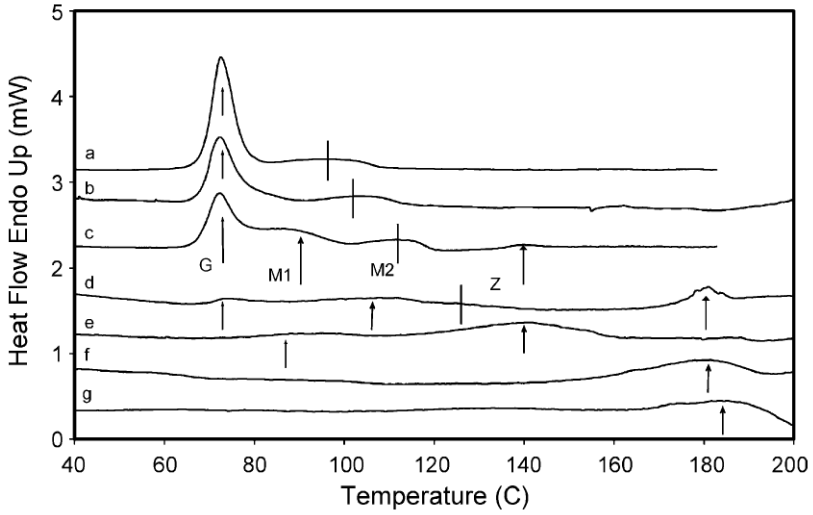

Figure 7: DSC endotherms of TPS with varying water content (H Liu, Yu, *et al.* 2006).

Peak G on Figure 7 is usually shown with starches containing excess water and represents the gelatinisation of amylopectin (Yoo & Jane, 2002; Russell, 1987; Wootton & Bamunuarachchi, 1979). M1 represents the melting of crystallites (Russell, 1987). M2 is considered to represent a phase transition within amylose lipid complexes (ALC) (Jovanovich & Añón, 1999). An ALC is a starch based composite structure consisting of a lipid/fatty acid and a helical amylose chain shown in Figure 13 (López, Vries & Marrink, 2012). Z has been attributed to the fortification of amylopectin crystals during heating (Russell, 1987; Maurice *et al.* 1985).

2.4 Gelatinisation of starch

Starch undergoes numerous phase transitions and physical and chemical reactions during processing which are more complex than conventional plastics. These include gelatinisation, decomposition, melting, crystallisation and water diffusion (H Liu, Xie, *et al.* 2009). Prior to gelatinisation, starch's decomposition temperature is lower than its melting temperature, which is why starch needs to be gelatinised before it can form TPS.

S Wang, C Li, *et al.* (2015) describe gelatinisation of starch as the disruption of crystalline regions in starch by the addition of a polar plasticizer. This makes it possible to let the starch undergo melt processing. During extrusion of gelatinised starch the A-type native crystal structures rearrange to form ALC's (Oliveira *et al.* 2017). The onset of gelatinisation with glycerol and water mixtures occurs at 58 °C, and continues until 80 °C according to DSC (Chen *et al.* 2019; Oliveira *et al.* 2017; H Liu, Xie, *et al.* 2009; Yoo & Jane, 2002). These values however are strongly dependent on the degree of hydrolysation of the starch. Figure 8 is a schematic representation of the impact of gelatinisation on the amylose and amylopectin molecules.

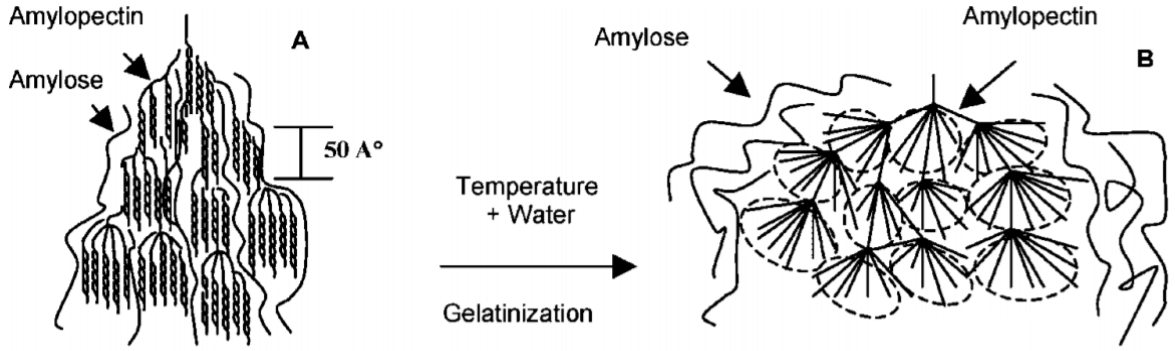

Figure 8: Representation of gelatinisation phase transition. Adapted from (Yu & Christie, 2005).

As shown in Figure 8, gelatinisation destroys the crystalline structure between phase A and phase B. The double helix structures of the amylopectin molecules have clearly expanded to form what Yu & Christie (2005) describe as "gel balls".

2.5 Thermoplastic starch processing

2.5.1 Effect of plasticisers

The preparation of TPS always involves plasticisers. In order to melt process starch, it needs to be gelatinised, which is the role of many of the plasticisers used in TPS production. García *et al.* (2011) investigated the effect of glycerol on the morphology of TPS. The addition of glycerol as plasticiser results in a lower apparent viscosity (Rodriguez-Gonzalez, Ramsay & Favis, 2004; Rodriguez-Gonzalez, Ramsay & Favis, 2003). The effect of glycerol however is not always as expected. H Liu, Xie, *et al.* (2009) have found conflicting results indicating more complex melt viscosity behaviour. Several other parameters during extrusion, may also display the inconsistent effects (H Liu, Xie, *et al.* 2009).

Water has been used to cook starch containing compounds for centuries. This is due to the fact that high starch containing compounds will thermally degrade before cooking without water. During gelatinisation with water, starch granules begin to swell as shown in Figure 8. Theoretically this effect would increase the melt viscosity of the compound, however Ilo *et al.* (1996) showed that shear forces in extrusion breaks the swollen granules, thus reducing the apparent viscosity.

Citric acid as plasticiser may increase the range of processing temperatures. It also reduces melt viscosity due to the acidic compound weakening entanglement and increasing fragmentation (Ning *et al.* 2007; R Shi *et al.* 2007; Jiugao, Ning & Xiaofei, 2005). Several other plasticisers have been used to gelatinise starch. These include vegetable oils and various metallic stearate combinations (Keszei *et al.* 2006; Onteniente, Abbès & Safa, 2000).

2.5.2 Premix preparation

Prior to thermal processing, some work needs to be done with the starch-plasticiser-additive mixture. Hietala, Mathew & Oksman (2013) investigated how to utilise nanocellulose as additive in thermoplastic starch. This investigation concentrated on mixture preparation and extrusion conditions. The preparation of cellulose nanofibres involved methods described by Abe, Iwamoto & Yano (2007), Iwamoto, Abe & Yano (2008) and Gong, Mathew & Oksman (2011). Dispersion of additives that do not dissolve in a polar solvent (water and glycerol w.r.t. this study) were achieved via high rate shear mixing. The final batch containing the plasticiser and starch can then be manually blended prior to extrusion.

2.5.3 Melt processing

As stated in the Gelatinisation of starch subsection, starch needs to be highly plasticised before undergoing melt processing, because the native starch's melting temperature is above its decomposition temperature. Thus depending on plasticiser type and content, the envelope for processing temperatures is not very large. This study is focused on specifically extrusion compounding of TPS. Hietala *et al.* (2013) suggest a 80/90/90/100/100/110/110 °C temperature profile for a twin screw co-rotating extruder. Single screw extruders have also been used, but the twin screw configuration is often preferred ue to higher mixing capabilities. Dextrins and maltodextrins may require low temperatures, thus a preliminary profile is shown in Figure 9. The temperatures shown in Figure 9 are different from the ones used by Hietala *et al.* (2013), as these are the processing conditions used in this study.

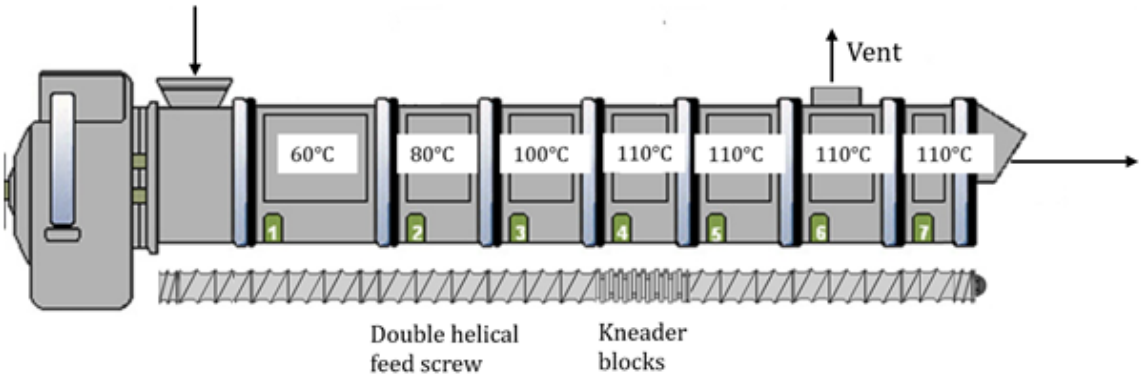

Figure 9: Extruder and screw profile. Adapted from (Hietala, Mathew & Oksman, 2013).

Most melt processing applications for TPS operate at 200 RPM. It will be crucial to have a mixing section with kneader blocks in the extruder to disperse the solid additives inside the melt.

2.5.4 Ageing

After extrusion, the conditions at which the extrudate is kept has to be controlled as many morphological changes occur during ageing (S Wang, C Li, *et al.* 2015). A simple method to do this, is to create an atmosphere with a fixed humidity at a controlled temperature. This can be achieved through a small space in the presence of a saturated or supersaturated salt solution in an environment where the temperature is maintained (Greenspan, 1977).

2.6 Retrogradation of thermoplastic starches

2.6.1 Retrogradation effects

S Wang, C Li, *et al.* (2015) define starch retrogradation as the process in which disassembled amylose and amylopectin chains in a gelatinised starch composite, reassociate to form more ordered and crystalline structures. The recrystallisation of amylose is far quicker than that of amylopectin and occurs immediately after melt processing. Studies on retrogradation focus on the slower reordering of amylopectin chains and its effect on the structure of thermoplastic starch. This mechanism leads to an embrittlement and shrinkage of the compound (Lendvai, Sajó, *et al.* 2019; Jiménez *et al.* 2013; Van Soest & Kortleve, 1999).

The easiest way to investigate retrogradation is through XRD analysis. This allows for the estimation of the crystallinity of the thermoplastic compound and what crystal structures exist. As described in the Starch morphology subsection, after melt processing, V_H, V_A and E_H crystal structures are formed in the thermoplastic matrix. Nafchi *et al.* (2013) state that all retrogradation processes are due to the absorption of water, allowing the movement of polymer chains in the hydrogen bonded matrix. Figure 10 schematically represents the phase transitions starch undergoes prior, during and after melt processing.

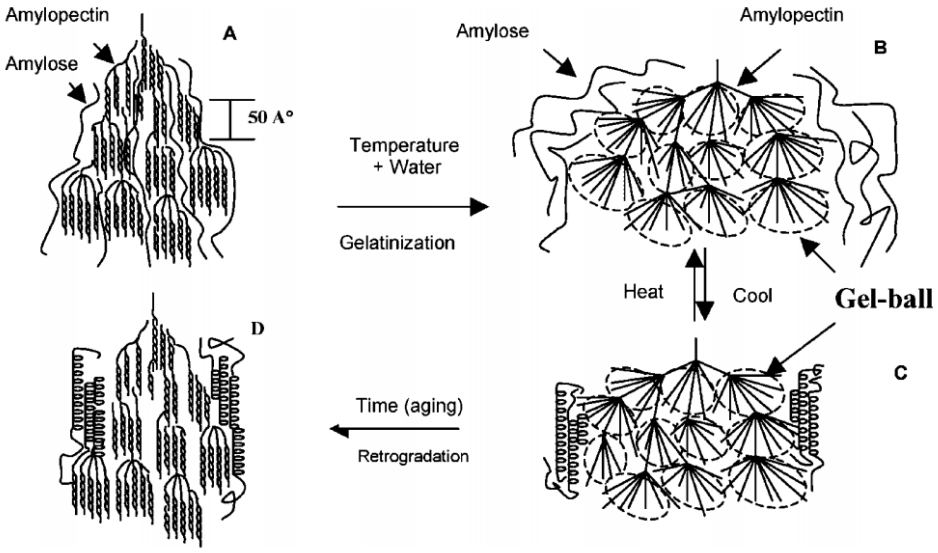

Figure 10: Amylose and amylopectin phase transition during gelatinisation and retrogradation Yu & Christie, 2005.

The fast recrystallisation of amylose into single helices are shown between B and C, while the slow gradual retrogradation process is represented between C and D. It is also noticeable that the representation shows the amylose helices are closely packed and form crystal structures (V_A- and V_H-types) due to this tight packing.

Crystallinity, and changes in the overall crystallinity of a sample may not always accurately depict retrogradation. There are several crystal type transitions that TPS can undergo without a noticeable increase in the ratio of the crystalline fraction in the TPS to the sum of the amorphous fraction and crystalline fraction (Frost *et al.* 2009). Ageing experiments show a definite increase in water content of the polymer matrix, accelerating the rate of retrogradation. Lendvai, Sajó, *et al.* (2019) and Buléon *et al.* (1990) concluded that during the initial ageing period, all V_A-type crystals hydrated to V_H-type crystals. In later periods of ageing V_H-type crystals may also transform to A-type crystals as seen in Figure 11, implying that some single helix amylose structure becomes linear in nature.

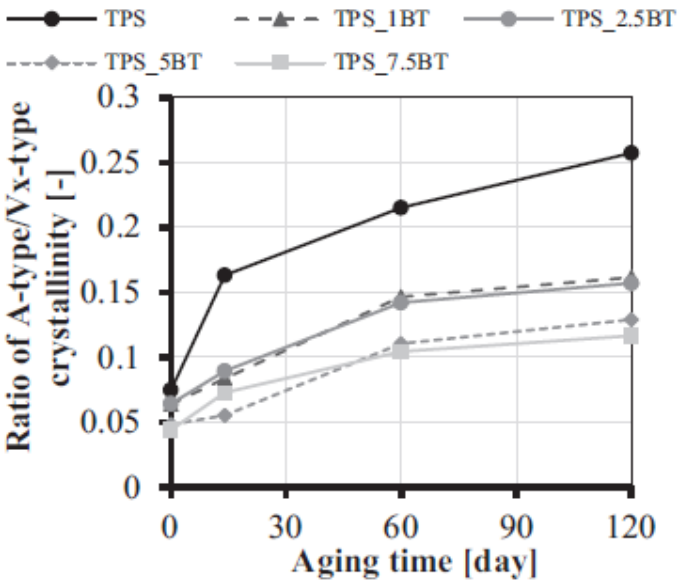

Figure 11: Ratio of A-type crystals to V-type crystal structures for TPS and TPS-bentonite nanocomposites as the composites age (Lendvai, Sajó & Karger-Kocsis, 2019).

The two main crystallinity phase changes match well with the change in mechanical properties during ageing. Lendvai, Sajó, *et al.* (2019) investigated the change in mechanical properties while observing the morphological effect of retrogradation. They found that the tensile strength and Young's modulus increased sharply in the first phase of ageing, while a steady, but far slower, increase continued after. Elongation at break had the opposite response.

2.6.2 Retrogradation prevention

In order to completely prevent retrogradation and/or its effects, the resulting compound must not change in crystallinity and must not change in terms of types of crystal structures, and must thus quickly stabilise its mechanical properties after melt processing. Various studies have investigated retrogradation and mechanisms that may retard the rate of retrogradation or prevent it completely. The prevention of retrogradation has been split into two main themes. The use different plasticisers (Area *et al.* 2019; Battegazzore *et al.* 2015; Khanna & Tester, 2006) and compounding together with additives (Hietala *et al.* 2013; Samutsri & Suphantharika, 2012; Biliaderis, Arvanitoyannis, *et al.* 1997).

In the food industry retrogradation may actually positively affect the quality of melt processed products. However, a negative affect in terms of nutritional properties and shelf-life is generally observed (Fu *et al.* 2015). In this industry, the preventative measure to retrogradation must also be safe for human consumption. Lipids (Biliaderis & Tonogai, 1991), salts (Samutsri & Suphantharika, 2012; Ahmad & Williams, 1999), proteins (Jiménez *et al.* 2012; Ottenhof & Farhat, 2004), acids (R Shi *et al.* 2007) and other organic compounds have shown a notable effect on the reduction of the rate and effect of retrogradation.

Organic compounds as plasticisers (other than glycerol) have shown mixed results. Some studies report a retardation of retrogradation using konjac glucomannan and guar gums (Khanna & Tester, 2006; Funami *et al.* 2005). Other studies using similar compounds like yellow mustard mucilage and xantham gum report no effect (H Liu, Eskin & Cui, 2003; Ferrero, Martino & Zaritzky, 1993). Other very similar hydrocolloids display an increased rate of retrogradation (Biliaderis, Arvanitoyannis, *et al.* 1997). A recent breakthrough has shown that replacing commonly used TPS plasticisers with isosorbide completely inhibits the retrogradation phenomenon. The bicyclic sugary isosorbide is a compound obtained from glucose dehydration (Area *et al.* 2019; Battegazzore *et al.* 2015). Compounding with isosorbide requires lower temperatures. However it greater amounts of work during batch preparation as it is very hygroscopic (J Shi *et al.* 2016; Battegazzore *et al.* 2015) and has shown no signals indicating retrogradation (Area *et al.* 2019).

Several investigations on CNF (cellulose nanofibres) and CNC (cellulose nanocrystals) as additives in TPS formulations have been done. The main aim of these studies were to determine the effect of the additives on the retrogradation behaviour of the TPS matrix, specifically in terms of its mechanical properties. CNF's have high surface area and aspect ratio, which enhance properties of polymers, similar to that of glass fibre additives in polymers.

Figure 12 displays how the strength of the TPS compound increases with an increase in CNF content. Hietala *et al.* (2013) state that the addition of 10 wt.% CNF increased the Young's modulus from 450 MPa to 900 MPa and decreased the elongation at break from 23 % to 8 %.

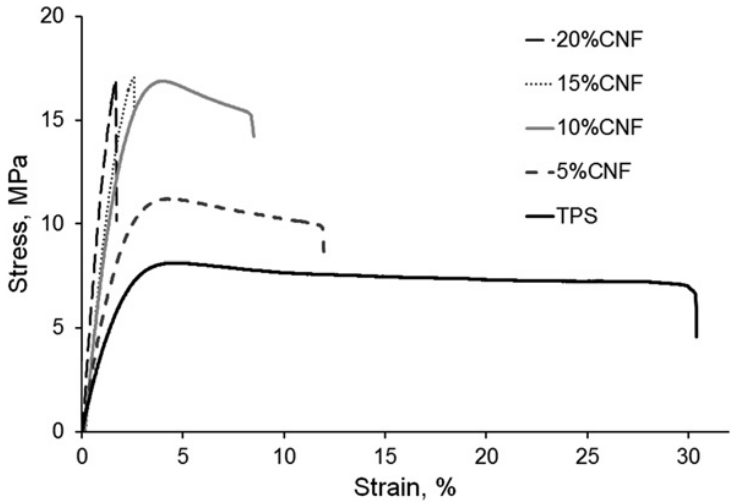

Figure 12: Stress-strain curves for TPS and TPS-CNF nanocomposites (Hietala, Mathew & Oksman, 2013).

The addition of cellulose to the matrix of TPS, may lead to a competition over moisture between the carbohydrates (S Wang, C Li, *et al.* 2015). This competition may slow the rate of retrogradation of the compound depending on the concentration and properties of CNF used as the migration of water to CNF will stop the conversion of anhydrous V-type crystals to hydrated V-type crystals.

Layered double hydroxide (LDH) is a generic term for a class of ionic solids with a layered structure of metal cations and hydroxide anions (Q Wang & O'Hare, 2012). These compounds occur in nature as inorganic minerals and can be processed to the nanoscale, where it is commonly known as nanoclays. LDH's are hydrophilic and houses hydrated layers in equilibrium with the rest of the compound (Hibino & Kobayashi, 2005).

Nanoclays have been used as additives to manipulate the mechanical, morphological and thermal properties of TPS. Hydrocalumite, bentonite, montmorillonite and many other nanoclays have shown a clear increase in tensile strength and Young's modulus at the cost of elongation at break of the thermoplastic starch (Lendvai, Sajó, *et al.* 2019; Vaezi, Asadpour & Sharifi, 2019; Lendvai, Kmetty & Karger-Kocsis, 2017; Ojijo & Ray, 2013).

Linear chain surfactants, emulsifiers and fatty acids (e.g. stearic, oleic, myristic and palmitic acid) have shown to strongly influence the functional and structural characteristics of starch and TPS (Jiménez *et al.* 2013; Jiménez *et al.* 2012; Raphaelides, Dimitreli,

et al. 2011; Mercier *et al.* 1980; Raphaelides, Arsenoudi, *et al.* 2010; Bhatnagar & Hanna, 1997). These fatty acids characteristically consist of a polar carboxyl end and a non-polar linear chain.

When compounded together with amylose and water, these fatty acids can form inclusion complexes during melt processing, generally referred to as amylose-lipid complexes. These inclusion complexes occur when the fatty acid's non-polar aliphatic chain are centred inside the single helix amylose structure as shown in Figure 13.

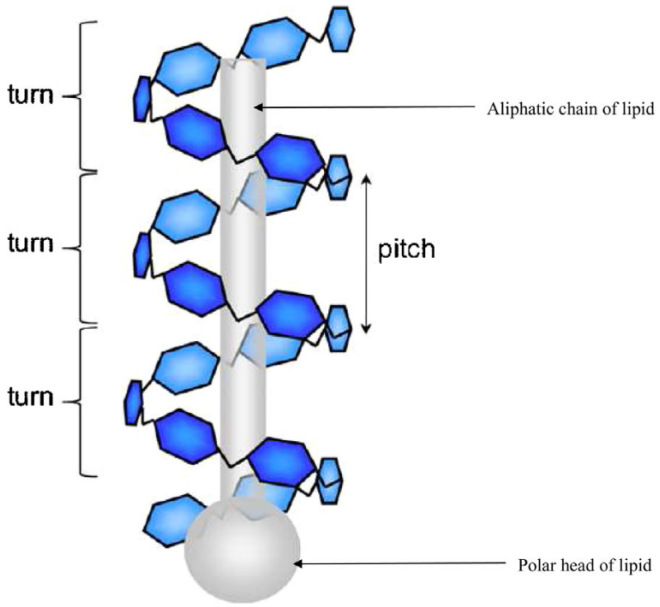

Figure 13: ALC structure. Adapted from (López, Vries & Marrink, 2012).

ALC's are generally classified as type I or type II complexes. The main difference is crystalline melting temperatures. Type I melts between 94 °C 104 °C, while type II transitions in the range of 115 °C to 121 °C (Biliaderis & Seneviratne, 1990). Panyoo & Emmambux (2017) deduce in their review of ALC's, that there is no official method to determine ALC levels in food and TPS. XRD can qualitatively show the presence of ALC's, while DSC is useful to classify between type I and type II and their sub-types.

Studies have shown that amylose co-crystallisation with amylopectin is retarded in the presence of ALC's (Gudmundsson, 1992; Gudmundsson & Eliasson, 1990). Czuchajowska, Sievert & Pomeranz (1991) demonstrates that the ALC crystallisation occurs instead of recrystallisation that accompanies retrogradation, the extent of which depends on amylose content. Long pasting times in conjunction of stearic acid lead to a large reduction in retrogradation rate during cooling and ageing (D'Silva, Taylor & Emmambux, 2011). S Wang, J Wang, *et al.* (2016) showed that the rate retrogradation in the presence of fatty acids can also be manipulated by the length of the aliphatic chain.

2.7 Deep eutectic salts background

So far the research has centered around starch, but a wide variety of other compounds may be suitable. A different substance, i.e. a eutectic salt, is also considered as a matrix for the chosen active ingredient. Stott, Williams & Barry (1998) defines a eutectic mixture as a combination of multiple components which usually do not interact to form a new chemical compound. At certain ratios, the crystallisation process will be inhibited/retarded. This results in a system having a lower melting point than its constituents. Many salts decompose prior to melting, adding to the usefulness of the thermodynamic event (Hasnain, 1998).

2.7.1 Eutectic physical chemistry

This section is adapted from Atkins, De Paula & Keeler (2018: 177) to help illustrate the thermodynamic phenomenon. Consider composition a_i on Figure 14.

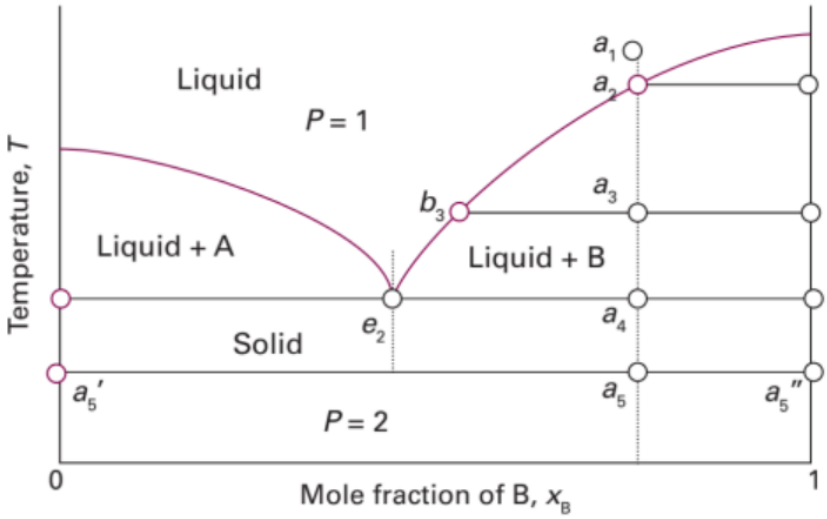

Figure 14: The temperature-composition phase diagram for two immiscible solids and their completely miscible liquids. Adapted from (Atkins, De Paula & Keeler, 2018).

- $a_1 \rightarrow a_2$ The system enters the two-phase region labelled 'Liquid + B'. Pure solid B begins to crystallize out of solution. This occurs at a lower temperature than the melting temperature of one or more of the components, in this case, B.
- $a_2 \rightarrow a_3$ More of solid B forms and the remaining liquid becomes richer in A. The relative amounts of the solid and liquid phases (which are in equilibrium) are given by the lever rule.

- $a_3 \rightarrow a_4$ At the end of this step, there is less liquid than at a_3, and its composition is given by the isopleth e_2. The liquid now freezes to give a two-phase system of pure B and pure A.
- $a_4 \rightarrow a_5$ The solid formed at a_4 cools with no surrounding liquid.

If the isopleth a_i, were to have occurred at the eutectic composition, e_2, a eutectic solid would form. This melt mixture would crystallize in nearly homogeneous microcrystals with regular ordering (Atkins *et al.* 2018: 177). Eutectic halt is defined as the steady cooling of liquid parts in a solidifying system whereby the exothermic crystallisation of one phase occurs in a eutectic system. This halt is most pronounced at the eutectic composition. This makes thermal analysis an ideal tool to analyse eutectic systems (Atkins *et al.* 2018: 187)(Stoler & Warner, 2015).

Thermal analysis and analysis in sample morphology (via XRD and SEM) is often used when investigating eutectic systems. These analysis techniques may display the occurrence of co-crystallisation, whereby a crystalline phase is formed composed of multiple compounds (Stoler & Warner, 2015). This will occur if the two compounds are slightly miscible as solids. The new co- crystal phase can be detected by the appearance of new diffraction reflections on the Powder XRD (PXRD) pattern, which cannot be assigned to the pure constituents. Figure 15 is a set of diffractograms of compounds that co-crystallise in specific ratios. The diffractogram reflections (peaks) of the mixture are not all present in any of the parent components. A reflection at 17.5° on Figure 15 is a good example of this.

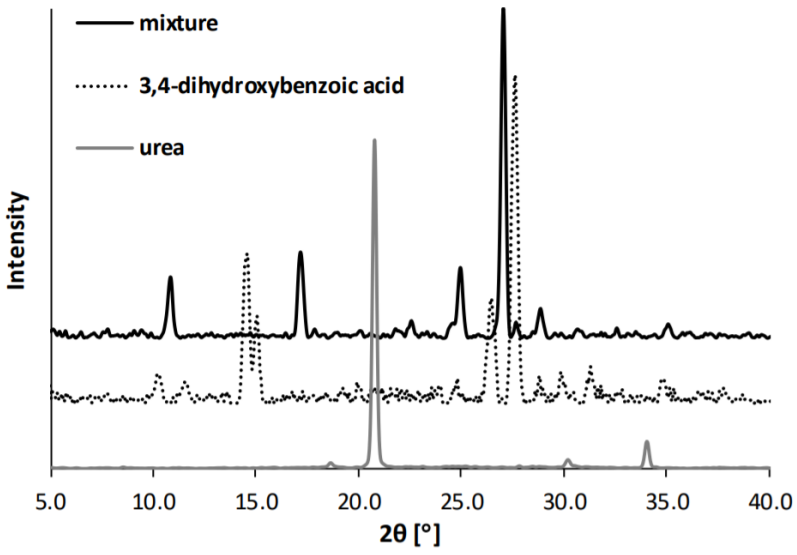

Figure 15: PXRD pattern of the urea & 3,4-hydroxybenzoic acid system displaying co-crystallisation. From (Przybyłek & Cysewski, 2018).

If a mixture of two solid components do form a eutectic at a certain composition, every reflection of the mixture diffractogram will be present in at least one of the parent components (Przybyłek & Cysewski, 2018; Stoler & Warner, 2015). Figure 16 displays the diffractograms of a eutectic composition and the co-formers of that eutectic system.

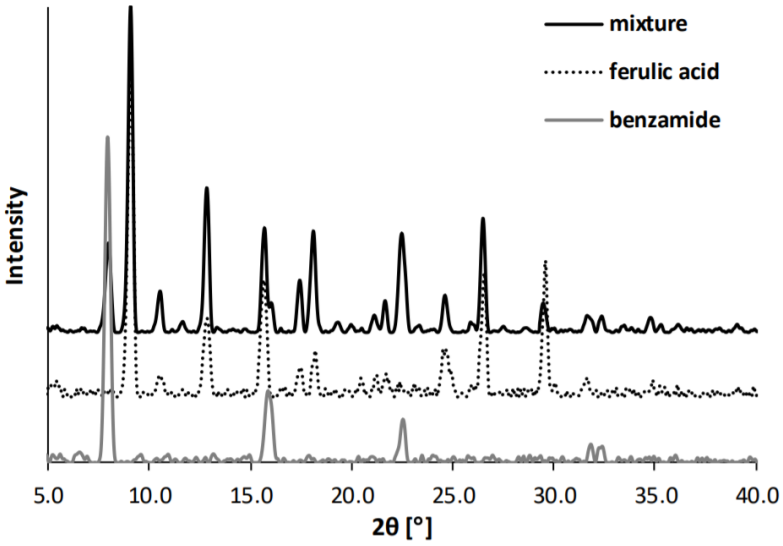

Figure 16: PXRD pattern of benzamide-ferulic acid system showing eutectic behaviour. From (Przybyłek & Cysewski, 2018).

Co-crystallisation occur to varying degrees. Some systems display new co-crystal phase reflections with a very low intensity. This indicates a low degree of co-crystallisation, and thus limited solubility of the constituents in the solid phase (Stoler & Warner, 2015).

2.7.2 Eutectic modelling

Ideal eutectic systems are modelled by the following relations shown in Equation 1 and Equation 2:

$$Rln(x_i) = \frac{H_i^\circ}{T_i^\circ} + \frac{H_i^\circ}{T} \tag{1}$$

$$\sum_i x_i = 1 \tag{2}$$

where H_i° is the standard enthalpy of fusion of a component, and T_i° refer to the melting point of that pure component.

Here T models the temperature at which a two phase mixture would exist at that composition, x_i. When significant deviations occur from this model, the components display interaction, which can be modelled by a suitable activity coefficient model as shown in Equation 3.

$$Rln(\gamma_i x_i) = \frac{H_i^\circ}{T_i^\circ} + \frac{H_i^\circ}{T} \tag{3}$$

In cases where significant deviation did occur the following activity coefficient models where considered and compared:

- Porter thermodynamic model
- Margules activity model
- Wilson thermodynamic equations

2.7.3 Eutectics as matrices for solid dosage forms

Organic eutectic salts have been used as matrices for pharmaceuticals, and is gaining traction as a useful material in medical applications (Abbott *et al.* 2017). Cherukuvada & Nangia (2014) have investigated the properties, design and characterisation of organic eutectics in pharmaceutical materials and has proven its advantages as a novel composite material. The possibility of the liquefication, and thus latter size reduction of recrystallised particles may occur in co-crystals of organic salts (Bica *et al.* 2011).

One of the categories of drug carrier that will be investigated in this research is that of urea based eutectic mixtures. These compounds are often prepared using the melting method consisting of two carrier compounds which are known to form a eutectic. These two constituents are also completely miscible when molten and display limited solid-solid solubility and co-crystallisation.

Urea is known to form eutectic and co-crystallising systems with a multitude of other organic salts. In this study two compounds, namely 1,3-dimethylurea and acetamide, will be investigated as the second constituent of the eutectic solid dosage form matrix. Fahy (2010) speculates that acetamide is toxic at levels above 35 wt.% where its carcinogenic characteristics are no longer negligible.

Law *et al.* (2003) in their study, regarding the use of a eutectic mixture of polyethylene glycol and fenofibrate, noted that a remarkable decrease in the size of fenofibrate crystals occurred after melt casting. Other studies in which ketoprofen (Margarit, Rodriguez & Cerezo, 1994) and hydroflumehiazide (Corrigan, Murphy & Timoney, 1979) together with polyethylene glycol, formed a eutectic. Both also found that a reduction in size of the active ingredient crystals occurred. The effect of the reduction of particle size on the dissolution rate of the solid dosage form was quantified. In all the listed investigations the smaller particle size lead to an increased dissolution rate. This faster rate of dissolution may be due to the reduction in particle aggregation and agglomeration as illuded by Chiou & Riegelman (1971).

Jung *et al.* (1999) state in their results that the reduced particle size, increased surface area, and the close contact between the hydrophilic carrier and hydrophobic drug may be responsible for the changes in rate of dissolution and solubility. This, according to later studies by Hülsmann *et al.* (2000), was concluded to be due to the increased wettability of the hydrophobic drug.

2.8 Dissolution kinetics of solid dosage forms

The dissolution speed of solid dosage forms is a measure of how quickly an active ingredient is released. This rate of released is important to determine the application of the compound. The rate of dissolution in water will be modelled on principles used in the pharmaceutical industry. In order to distinguish between two interrelated concepts, the terms; solubility and dissolution will be defined as follows:

Solubility is a thermodynamic property which defines the capacity of a solute to dissolve in a pure solvent. Dissolution is a kinetic process. The dissolution rate defines the tempo at which a solute dissolves into the solvent (De Blaey & Van der Graaff, 1977). In many cases the solubility of a solute may be low, yet it dissolves rapidly into the accompanying solvent (Smith, 2015). In this study the dissolution rate is expressed in Equation 4 via the Noyes-Whitney equation (Heng *et al.* 2008):

$$\frac{dC}{dt} = \frac{DS(C_S - C)}{Vh} \tag{4}$$

where C describes the concentration of the solute in the solvent, C_S is the solubility limit of the solute in the solvent, D represents the diffusion coefficient which depends on the Reynolds number and thus rate of stirring and viscosity of the solvent, S describes the surface area that the solute is in contact with the solvent, V is the volume of the solvent used and h is the thickness of the boundary layer which depends on the diffusivity and thus viscosity and stirring speed as well. Equations 5 through 8 describe the geometrical relationships of spherical particles:

$$M = \frac{N\pi d^3 \rho}{6} \tag{5}$$

where the the mass of undissolved solutes M is equal to the volume of particles calculated from N, the amount of particles, and d the diameter of the average sized particle, divided by the particle density ρ. Equation 6;

$$S = N\pi d^2 \tag{6}$$

relates the average diameter and number of particles to the total exposed solid surface area S. Equation 5 can be manipulated to give the relation shown in Equation 7

$$\frac{M}{M_0} = \left(\frac{d}{d_0}\right)^3 \tag{7}$$

while Equation 6 brings about Equation 8 in a similar fashion

$$\frac{S}{S_0} = \left(\frac{d}{d_0}\right)^2 = \left(\frac{M}{M_0}\right)^{2/3} \tag{8}$$

The subscript 0 depicts an initial value. Equations 9 through 11 describe the conventions followed in the derivation of the rate equations used in this study:

$$m = M_0 - M \tag{9}$$

where m depicts the total mass of solute dissolved. Equation 10 relates the dissolved mass and volume of solvent to the concentration C of solute in the solvent.

$$C = \frac{m}{V} \tag{10}$$

Equation 11 shows that the ratio between the surface area, S, and mass of solids, M, remain unchanged

$$S_{SP} = \frac{S_0}{M_0} = \frac{6}{d_0\rho} \tag{11}$$

where S_{SP} is a geometrical constant known as the specific surface area of a sphere. The Noyes-Whitney equation as written in Equation 4 assumes a zero-order rate decrease of the solute, and when applying a sink condition Equation 12 is created:

$$\frac{dC}{dt} = \frac{DSC_S}{Vh} \tag{12}$$

and if the conventions and geometrical relationships shown in Equations 8, 9, 10 and 11 are applied, an integratable form of the Noyes-Whitney equation is shown in Equation 13 after manipulation of Equation 12 and the geometrical relations in Equations 5 through 11:

$$-\frac{dM}{dt} = \frac{DS_{SP}M_0^{1/3}M^{2/3}C_S}{h} \tag{13}$$

After minor manipulation, Equation 14 is ready for integration from the initial condition until time t:

$$\int_{M_0}^{M} -M^{-2/3} dM = \int_0^t \frac{DS_{SP} M_0^{1/3} C_S}{h} dt \tag{14}$$

which gives rise to Equation 15

$$M_0^{1/3} - M^{1/3} = \left(\frac{2DC_S}{\rho h}\right)\left(\frac{M_0^{1/3}}{d_0}\right) t \tag{15}$$

which can be rewritten into Equation 16

$$\sqrt[3]{M_0} - \sqrt[3]{M} = k'\left(\frac{\sqrt[3]{M_0}}{d_0}\right) t \tag{16}$$

which clumps the solute-solvent and experiment specific parameters into a new coefficient k' which is known in this study as the intrinsic rate constant. This equation is further modified to give Equation 17 which is commonly known as the Hixson Crowell cube root law. De Blaey & Van der Graaff (1977) amends the derivation in order to accommodate for more complex particle geometries.

By inspection of Equation 15 and Equation 16, the intrinsic rate constant, k', depends on the density, solubility and diffusivity of the particle as well as the dissolution boundary layer. For the purposes of this research the intrinsic rate constant is communicated to report the rate of dissolution of the particles created in this study without geometrical and initial mass dependencies.

The Hixson Crowell cube law in its native form is used to model the isotropic dissolution of spherical particles. It can however be amended for various geometries (De Blaey & Van der Graaff, 1977). The modified Hixson Crowell dissolution model used in this study is presented in Equation 17 and Equation 18 for spherical particles and Equation 19 for disks and cylinders.

$$\sqrt[3]{M_0} - \sqrt[3]{M} = kt \tag{17}$$

$$k = k'\frac{\sqrt[3]{M_0}}{d_0} \tag{18}$$

$$k = k' \frac{\sqrt[3]{M_0}}{\sqrt[3]{H_0 d_0^2}} \tag{19}$$

The subscript 0 indicates an initial amount. The cube root rate constant, k, is split into geometric and intrinsic properties by Equation 18 or Equation 19, depending on the geometry of the particle. The intrinsic rate constant, k', is known to be dependent on the diffusivity, solubility, density and dissolution film size. If a zero order rate decrease is assumed as per the Noyes-Whitney equation, the relation between the intrinsic rate and film thickness, h, is inversely proportional as displayed in Equation 20.

$$k' \alpha \frac{1}{h} \tag{20}$$

To compare across samples of varying composition and geometry, the percentage difference in film thickness is often compared as well as the fitted intrinsic rate constant.

3 Experimental design

3.1 Materials

3.1.1 Amitraz

Amitraz is the acaricide chosen for this work. It is a dark yellow to brown powder with a molecular weight of 293.4 g·mol^{-1} (National Center for Biotechnology Information, 2020). The substance melts at 86 °C and is very hydrophobic and thus only practically insoluble in water at room temperature and pressure ($<$ 1 mg·L^{-1}) (ILO, 2020). It is far more soluble in organic solvents, but may become unstable in acid solutions where it may undergo further hydrolysis. The compound has many crystalline states, but is considered to be very stable in its solid form, and does not degrade below 400 °C (Villiers *et al.* 2004). The amitraz used in this investigation was supplied by Bayer as a powder, marketed as 98.5 % AmitrazTech R44/2004.

3.1.2 Dextrin and thermoplastic dextrin additives and plasticizers

Stydex White Dextrin 072012 was obtained from Tongaat Hullet in powder form. The particle size was of the raw powder materials (dextrin, CNF and amitraz) are reported in the Powder Analysis subsection. The molar mass and degree of polymerisation were quantified via MALDI-TOF, rheology, and intrinsic viscosity.

Deionised water was used in all suitable analysis experiments and in the gelatination of starch where it would act as plasticiser. Glycerol, used as a second plasticiser was obtained from ACE (Associated Chemical Enterprise) at a purity of >99.5 wt.%.

Several additives were investigated for use in the thermoplastic composites. As control additive, inert glass beads were used. Spherical 4070AH glass beads (40 μm) were supplied by Blastrite. Grade Pristirine 4989 stearic acid was supplied by Protea Chemicals. The stearic acid would serve as fatty acid additive to investigate amylose-lipid complex (ALC) formation and its effects. Sappi donated Valida-Visco-L, a fibrillated nano-cellulose fibre suspension containing 13.4 wt.% solids. The cellulose nanofibre (CNF) was chosen to strengthen the matrix if necessary. CNF may also act as moisture competition with the dextrin to perhaps combat retrogradation. The layered double hydroxide (LDH) nanoclay, hydrolcalumite grade B44 LDH, was kindly donated by Jan Mentz and Greenfield Additives. It is hypothesised that the LDH would strengthen the thermoplastic dextrin (TPD) matrix and slow the rate of dissolution in water.

To quantify the rate of dissolution of the TPD compounds, an Iodine indicator was created. Vähäsalo & Holmbom (2004) prescribes adding 2 mL of a 0.1 M iodine solution in a 1 L dispersion of starch. The iodine solution was prepared by mixing 20 g KI (anhydrous potassium hydroxide obtained from Sigma-Aldrich; CAS no. 7681-11-0) and 6.4 g iodine beads (99.7 % obtained from Sigma-Aldrich; CAS no. 7553-56-2) in 500 mL deionised water.

3.1.3 Urea based eutectic compounds

Urea (CAS no. 57-13-6), acetamide (CAS no. 60-35-5) and 1,3-dimethylurea (also depicted as N,N'-dimethylurea; CAS no. 96-31-1) were obtained from Sigma-Aldrich at a purity of 98 %, 99 % and 99 % respectively. All of the above salts display high solubility in water. Acetamide and dimethylurea are known to be highly hygroscopic, and thus were dried over silica gel prior to use.

The quantities of the physical properties of the salts are summarised in Table 2. These values were used to create the eutectic plots displayed in the document.

Table 2: Organic salt physical properties.

Name	Molar mass [g ·mol^{-1}]	Melting point [°C]	Enthalpy of fusion [kJ·mol^{-1}]
Urea	60.06	132.7	14.6
N,N-dimethylurea	88.11	102.3	13.6
Acetamide	59.07	81	15.6

3.2 Methods

3.2.1 Thermoplastic starch batch preparation

Befor compounding with the active ingredient, several candidate matrices were first evaluated. The most suitable matrix would be chosen from one of nine TPD batches. All TPD combinations consisted of 60 wt.% dextrin, 18 wt.% water, 18 wt.% glycerol, and 4 wt.% additive. Each batch is named according to the additive/additive combination used. Each batch is summarised in Table 3. Sample S0 was only used in the particle size analysis of the Thermoplastic dextrin composites as matrices for solid dosage forms subsection. The hydrocalumite LDH was used in a milled and unmilled form. The unmilled form was used as received.The milled form was prepared by grinding in batches using a Netsch LME1 laboratory scale horizontal stirred mill. The mill was controlled to 2 000 RPM with the milling chamber filled with 250 μm zircon beads. Batch sizes were 8 L of a 10 wt.% LDH slurry. After milling, a recirculating flow protocol was sustained for three hours.

Table 3: Premix compositions of TPD composites.

Sample	Dextrin [wt.%]	Water [wt.%]	Glycerol [wt.%]	Nanofiller [wt.%]			
				Glass beads	LDH	Stearic acid	CNF
S0	60	20	20	-	-	-	-
S1	60	18	18	4	-	-	-
S2	60	18	18	-	4[a]	-	-
S3	60	18	18	3	-	-	1
S4	60	18	18	-	-	4	-
S5	60	18	18	-	4[b]	-	-
S6	60	18	18	-	2[a]	2	-
S7	60	18	18	-	-	3	1
S8	60	18	18	-	3[a]	-	1
S9	60	18	18	-	1.5[a]	1.5	1

[a]LDH in an unmilled form. [b]LDH in milled form.

All sample batches were manually mixed prior to extrusion. Whenever stearic acid was used as additive the approach was slightly different to ensure good mixing. It was first blended with small amounts of dry using a Pyramid Sigma Super Grinder. This mixture would then be dispersed in the rest of the dry batch before adding the plasticizer mix.

The LDH and/or CNF additives were mixed into the plasticiser with a Silverson L4RT high shear mixer at 6000 RPM for 15 minutes before combining it with the starch.

The TPD composite labelled was subsequently chosen as matrix for compounding with amitraz. The motivation for selecting this specific TPD is discussed in the Results and Discussion section. Three amitraz loadings were investigated, namely 5 wt.% (A5), 10 wt.% (A10) and 20 wt.% (A20), where the remaining fraction consists of the composition specified for S7 in Table 3. Another sample, with the same composition to that of S7 was also extruded as control compound called A0. During batch preparation, the active ingredient would be systematically added to the plasticiser, CNF mixture when prepared in the high shear mixer.

3.2.2 Thermoplastic dextrin extrusion and film preparation

The premixed raw materials were melt-compounded on a ThermoFischer TSE 24 twin-screw co-rotating compounder (24 mm ϕ and 30 L/D). The screw speed was varied in the range of 50 to 80 RPM depending on the ease of feeding. The temperature profile was 60/80/100/110/110/110/110 °C. The extruded strands (5.5 mm ϕ) were collected and held overnight at -10 °C before granulating.

When compounding with amitraz, the temperature profile was lowered. This was done to compensate for the decrease in viscosity obtained when amitraz melts. The 5 wt.% (A5) and 10 wt.% A10) loadings were extruded using a 60/80/90/100/100/100/100 °C temperature profile while 20 wt.% loading was operated at 60/80/90/95/95/95/95 °C.

For some analyses (DMA and XRD), a flattened extrudate was required. This was achieved by re-compounding the granulated extrudates at the same processing conditions, but without the die attachment. The hot melt was flattened between two metal plates separated by a die frame of height 1.6 mm. Two polyester films were used to avoid adhesion to the plates.

After melt processing and granulation, all granules and films were stored in a humidity chamber. The relative humidity was set to 75 % at room temperature via a presence of a supersaturated sodium chloride solution (Greenspan, 1977). This was done to achieve a controlled atmosphere during storage and ageing for retrogradation studies.

3.2.3 Thermoplastic starch dissolution experiments

The granulated samples were sieved and the granules in the size range of 4.00 to 4.75 mm were collected. The 0.1 M iodine solution was used as indicator for the determination of the temporal variation of the starch concentration in each dissolution experiment. Spectra were recorded on a PG Instruments T60 UV-visible Spectrophotometer. The dissolution of the water-soluble dextrin was used as a proxy for the release of the amitraz. The absorbance measured at a wavelength of 580 nm. Beer-Lambert's Law was used to generate the calibration curve based on a range of dextrin solutions (Vähäsalo & Holmbom, 2004).

Duplicate dissolution experiments were conducted for each sample in a laboratory temperature-controlled to 20 ± 1 °C. In each case, approximately one gram of the sieved granules was added to a 1.0 L Erlenmeyer flask containing 500 mL deionized water and 2.00 mL of the 0.1 M iodine solution. The flask contents were vigorously agitated using a magnetic stirrer operating at a speed set to 200 RPM. At intermittent times, 5.0 mL sample liquid was removed from the flask and rapidly filtered. The liquid filtrate was analysed in a polystyrene cuvette in the spectrometer and the dextrin concentration was calculated from the measured absorbance.

3.2.4 Melt casting

After eutectic modelling and freezing curves were completed, specific systems were chosen to be cast into disks with various diameters. Two polypropylene mould sizes (55 mm ϕ and 100 mm ϕ) are reported in this document. The height of the disks in the moulds were kept the same (5 mm). The molten salts were poured into the mould well above the disks' melting point, and then sealed with a polypropylene lid. The moulds were then placed in a refrigerator at 2 °C for one hour. Each sample was then removed from the mould and then placed in an air-tight container. Five sets of disks were created at each diameter.

When casting with amitraz, the pesticide powder, was added to the molten salts while in the moulds and then thoroughly mixed. A loading of 20 wt.% amitraz was used. Another five samples were made for each diameter.

3.2.5 Salt freezing curves

Cooling curves were generated using the following typical procedure: Predetermined quantities of urea and 1,3-dimethylurea were weighed into a test tube. The test tube was partially submerged in silicon oil contained in a beaker placed on a heater-stirrer. The contents were heated until the test tube contents were fully molten. The molten mixture was agitated with a glass rod to ensure complete homogenization of the contents. The heater was switched off, while the stirrer was kept on during this cooling phase.

The change in temperature over time was tracked with a Hairuis Model SSN-61 temperature data logger. Care was taken that the thermocouple inserted into the test tube did not touch the glass walls. In most cases, sub-cooling occurred as indicated by a sudden rise in the temperature when freezing commenced. After the peak temperature was used as the equilibrium crystallization temperature for the corresponding composition. Duplicate runs were conducted for each composition considered.

3.2.6 Eutectic salt dissolution experiments

The dissolution of the discs was tracked gravimetrically. Triplicate determinations were made according to the following procedure: Prior to each experiment, the discs were weighed using a Radwag PS 360/C/2 laboratory scale. They were then placed in a 2 L beaker filled with 1 L of deionized water, which was agitated with an overhead WiseStir HS-120A stirrer set to 200 RPM. The discs were temporarily removed and weighed at regular intervals.

3.3 Characterisation methods

3.3.1 Particle size distribution (PSD)

Particle size analysis was conducted on a Malvern Mastersizer 3000. The wet dispersion of the solid powders for particle size analysis was controlled with a Malvern LV Hydro. The ultrasound setting was 20% and the shear mixer was set at 3 500 rpm. The reported values represent averages of five measurements. The particle size distributions of the neat amitraz powder and the dispersions obtained after the completion of the dissolution experiments were determined.

3.3.2 Molar mass characterisation of dextrins

Matrix-assisted laser desorption/ionization using time-of-flight mass spectroscopy (MALDI-TOF MS)

The molar mass of carbohydrate polymers can be measured by MALDI-TOF MS up to 10×10^6 g· mol^{-1} (Garrozzo *et al.* 1995). The characterisation requires ionisation and desorption of the bio-molecules in a matrix. In this study the matrix used was a 2 % solution of acetic acid in water. Approximately 10 mg of dextrin was used per analysis in 1 mL of the solution while heated for one hour at 60 °C while sonicating in an AutoflexTOF. The MALDI-TOF molar mass analysis was confirmed via two viscosity tests.

Rheology based molar mass characterisation

A solution containing 10 % (w/v) of dextrin and deionised water was created. The viscosity of this sample was analysed at 30 °C at a shear rate of 160 RPM with a Brookefield DV-111 Ultra programmable rheometer and repeated three times per sample analysis (Sun *et al.* 2010).

Intrinsic viscosity relation

The intrinsic viscosity of the dextrin was measured at 45 °C in a 0.02 M solution of sodium nitrate using an Ubbeholde OC viscometer. All Ubbeholde experiments were duplicated with different dextrin solutions. In order to ensure full dissolution of dextrin in solution it was first heated to 65 °C until a clear homogeneous solution is obtained.

3.3.3 Moisture content

An Ohous MB35 moisture analyser was used to quantify the moisture content of the conditioned compounds. Each moisture content analysis was duplicated. The analyser was used in the “auto” setting at a controlled temperature of 120 °C.

3.3.4 Dynamic mechanical analysis (DMA)

Rectangular specimens (35 x 10 mm) were cut from flattened extruded samples.. The thickness was measured with a Mitutoyo RHS 769 micrometer. A Perkin Elmer Dynamic

Mechanical Analyzer 8000 was used in a single cantilever bending geometry at a frequency of 1 Hz with a strain amplitude of 0.020 mm. The strain amplitude chosen was deemed suitable as it did not damage the sample in its frozen state for any composition. A temperature scan experiment type was set to a scanning rate of 10 °C·min^{-1} from -90 °C to 25 °C. All glass transition and β transition temperatures were found to lie in this range. Analyses were performed in duplicate.

3.3.5 X-ray diffraction (XRD)

XRD measurements were performed on a Bruker D8Advance diffractometer set to 2.2 kW CuKα radiation with a corresponding wavelength of 1.54060 nm and LynxEye detector with 3.7° active area. Flattened TPD samples were cut into round discs of 22 mm diameter. The samples were scanned in reflection mode form 2° to 70° 2Θ at a rate of 0.02°· s^{-1} with generator settings of 40 kV and 40 mA. For the TPD samples, XRD scans were performed the first day after extrusion (Day 1). The samples were then stored at constant relative humidity and then on days specified in the Results and Discussion section, were analysed again with the diffractometer. Samples of the pure materials were subjected to the same analysis protocol in order to obtain characteristic diffractograms used to identify reflections associated with each of the components. The ICDD database PDF-2 2015 was used for phase identification and the ICDD PDF card reference for each of the starting materials is cited in the discussion part of the text.

Relative crystallinity was estimated as the ratio of the area of crystalline reflections after baseline subtraction to that of the area of the original diffractogram. Savitzky-Golay smoothing was used on the original diffractogram data. After baseline subtraction the crystallinity of each individual crystalline element was estimated via integration of that subtracted reflectance and dividing by total crystalline reflectance area after baseline subtraction (Frost *et al.* 2009). Figure 17 displays an example of how the baseline looks after being calculated and fitted, and then subtracted.

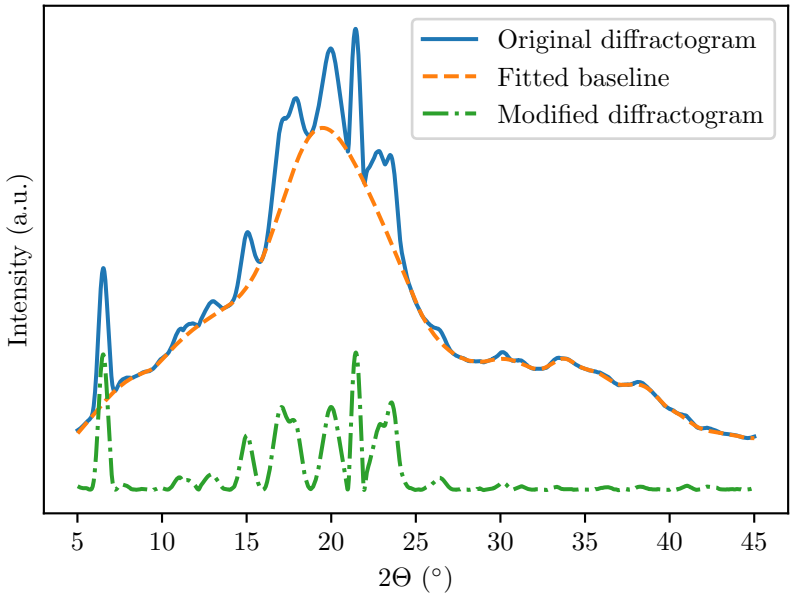

Figure 17: Visualisation of diffractogram data handling, exemplified by sample S4's day 1 diffractogram.

3.3.6 Thermal gravimetric analysis (TGA)

Thermal property tests of the TPD compounds were completed in a TA Instruments SDT Q600. Aged samples of roughly 4 g were analysed in air at a ramp rate of 10 °C ·min^{-1} from 20 °C to 900 °C.

3.3.7 Differential scanning calorimetry (DSC)

TPD composite high pressure DSC (HPDSC)

Morphological and thermal stability properties of the extruded materials were also analysed using a HP SC827e, Mettler Toledo machine under a nitrogenous pressurised atmosphere at 4 MPa, in order to inhibit moisture loss. An empty aluminium pan (100 μL) was used as reference. Approximately 40 mg was sealed into a perforated aluminium pan. Samples were heated from 20 °C to 200 °C at a heating rate of 10 °C·min^{-1}. The indium calibration standard was chosen for analysis of all samples.

Urea-based eutectic DSC

The cast samples and active ingredient were analysed using a Perkin Elmer DSC 4000 with aluminium pans (40 μL containing approximately 12 mg of the samples). The DSC method for these samples are summarised:

- Isothermal at 20 °C for 2 min.
- Heat from 20 °C to 140 °C at 5 °C·min^{-1}.
- Isothermal at 140 °C for 2 min.
- Cool from 140 °C to 20 °C at 5 °C·min^{-1}.
- Isothermal at 20 °C for 2 min.
- Heat from 20 °C to 140 °C at 5 °C·min^{-1}.
- Isothermal at 140 °C for 2 min.
- Cool from 140 °C to 20 °C at 5 °C·min^{-1}.

This method was followed in order to understand the melting and freezing phenomena of the tested compounds when containing excess moisture and then when dried. The eutectic phase changes are known to be very slow, hence the different method as compared to the thermoplastic dextrin DSC analysis.

3.3.8 Cryogenic scanning electron microscopy (CSEM)

The morphology of granulated TPD samples were viewed using a Zeiss Supra 55 FEGSEM. The TPD samples were imaged in granular form. The granules were frozen using liquid nitrogen and then hammered into smaller fractures. The samples were sputter coated with carbon and viewed in the analysis machine at 5 kV.

3.3.9 Attenuated total reflectance Fourier transform infrared spectroscopy (ATR/FTIR)

TPD granule samples were analysed to investigate the influence of additives on organic functional groups. Absorbance spectra were recorded on a Perkin Elmer Spectrum 100 using the single reflection ATR diamond crystal. All spectrograms were obtained at a resolution of 4 cm^{-1} as the average of 32 scans.

4 Results and Discussion

4.1 Powder Analysis

Three partially soluble powders, namely amitraz, dextrin and cellulose nanofibres (CNF), were analysed. These powders were used in the first candidate matrix and the final compound. Figure 18 shows the particle size distribution of the raw powders used. Amitraz formed a unimodal distribution, while dextrin and CNF were both multimodal. The insoluble residue of dextrin are likely due to a metastable region of solubility in water. Full dissolution of the starch powder occurred by first heating to 60 °C and then cooling to room temperature as shown in the Degree of polymerisation characterisation of dextrin starch section of the results.

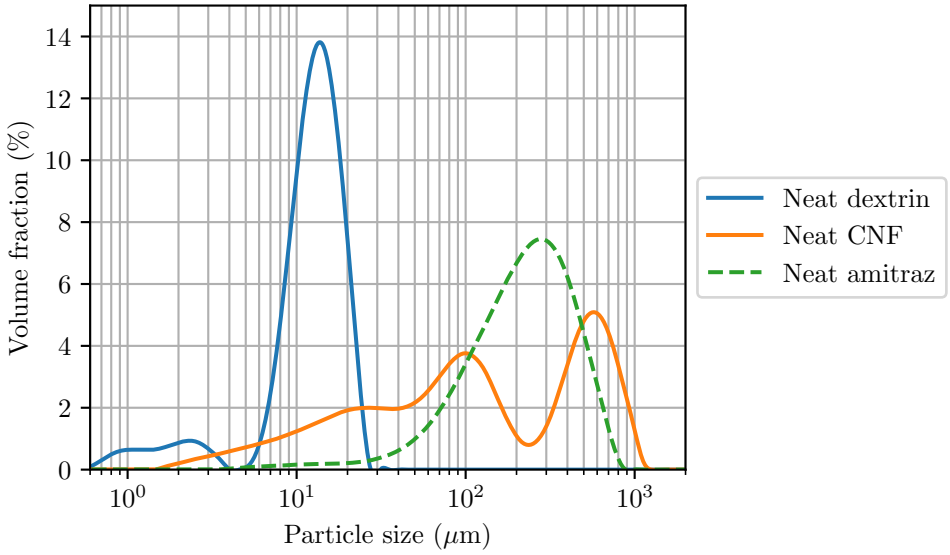

Figure 18: Raw material particle size distributions

.

Table 4 summarizes the results of the PSD. Averages and standard deviations are shown for each sample's five measurements.

Table 4: Particle size values for the neat powder materials used in this research.

Sample	D10 (μm)	D50 (μm)	D90 (μm)
Amitraz	80.8 ± 3.7	240 ± 10	511 ± 28
Dextrin	6.78 ± 0.04	13.5 ± 0.1	20.7 ± 0.1
Cellulose nanofibre	12.1 ± 0.2	114 ± 2	725 ± 9

4.2 Thermoplastic dextrin composites as matrices for solid dosage forms

4.2.1 Degree of polymerisation characterisation of dextrin starch

Figure 19 shows the results obtained from the MALDI-TOF analysis of the neat dextrin starch as obtained from the method described in the Characterisation methods subsection. The figure shows repeat experiments on 2 separate samples of the dextrin under identical conditions. There is a clear difference in the result, implying an inconsistency in the experimental method. Starch is known to have very strong hydrogen bonding characteristics. This may be the cause of the inconsistency, as well as the very low molecular masses obtained from the result. The molar mass of a single glucose unit is approximately 180 g·mol^{-1}. The first (top) result shows clear regions that are multiples of this value i.e. 180, 360, 540, 720, 900, 1080 and 1260. The most intense regions appear to be those corresponding to a molar mass of one glucose unit indicating a very high level of hydrolysis of the dextrin. The analysis is very sensitive to lighter oligomers, and struggles to volatilise chains where there are more intermolecular forces holding them together (**byrd2000limitations**).

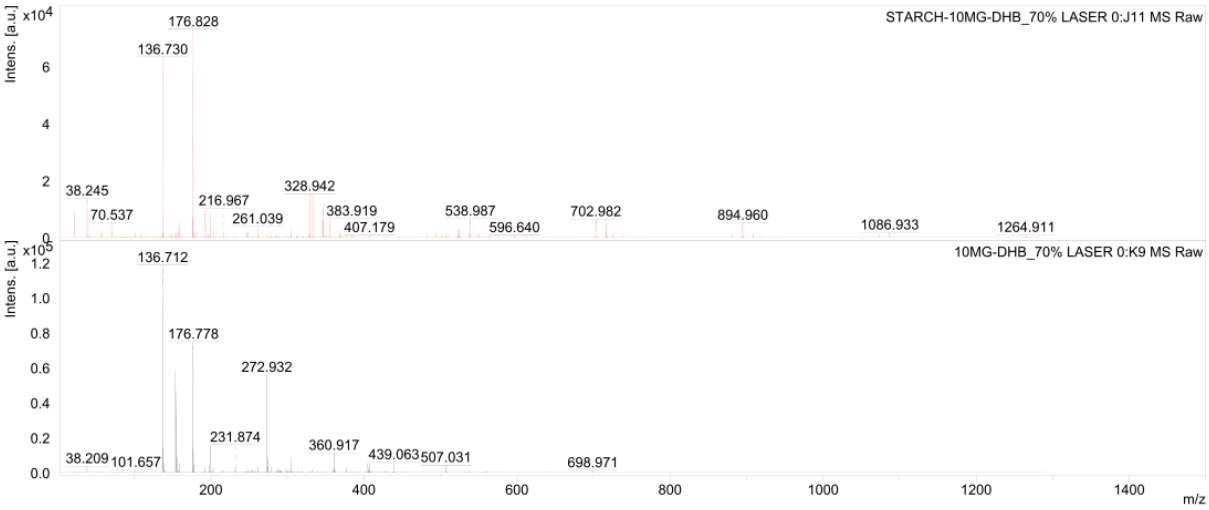

Figure 19: MALDI-TOF results of dextrin starch.

Sun *et al.* (2010) published a relationship between the average molar mass of a dextrin solution the the viscosity of the solution at a certain temperature and concentration. A dextrin solution consisting of 10 % (w/v) at 30 °C was analysed in The results from the Brookefield viscosity test as described by Sun *et al.* (2010) displayed a result of an average of 14.2 cP after three sets of experiments. This corresponds to a dextrose equivalent of approximately 24, via similar calculations done by Sun *et al.* (2010). This

dextrose equivalent is then converted to a degree of polymerisation of approximately 5.5. This value is clearly larger than the value that the MALDI-TOF analysis implies.

The third method to find the molar mass of the neat dextrin was to find the intrinsic viscosity of the polymer in solution as described in the Intrinsic viscosity relation explanation. Figure 20 shows the final Mark Houwink plot obtained from six duplicated experiments. Equation 21 relates the viscosity measurements obtained at various solute concentrations to the intrinsic viscosity.

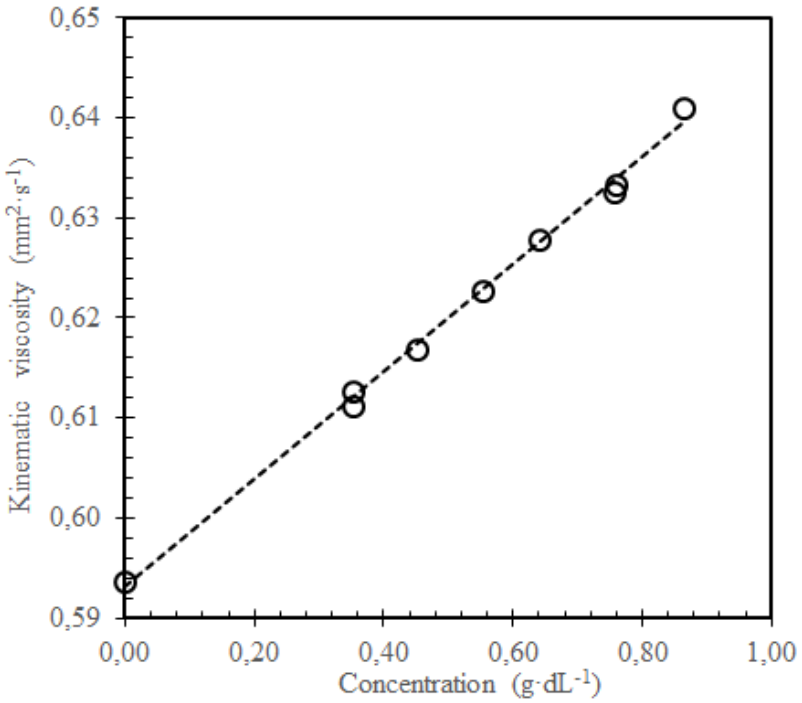

Figure 20: Mark Houwink plot of dextrin starch dissolved in a 0.01 M NaCl solution.

$$\nu = mc + \nu_0 \tag{21}$$

where ν and ν_0 represent the kinematic viscosity of the polymer solution and solvent respectively, $\overline{m}$ is the slope obtained from the regression and c is the concentration of polymer in solution. A least squares regression of the data with Equation 21 was completed. Table 5 summarises the regression statistics obtained.

Table 5: Summary of regression statistics for Mark Houwink plot.

	Value	Error	t Stat	P-value	Lower 95%	Upper 95%
ν_0 ($mm^2 \cdot s^{-1}$)	0,593	6.48×10^{-4}	914,1	4.9×10^{-19}	0.5916	0,5947
$\overline{m}$ ($mm^2 \cdot dL \cdot g^{-1} \cdot s^{-1}$)	0.054	11.1×10^{-4}	48.1	4.4×10^{-10}	0,0508	0,0561

Dividing by ν_0 and c and rearranging gives Equation 22:

$$\frac{\frac{\nu}{\nu_0} - 1}{c} = \frac{\overline{m}}{\nu_0} \tag{22}$$

where the term on the left is known as the reduced viscosity. The intrinsic viscosity is defined in Equation 23 as:

$$\lim_{c \to 0} \frac{\frac{\nu}{\nu_0} - 1}{c} = \lim_{c \to 0} \frac{\overline{m}}{\nu_0} \tag{23}$$

However the slope and ν_0 are independent of the concentration. This leads to Equation 24:

$$[\eta] = \frac{\overline{m}}{\nu_0} \tag{24}$$

where $[\eta]$ is the intrinsic viscosity of the polymer solution. Using the Mark Houwink relationship in Equation 25 and constants obtained from APSC, 2018, the average molar mass of the dextrin was obtained as 9 603 g $\cdot$ mol^{-1} with an error of 935 g $\cdot$ mol^{-1} This relates to a degree of polymerisation of 53 with a standard error of 5.

$$[\eta] = K(M_w)^a \tag{25}$$

4.2.2 Compositional analysis

The composition of the TPD composites were analysed using spectroscopy and various thermal analysis techniques. The aim was to investigate how closely the composition of the composite matches the batches described in Table 3.

Spectroscopy

In order to validate the incorporation of certain substances into the TPD, an FTIR-ATR absorption spectra was completed. Figure 21 show the results of the analysis of the TPD composites. There are distinct regions in the spectra which may indicate the presence, and to a less accurate extent, the amount of a certain additive added to the TPD.

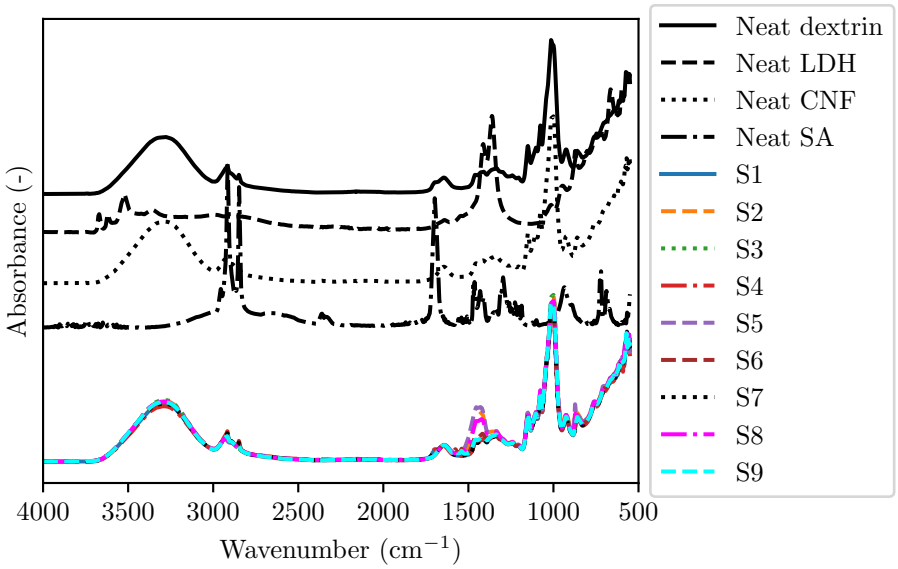

Figure 21: Absorption spectra of TPD composites and raw materials.

Cellulose and starch are both carbohydrates, and contain the same functional groups. The main difference is how the polymer chain is polymerised. Thus a significant difference in FTIR spectra is not expected. This analysis was completed however to investigate the effect of the additive purity, and shown in Figure 22.

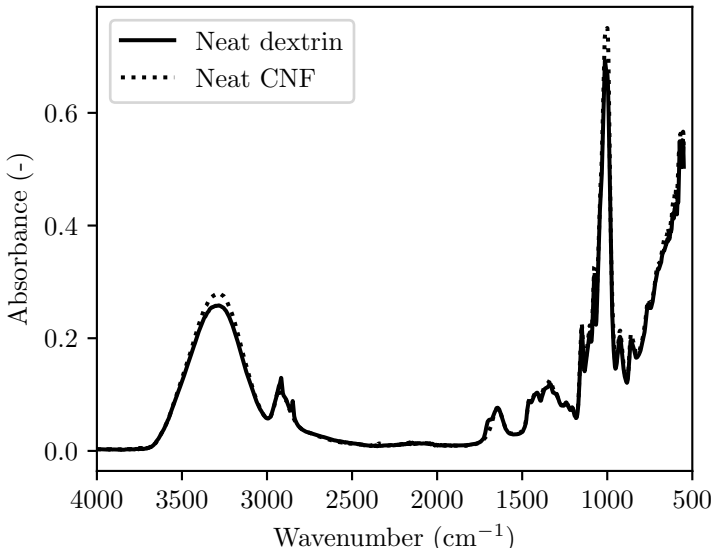

Figure 22: FTIR absorption of carbohydrate raw materials.

Two regions were identified in Figure 21 which may indicate the presence of stearic acid and LDH. Figure 23 shows the absorbances between 1300 and 1600 cm^{-1} wavenumbers. The absorbance shown by the neat LDH is believed to be what cause the absorbances

of S2, S5, S6, S8 and S9 to increase in this region, based on the analysis of the neat additives. The influence of LDH concentration is also notable on Figure 23, where S2 and S5 (which contain 4 wt.% LDH) display larger absorbances than that of S8 (3 wt.% LDH) which in turn is also more intense than S6 (2 wt.% LDH) which is also larger than S9 (1.5 wt.%).

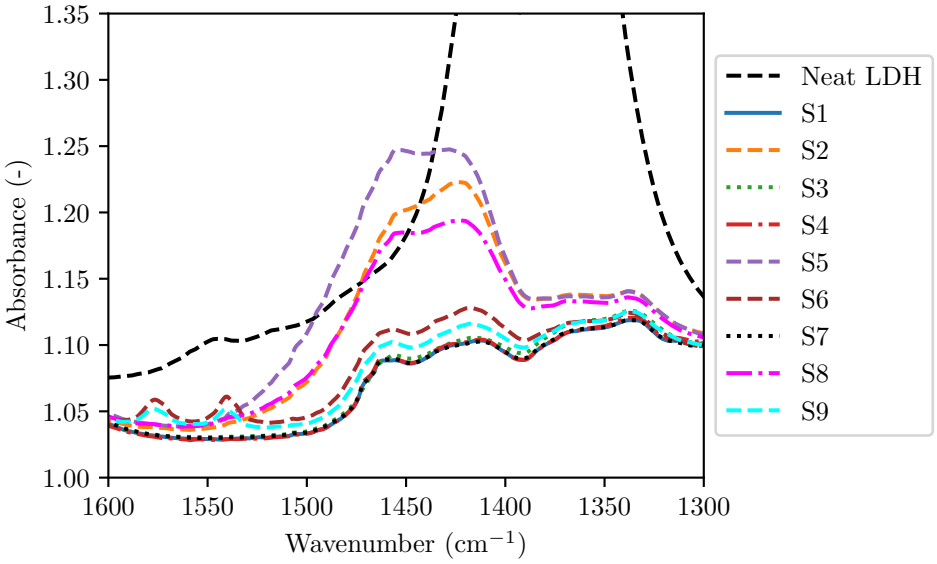

Figure 23: Effect of LDH on FTIR absorption.

The region identified to display the presence of stearic acid is shown in Figure 24. The two large absorbances of the stearic acid used (2850 cm^{-1} and 2925 cm^{-1}) are present on the TPD absorbances. The intensity of these absorbances match the trend of the loadings specified by Table 3. S4 (4 wt.% SA) shows absorbance values larger than that of S7 (3 wt.% SA) which is also larger than S6 (2 wt.% SA) which in turn shows more intense absorbances than S9 (1.5 wt.% SA).

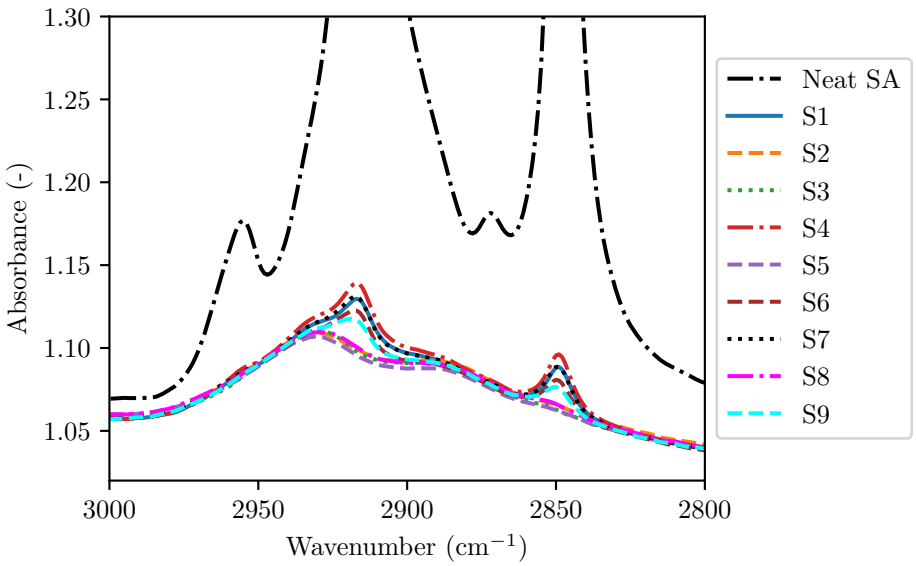

Figure 24: Effect of SA on FTIR absorption.

Figure 23 and Figure 24 thus prove that there was no contamination of stearic acid and LDH in any sample where these substances were not supposed to be. The same logic can be used for the clay additive, as no LDH absorbances are shown in samples where no LDH was added.

Thermogravimetric results

Thermogravimetry can be used to validate the incorporation of certain additives in a polymer and analyse the thermal stability of the compound. Figure 25 shows the thermograms of all the TPD composites when analysed using he procedure explained in the Thermal gravimetric analysis (TGA) section. The thermal gravimetric analysis (TGA), and derivative thermogravimetry (DTG) are used for the compositional analysis of the TPD composites. On initial visual inspection of the analyses, five thermal events occur:

- Mass loss associated with moisture release between 80 °C and 200 °C.
- Significant mass loss of LDH TPD composites (S2, S5, S6, S8, S9) beginning at 200 °C up to 340 °C.
- Degradation of all compounds from 280 °C to 340 °C.
- Sharp calcination and decomposition of LDH containing TPD composites (S2, S5, S6, S8, S9) between 420 °C and 470 °C.

- Gradual decomposition of TPD composites not containing LDH (S1, S3, S4, S7) between 350 °C to 550 °C.

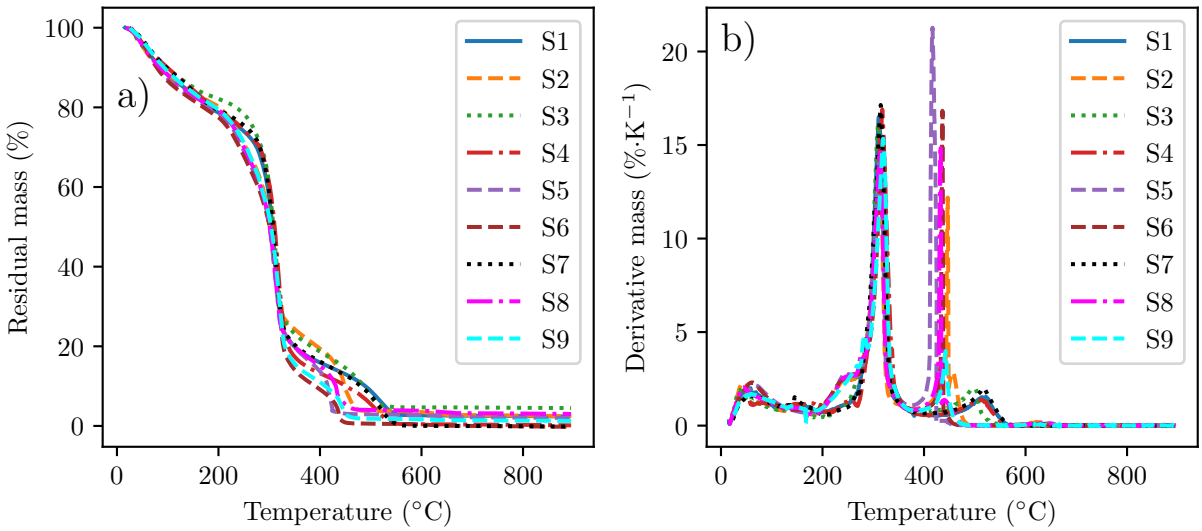

Figure 25: Thermoplastic starch TGA and DTG thermograms denoted by a) and b) respectively.

The initial continuous mass loss observed in Figure 26 may be attributed to moisture loss in the compounds, followed by a continuous degradation of the dextrin. All samples showed similar rates of moisture release indicating similar moisture content and spread.

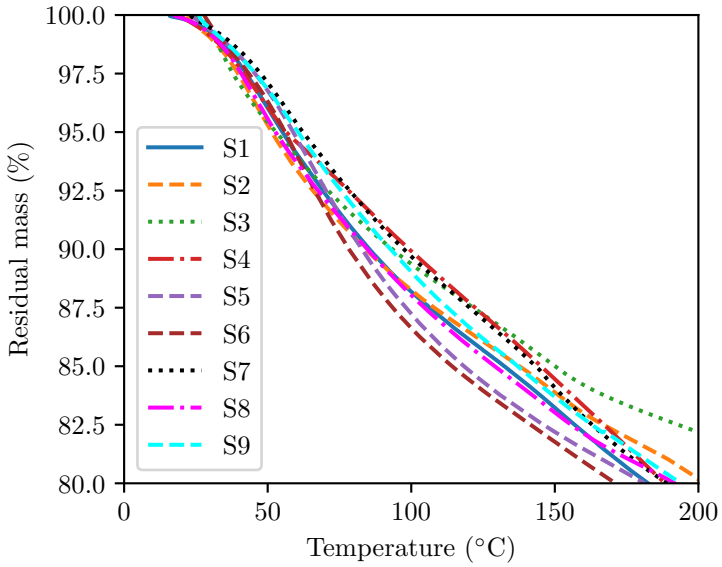

Figure 26: Thermoplastic starch moisture release and compound degradation.

After the moisture release (between 200 °C and 350 °C) the samples begin acting differently in the TGA. The samples containing hydrocalumite (LDH) reacted faster than

other TPD composites, shown by the larger DTG values shown in Figure 27. The other compounds were more stable prior to the onset of their degradation, starting at 270 °C. This thermal event is speculated to be linked to the combustion of the organic compounds in the composite.

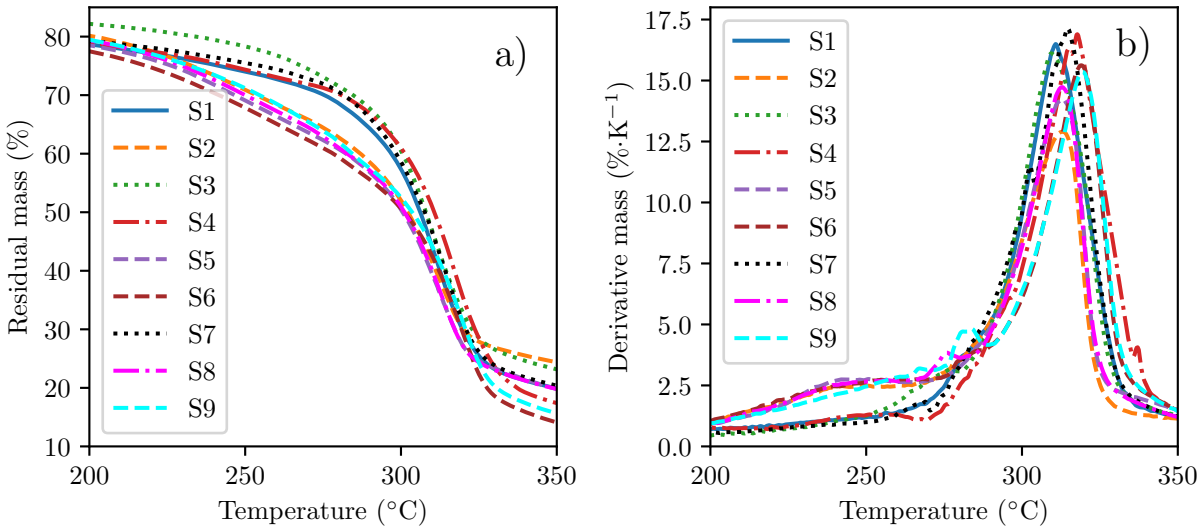

Figure 27: Calcination of LDH in TPD composites showing the TGA denoted by a) and DTG thermograms denoted by b).

Figure 28 shows the thermograms where the final carbon decomposition in the TPD samples occur between 350 °C to 550 °C. The DTG curves show a significant difference for the LDH containing compounds. This corresponds to the calcination of hydrocalumite (Tian & Guo, 2014). All compounds combust completely, however the LDH compounds show a final uncombusted residue ash at a residual mass similar to the specified loading in Table 3.

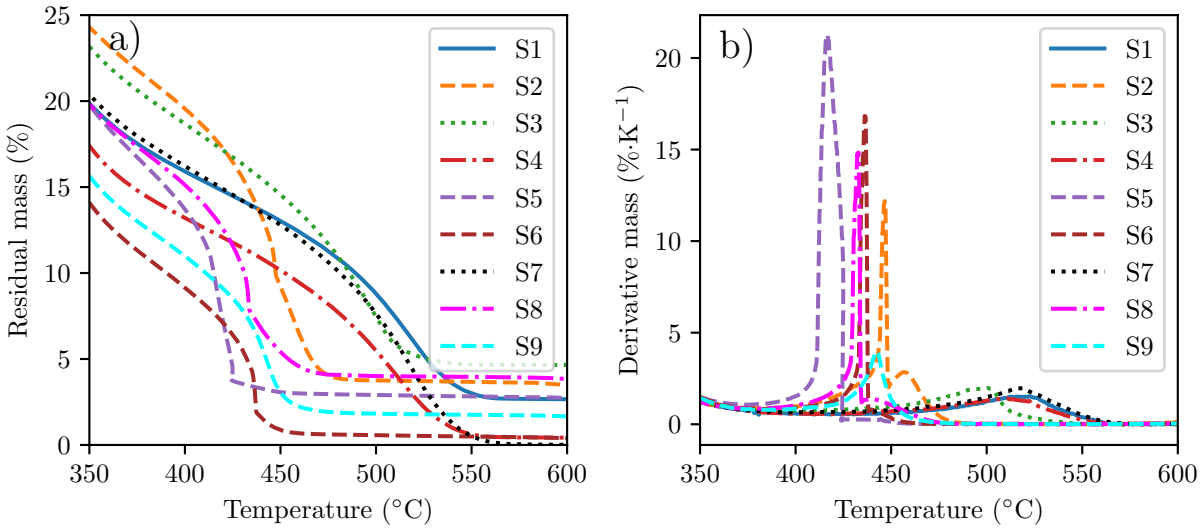

Figure 28: Final decomposition and residual mass of TPD composites showing the TGA denoted by a) and DTG thermograms denoted by b).

The Differential Thermal Analysis (DTA) plots did not provide any additional information to the compositional analysis and thermal events.

4.2.3 Morphology

Diffractogram reflection assignment

Table 6 summarizes the assignments given to the identified reflections in Figure 29. Each assignment is based on literature summarized in Table 1 and the reflections created by the neat additives.

The diffractogram of the native dextrin, identified as α-Amylose $(C_6H_8O_4)_n$ (ICDD PDF 00-043-1858), features strong reflection peaks at 15.1° (d = 0.586 nm), a doublet at 17.2° (d = 0.516 nm)/17.9° (d = 0.493 nm) and another strong reflection at 23.0° (d = 0.387 nm) typical for a type-A crystallinity (Van Soest, Hulleman, *et al.* 1996). In raw starch this type of crystallinity is attributed to chains arranged in a double helical structure (Van Soest, Hulleman, *et al.* 1996; H Liu, Xie, *et al.* 2009). Just as for conventional thermoplastic starches, the diffraction pattern of the dextrin based TPD featured an extensive amorphous scanning halo with weaker diffraction peaks. This is typical for semi-crystalline polymers with a low crystallinity (Frost *et al.* 2009).

Table 6: Crystallographic parameters associated with most prominent reflections in the TPD composite diffractograms.

#	2Θ (°)	d (nm)	Assignment
A	6.7	1.31 ± 0.02	SA
	11.1	0.79 ± 0.02	SA
B	11.7	0.76 ± 0.00	LDH
C	15.1	0.58 ± 0.01	Starch
	15.6	0.57 ± 0.01	SA
	15.7	0.56 ± 0.02	CNF
D	17.2	0.52 ± 0.01	Starch
E	17.9	0.49 ± 0.01	Starch
F	18.4	0.481 ± 0.003	LDH
G	20.1	0.442 ± 0.005	Starch
H	21.5	0.414 ± 0.006	SA
	21.6	0.412 ± 0.008	ALC
I	22.9	0.39 ± 0.01	CNF
	23.0	0.387 ± 0.003	Starch
J	23.5	0.378 ± 0.010	LDH
	23.6	0.377 ± 0.004	SA
k	29.4	0.302 ± 0.003	LDH

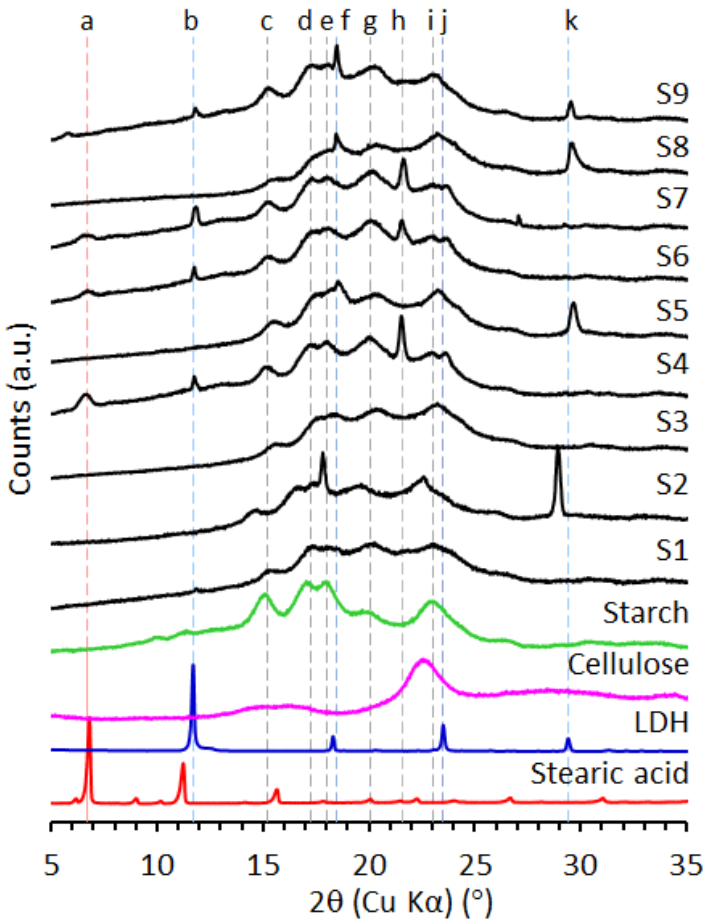

Figure 29: Aged TPD nanocomposite diffractograms compared to neat components.

.

Usually the TPD gelatinisation process destroys the original crystalline structure and induces a different, processing-induced crystallinity. Depending on variables such as the type and amount of plasticizer and the intensity of the applied shear, three types of induced crystalline structures, i.e. V_H-type, V_A-type and E_H-type, are obtained (Van Soest, Hulleman, *et al.* 1996; H Liu, Xie, *et al.* 2009). The V-type crystallinity arises from the packing of single helix chains, mostly amylose, with ligands such as stearic acid. These are known as amylose lipid complexes. The latter occur in anhydrous (V_A) or hydrated forms (V_H) with interhelical water molecules present in the latter (Obiro, Sinha Ray & Emmambux, 2012). The present dextrin-based TPD samples featured a combination type V_A-type crystallinity superimposed on the original A-type polymorphism. This means that the neat TPD, as well as most of the nanocomposites, either recovered or retained the type-A crystallinity present in the native dextrin. This behavior can be attributed to the fact that the dextrin starch base comprises primarily rather short chains as this favours type-A crystallinity (Castaño *et al.* 2014). In addition, the associated much lower melt viscosity may facilitate rapid reorganisation after melting in the compounding process. The results suggest that there were essentially linear dextrin chains that can

form V-type complexes with ligands as well as self-association to form double helical type-A structures.

The strong reflection at 22.9° (d = 0.386 nm) in the diffractogram for the nanocellulose fibres, identified as Cellulose Iβ (ICDD PDF 00-056-1718), is typical of the Cellulose I pattern (Nindiyasari *et al.* 2016).

Morphological analysis of TPD composites

The ageing diffractograms are shown in Figure 30. There is also an indication of this reflection in the XRD pattern of the TPD cellulose nanocomposite (Sample S3) but not in any of the other composites that contain CNF.

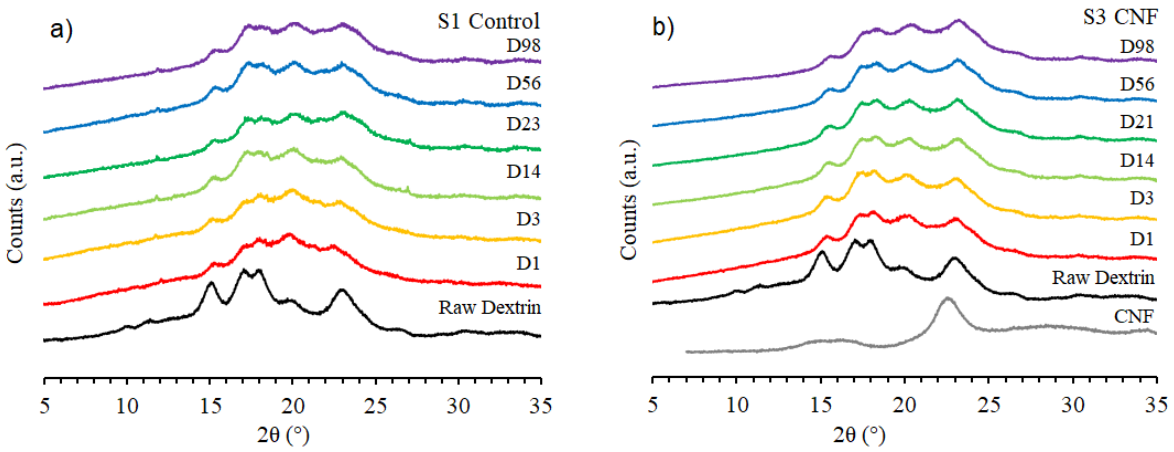

Figure 30: Diffractograms of a) the control composite (S1) and b) the TPD composite containing cellulose nanofibres (S3).

.

Figure 31 and Figure 32 show the micro-imaging of Sample 1 and Sample 3 respectively. Both micrograph sets show the presence of glass beads. Figure 31 shows a wide variety of water crystals, shown on the enlarged glass bead image and another larger water crystal in the top right corner.

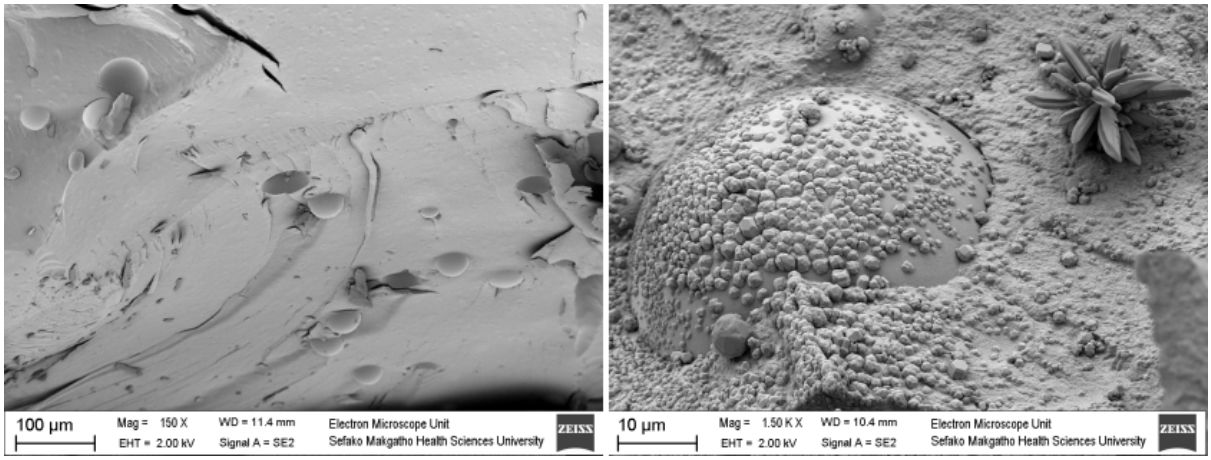

Figure 31: Micrographs of control sample (S1 containing glass beads).

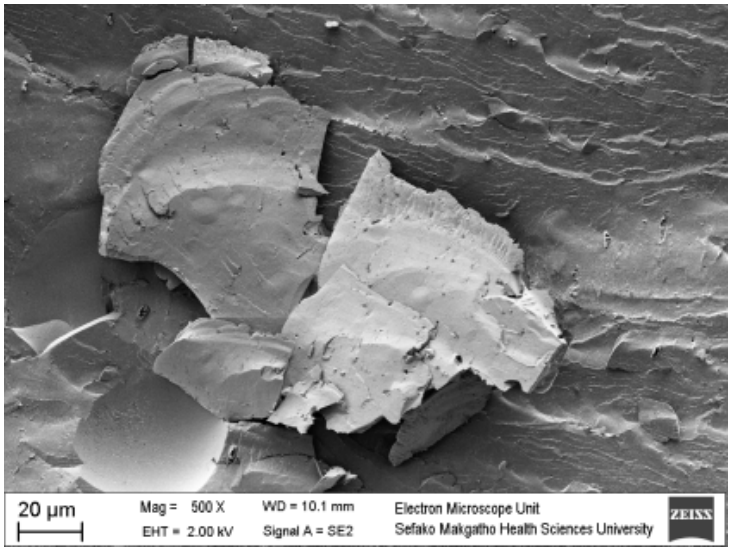

Figure 32: Micrographs of cellulose TPD composite (S3 containing CNF).

The diffractogram for the LDH, identified as calcium aluminium hydroxide carbonate hydrate (ICDD PDF 01-087-0493), features prominent reflections at 11.7° (d = 0.755 nm), 18.3° (d= 0.48 nm), 23.5° (d = 0.38 nm) and 29.54° (d = 0.30 nm). The diffractogram for the LDH-based dextrin TPD nanocomposite (Sample S2) shown in Figure 29, shows only two of these reflections as very strong and sharp peaks albeit at slightly higher d-spacing values (0.50 and 0.31 nm respectively). Figure 33 shows the time evolution of the XRD pattern for this nanocomposite.

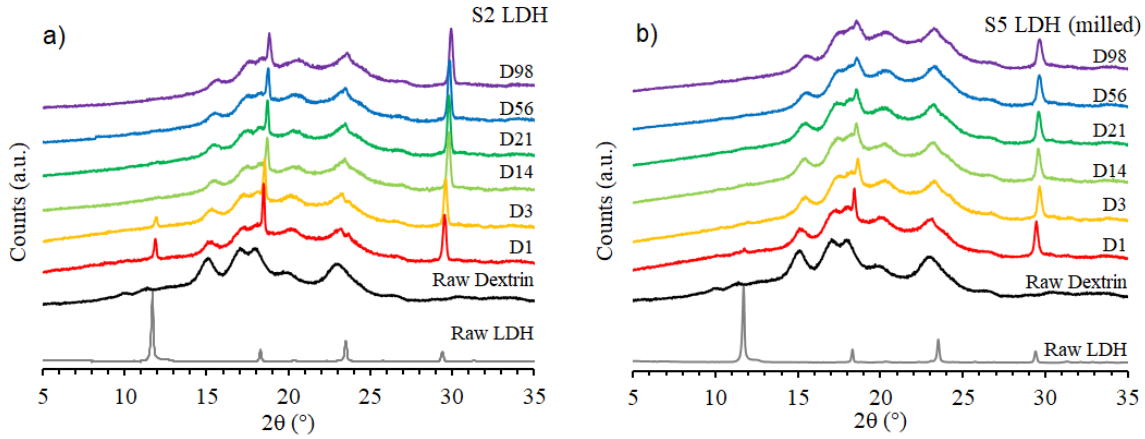

Figure 33: Diffractograms of TPD composites containing LDH (a) S2 & b) S5).

.

The following micrographs shown in Figure 34 and Figure 35 for the 4 wt.% LDH TPD nanocomposites. There appears to be no striking resemblance between the images when comparing across samples. In Figure 35 it is possible to see the distinctive hexagonal shapes of the hydrocalumite crystals. This is not clearly visible for the unmilled sample in Figure 34.

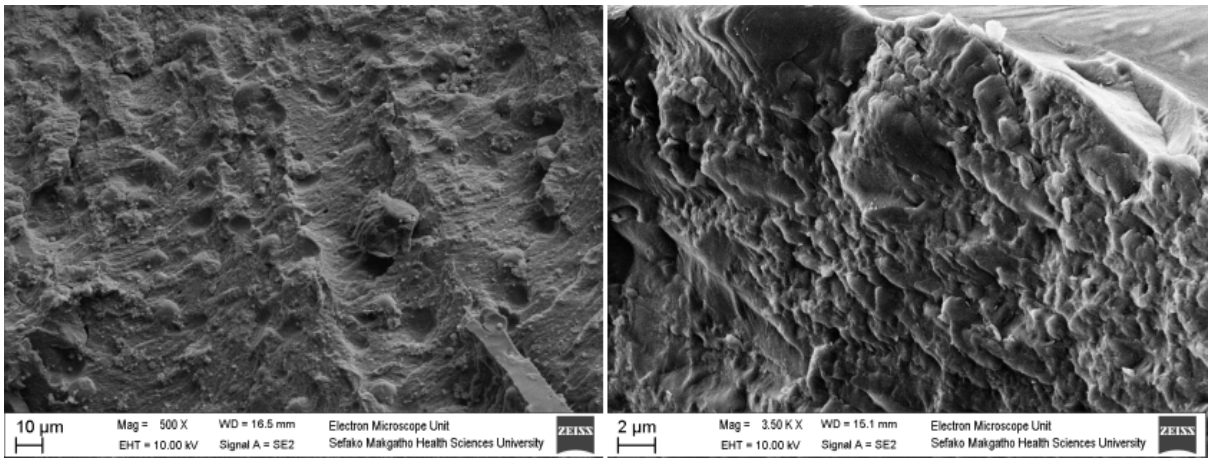

Figure 34: Unmilled LDH TPD sample micrographs (S2 containing LDH).

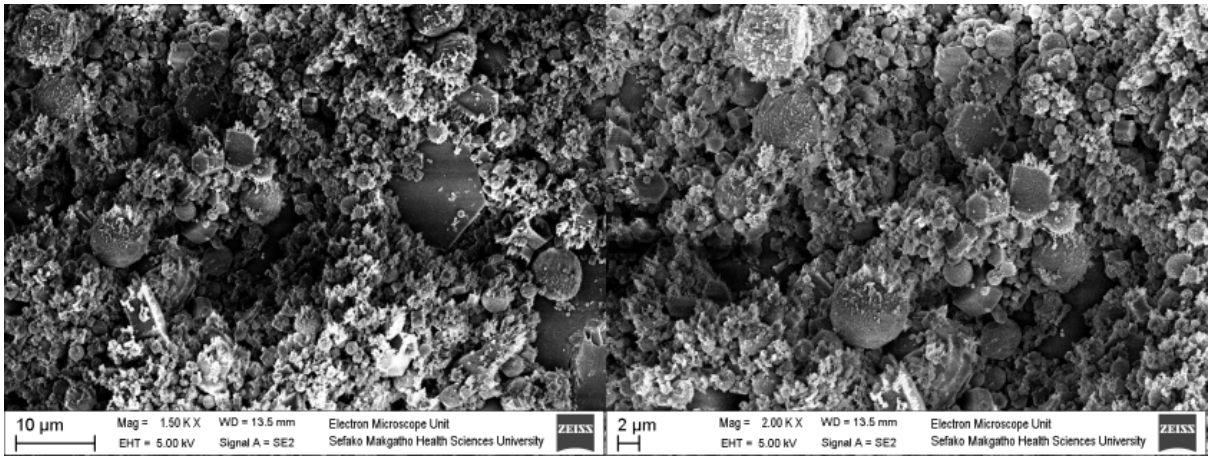

Figure 35: Milled LDH TPD sample micrographs (S5 containing LDH).

The main LDH reflection is clearly visible on Day 1 and at diminished intensity on Day 3. However, it is absent in the diffractograms recorded on later days. Similar observations apply to the TPD nanocomposites obtained with either the milled LDH (Sample S5) or LDH+CNF combination (Sample S8). However, the main LDH reflection at 11.7° (d = 0.77 nm) is retained indefinitely in the nanocomposites based on the stearic acid plus LDH combination (Sample S6) as well as in the ternary additive mixture (Sample S9). The implication is that, in the absence of stearic acid, either the LDH in the nanocomposites delaminates on ageing or it is degraded into compounds that do not feature the reflections associated with the hydrocalumite.

In the presence of both stearic acid the LDH main reflection seems to remain unchanged during ageing as can be seen in Figure 36. This may imply that the LDH recrystallises with intercalated stearic acid (proposed by Figure 37) or an effect caused by the production of stable ALC's.

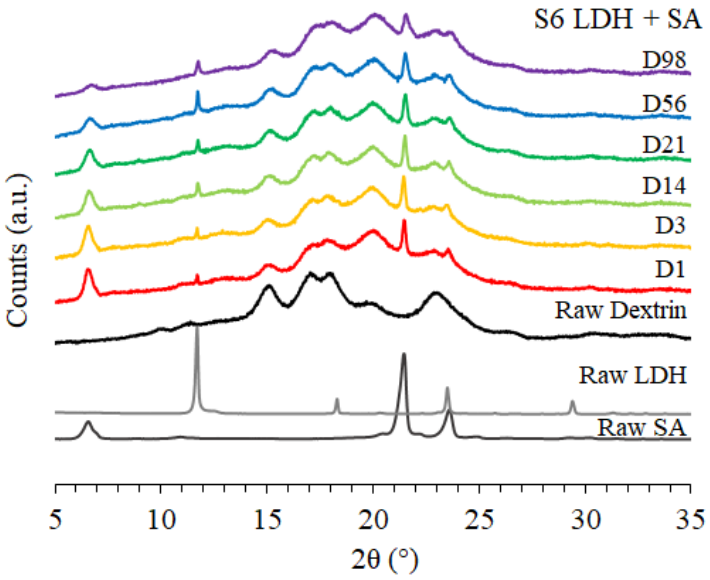

Figure 36: Diffractograms of TPD composites containing stearic acid and unmilled LDH (S6).

Figure 37 is a set of micrographs of sample S6 which contains hydrocalumite and the fatty acid. On the higher resolution micrograph, an unmistakable hexagonal hydrocalumite crystal is shown. Layered double hydroxides are known to spontaneously become intercalated with stearic acids upon recrystallisation (Dong *et al.* 2019).

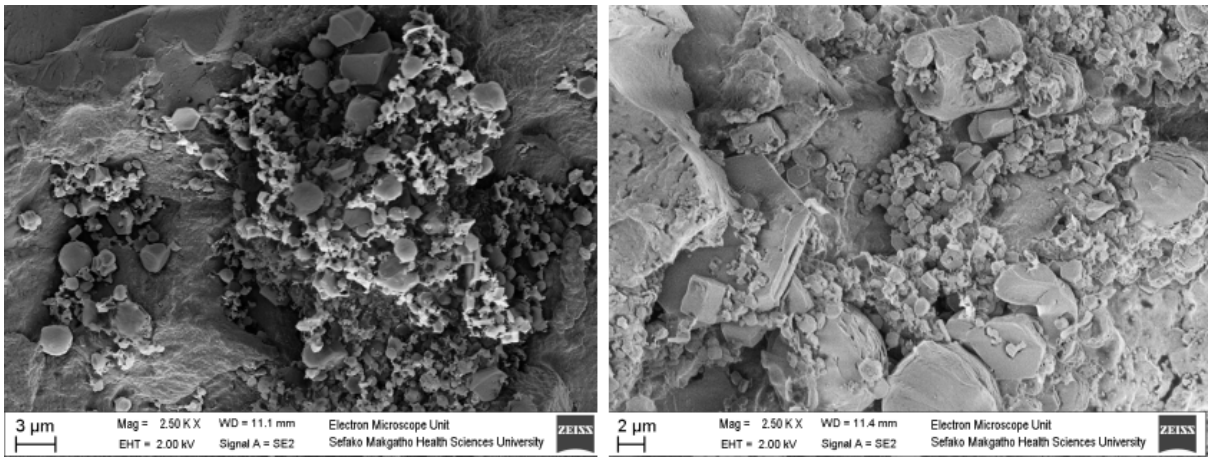

Figure 37: Micrographs of sample 6 (which contains LDH/SA 1:1).

Crystal analysis during ageing

Relative crystallinity was calculated and tabulated in Table 7 using methods as discussed in X-ray diffraction (XRD) in the Characterisation methods subsection. The large variation in approximate relative crystallinity values over samples are due to the crystallinity

added by the additive type. The nanoclay, nanocellulose and stearic acid are far more crystalline than the native dextrin.

Table 7: Approximate relative crystallinity of TPD samples during ageing.

Sample	Relative crystallinity [%]					
	Day 1	Day 3	Day 14	Day 23	Day 56	Day 98
S1	1.13	1.18	1.58	1.49	1.57	1.50
S2	4.74	4.97	4.70	4.86	5.19	5.21
S3	3.31	3.59	3.68	3.64	3.82	3.64
S4	4.33	4.27	4.37	4.45	4.29	4.43
S5	4.84	5.12	5.12	5.37	5.35	5.42
S6	3.70	3.72	4.13	4.06	4.12	4.93
S7	4.15	4.35	4.51	4.26	4.40	4.48
S8	4.49	4.87	4.58	4.57	5.13	4.90
S9	4.08	4.33	4.76	4.49	4.79	4.56

In order to compare retrogradation effects across samples, the relative crystallinity was normalised according to its initial (Day 1) relative crystallinity and to produce Figure 39 and Figure 43. Table 7 indicates that all compounds were predominantly amorphous in nature with very low degrees of crystallinity. The addition of additives has clearly made an impact on the morphology of the TPD. It could therefore well be that the difference in the crystallinity values of the samples simply reflects the contribution of the crystalline additives that they contain. To test this hypothesis, an attempt was made to predict the crystallinity based on a linear blending rule:

$$X = X_{TPS} + U_{CNF}w_{CNF} + U_{SA}w_{SA} + U_{LCD}w_{LDH} \tag{26}$$

where X is the steady state crystallinity (in %) of the nanocomposite after ageing. This was taken as the average value for measurements made at times exceeding 21 days of ageing. $X_{TPS} = 1.54$ % is the crystallinity of the neat TPD; w_i is the mass fraction (in wt. %) and U_i is an adjustable constant quantifying the contribution of additive i. A least squares fit yielded $U_{CNF} = 1.20$; $U_{SA} = 0.63$, and $U_{LDH} = 0.84$.

Figure 38 shows a plot of the predicted crystallinity values versus the steady state crystallinity. This suggests that the model fits the data reasonably well except for the cellulose nanofibre composite (Sample S3). Also shown in Figure 38 is a plot of the crystallinity on Day 1 against the steady state value. These values fall on a line with a slope of unity.

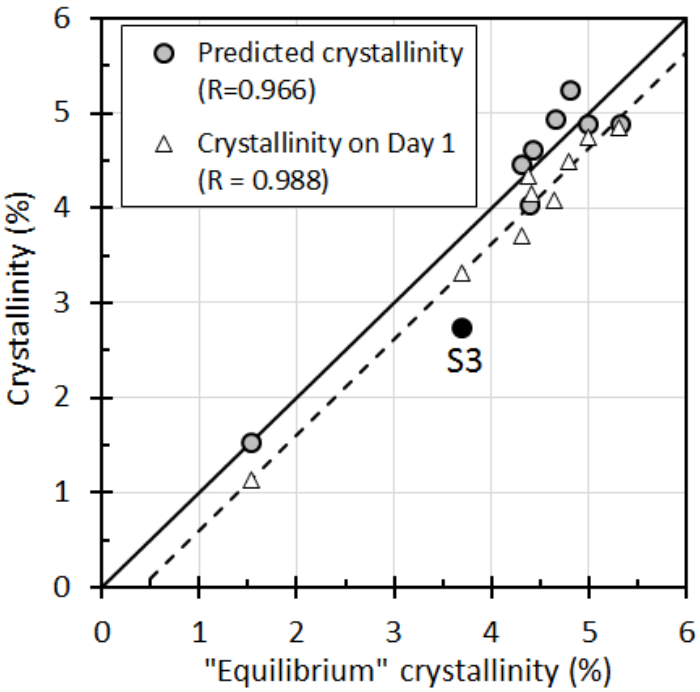

Figure 38: Correlations between the initial and steady state crystallinity and predicted values.

.

If the additive is perfectly crystalline, a value of unity for the corresponding Ci implies direct additivity and the absence of an interaction with the dextrin matrix. The value C_{CNF} exceeds unity and this indicates that the presence of the cellulose nanofibre leads to a slightly larger crystallinity than expected. This could imply that the CNF acts as a weak nucleating agent for the dextrin but in order to prove this, further experimentation is required.

The opposite is true for the stearic acid and the LDH. In the case of stearic acid, the formation of the ALC may explain the lower than expected crystallinity. When this complex forms, the stearic acid molecules enter the single chain starch helices, stabilizing that particular form. However, it means that the molecules available for crystallising as a separate stearic acid phase is reduced. The lower than expected crystallinity for the unmilled LDH compound (Sample S2) is consistent with the notion that it exfoliated on incorporation into the TPD which will be further discussed in this section.

The control sample (S1) continued to rapidly increase in crystallinity until Day 21 in storage. The sample containing only stearic acid as additive (S4) did not have a noticeable increase in crystallinity. It should however be noted that the intensity of various reflections did change substantially for all samples during ageing. This means that the crystallinity produced by for example LDH may have decreased while for example the A-type starch peak may have increased by a similar amount which still implies that

retrogradation has occurred but hasn't changed the overall crystallinity of the sample.

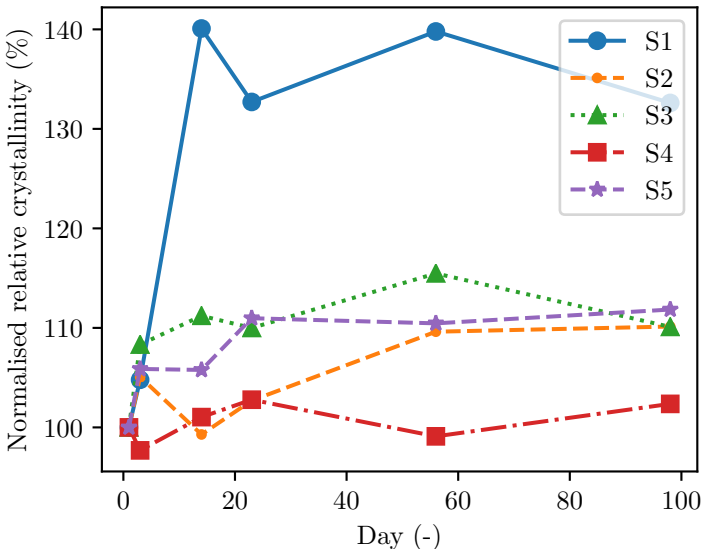

Figure 39: Normalised relative crystallinity of TPD composites during ageing containing a single additive.

.

A clear standout shown by Figure 39 is that of S4. This sample shows a retardation of the retrogradation of the starch sample. This may be due to the creation of more stable amylose-lipid complexes (S Wang, C Li, *et al.* 2015). The diffractograms do however indicate the decrease of stearic acid crystallinity over time, shown in Figure 40. This indicates exfoliation into the matrix of the TPD or the continuous formation of ALC's during ageing as Figure 41 displays.

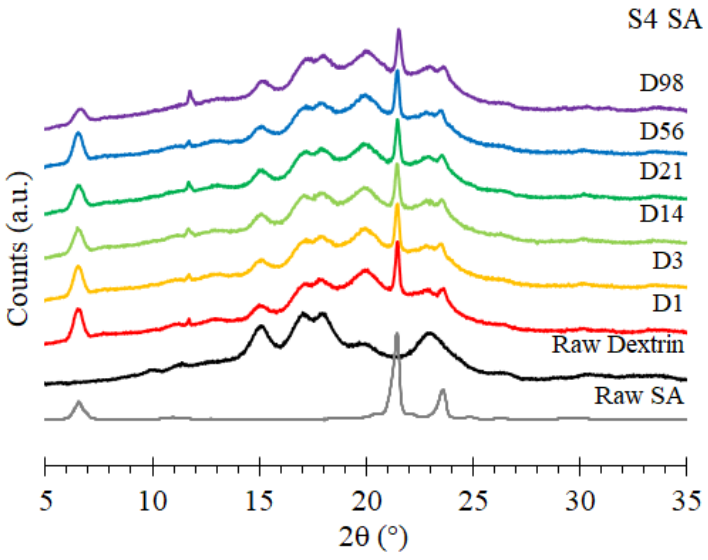

Figure 40: Diffractograms of TPD composites containing stearic acid (S4).

.

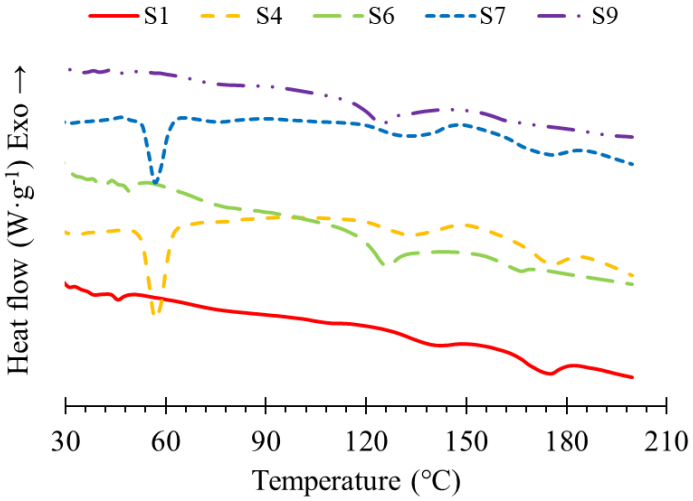

Figure 41: HPDSC thermograms of TPD composites containing stearic acid.

.

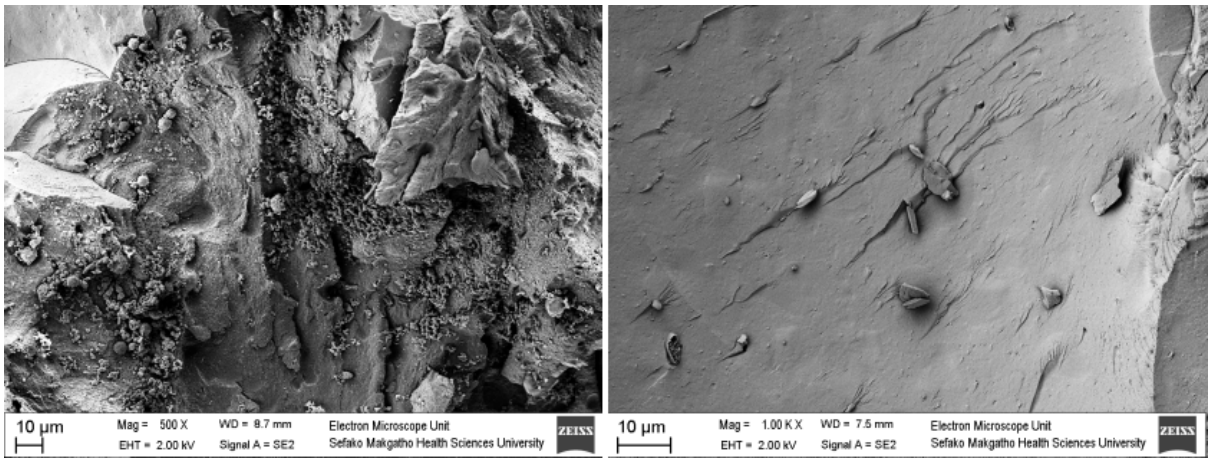

Figure 42: TPD and stearic acid composite micrographs (S4 containing SA as additive).

Thermoplastic composites containing multiple additives also indicated slower retrogradation, but to a clear lesser extent to that of S4. S7 does however seem to be the best out of the samples shown in Figure 43. This corresponds well to the ALC explanation and to the data displayed in Figure 41 where it displays similar melting points to that of S4.

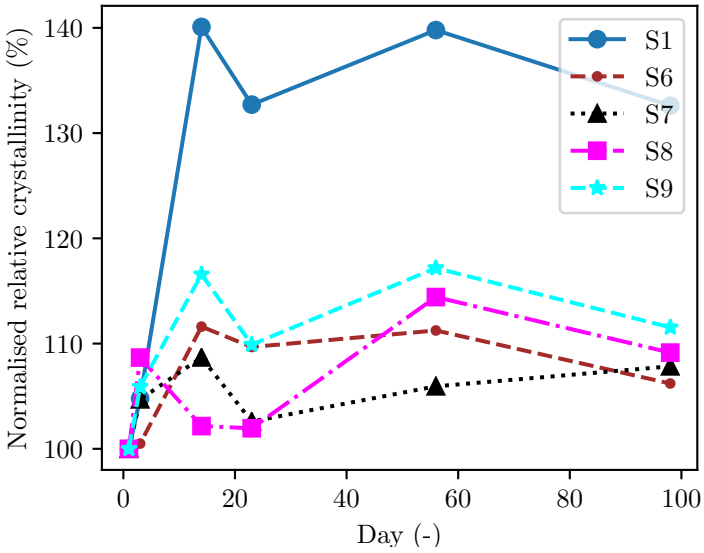

Figure 43: Normalised relative crystallinity of TPD composites during ageing containing multiple additives.

.

The results of the dissolution tests and the compounding experience will serve to choose S7 as the system to compound with amitraz. Figure 43 and Figure 41 hint toward the formation of stable ALC's and thus slower retrogradation for S7. It is however prominent to see changes in the intensities of various reflections in Figure 44. A micrograph set of this sample is shown in Figure 45.

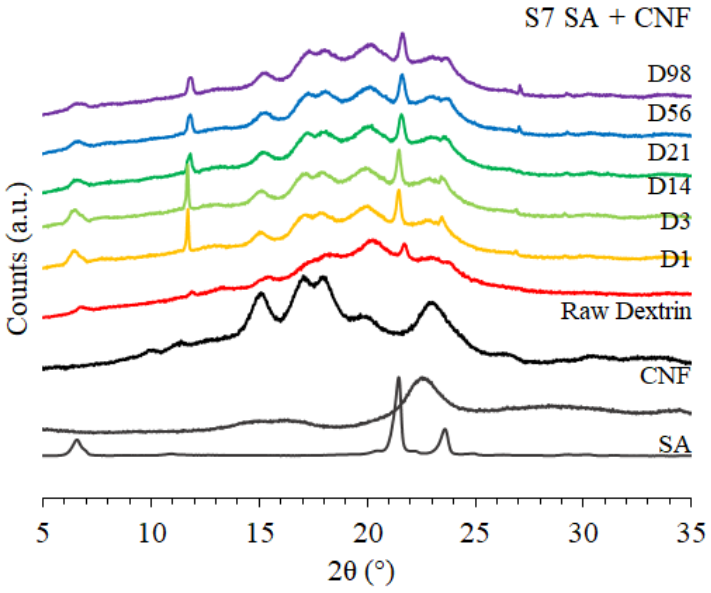

Figure 44: Diffractograms of TPD composites containing stearic acid and cellulose nanofibres (S7).

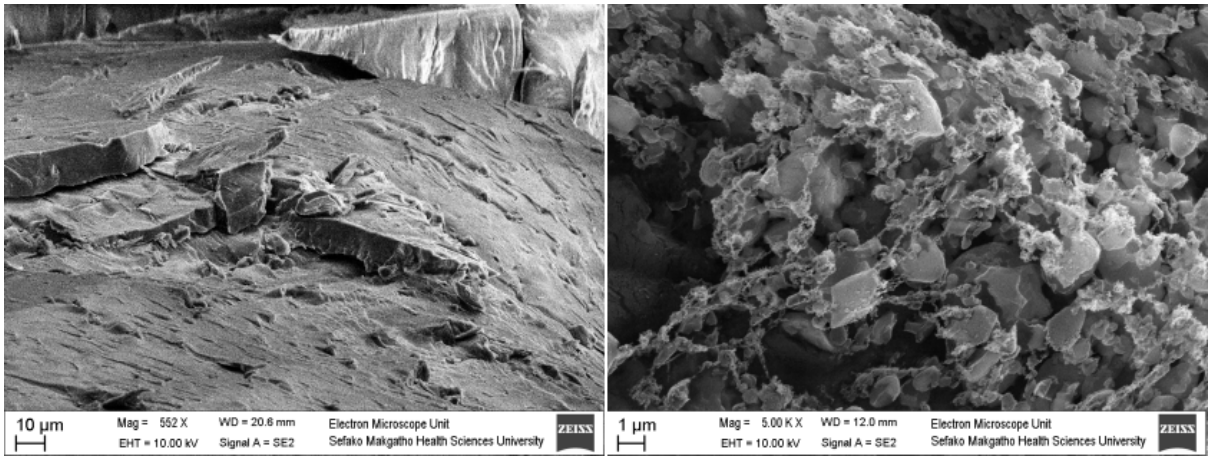

Figure 45: TPD images containing fatty acids and cellulose nanofibres as additives (S7 SA/CNF 3:1).

It can be argued that S8 on Figure 46 displays similar exfoliation mechanics as that displayed in Figure 33. Day 1's diffractogram displays a slight reflection at 12°, which disappears as the sample ages. S9 exhibits the same results shown in Figure 46 as seen in Figure 36. The same conclusions may be drawn.

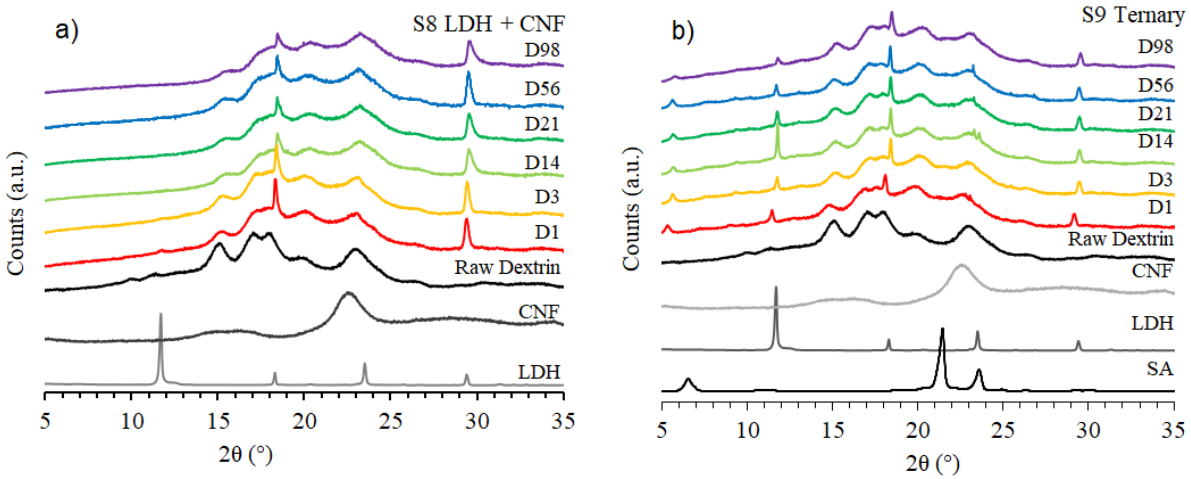

Figure 46: Diffractograms of TPD composites containing a) LDH and CNF (S8) and b) the ternary additive TPD composite (S9).

Sample S8 and Sample S9 were also imaged under SEM and are shown in Figure 47 and Figure 48. No clear conclusions are made from this analysis.

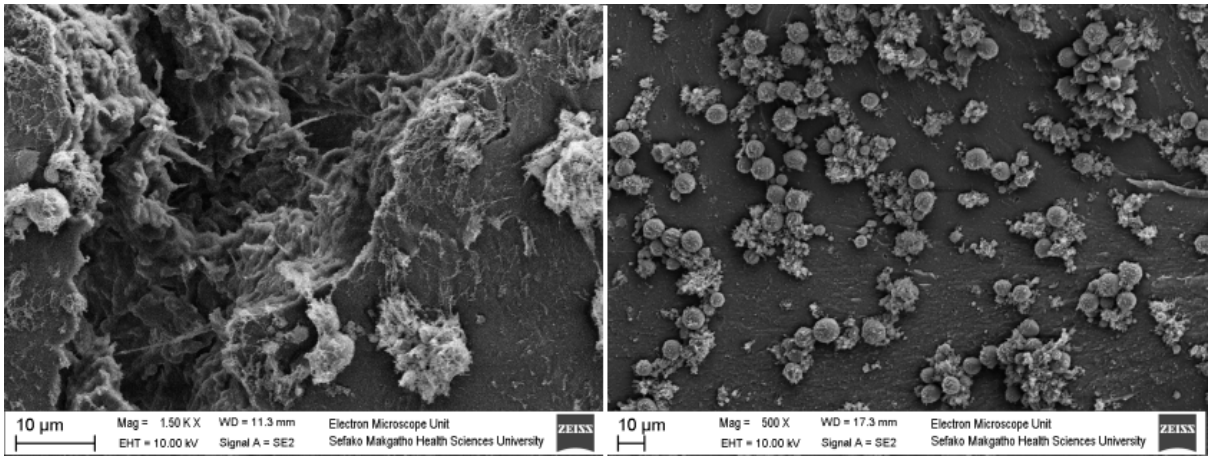

Figure 47: SEM images of sample 8, containing LDH and CNF (LDH/CNF 3:1).

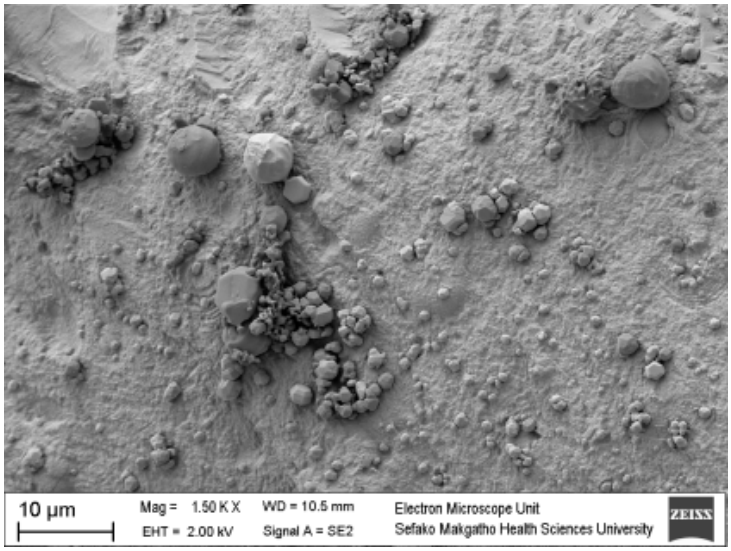

Figure 48: Micrographs of the ternary additive composite (S9 containing LDH:SA:CNF at 1.5:1.5:1).

4.2.4 Mechanical properties

Mechanical properties were investigated via Dynamic Mechanical Analysis (DMA). These experiments were conducted at least 30 days after extrusion. At this point, the retrogradative effects were believed to have stabilised. Figure 39 and Figure 43 show that the morphology of the composites remained relatively unchanged after this period. A representative DMA plot is shown in Figure 49.

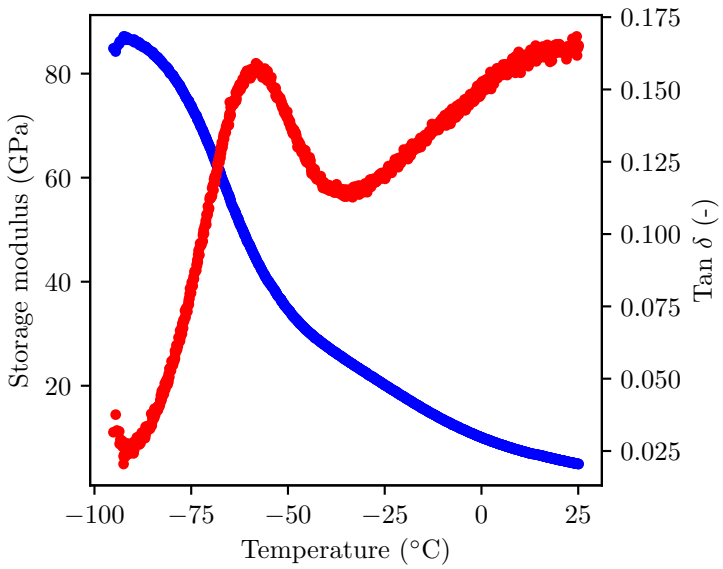

Figure 49: Typical TPD DMA results as portrayed by S2.

.

In order to compare glass and β-transition temperatures (tan δ peaks), a peak model was fitted to the data around the occurrence. This model is based on a linearly increasing sinusoidal peak. The model's fit can be visualised by Figure 50. The model equations are only fitted to be viable within 10 °C of the glass transition temperature.

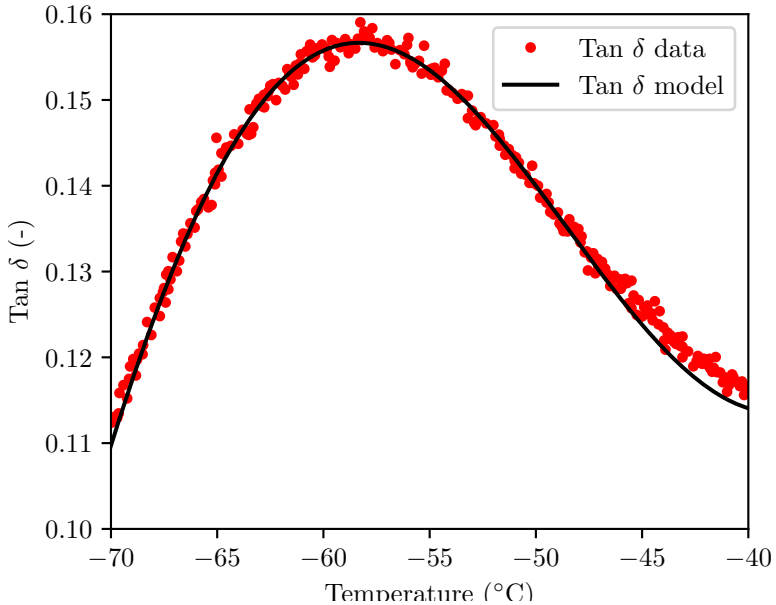

Figure 50: Tan δ peak fitting example, exemplified by S2 which contains LDH.

.

The results of the duplicated DMA analyses is summarised as averages in Table 8. All

samples display the moisture content value, which seem similar to what was expected if compared to the batch compositions in Table 3.

Table 8: Mechanical, phase change and moisture properties of various TPD composites.

Sample	Moisture (wt.%)	T_β (°C)	T_G (°C)	E′ at 20 °C (GPa)
S1	16.9 ± 0.5	-58	14	1
S2	16.3 ± 0.0	-56	23	2.5
S3	15.0 ± 0.2	-57	21	3.2
S4	16.7 ± 0.4	-59	13	1.2
S5	18.1 ± 0.0	-55	32	3.4
S6	18.6 ± 0.4	-56	19	1.9
S7	17.8 ± 0.8	-58	21	3.2
S8	17.8 ± 0.1	-59	23	3
S9	18.4 ± 0.2	-56	6	2.4

All the compounds exhibited a pronounced β-transition at a similar temperature of around -57 ± 2 °C. However, the glass transition temperatures differed significantly and the modulus curves were displaced vertically compared to this material. Another commonality was the development of severe scatter in the tan δ data as the temperature approached 20 °C and beyond. An example of this occurrence is shown on the typical plot in Figure 49. Table 8 also lists values of the bending modulus at 20 °C as determined by DMA. The results indicate that the CNF (S3, S7, S8 and S9) and LDH nanoparticles (S2, S5, S6, S8, S9) led to a significant increase in the bending modulus. Compounds containing them were up to three times stiffer than the glass-filled base compound.

Comparing Sample S5 to Sample S2 shows that the milled LDH was more effective than the unmilled material as a reinforcing filler. The CNF appears to be particularly effective considering that loadings of just 1 wt.% provided stiffness increases exceeding a factor of three cf. Samples S3 and S7. The result for Sample S4 shows that the stearic acid on its own did not impart a reinforcement effect.

4.2.5 Dissolution

As stated in the Dissolution kinetics of solid dosage forms subsection, the dissolution speed of solid dosage forms is a measure of how quickly an active ingredient is released. Thus the dissolution rate of a candidate matrix must be used to evaluate the suitability

of the compound as a solid dosage form. The intended purpose of the compound is to be placed in a water medium, where the matrix would dissolve leaving an insoluble active ingredient over time. The Thermoplastic starch dissolution experiments discussion explains the methods involved in the characterisation of the dextrin composite's dissolution rate in water. The spectroscopic method here requires the calibration of the indicator to the dissolved concentration of the analysed compound at the analysis wavelength.

The calibration curve shown in Figure 51 displays the linear relationship as defined by the Beer-Lambert law. At concentrations higher than 1.25 g·L^{-1}, a significant deviation would occur at the specified wavelength of 580 nm. Thus all dissolution experiments were set up such that the total amount of dextrin starch placed in the 1 L volumetric flask would be 0.60 g.

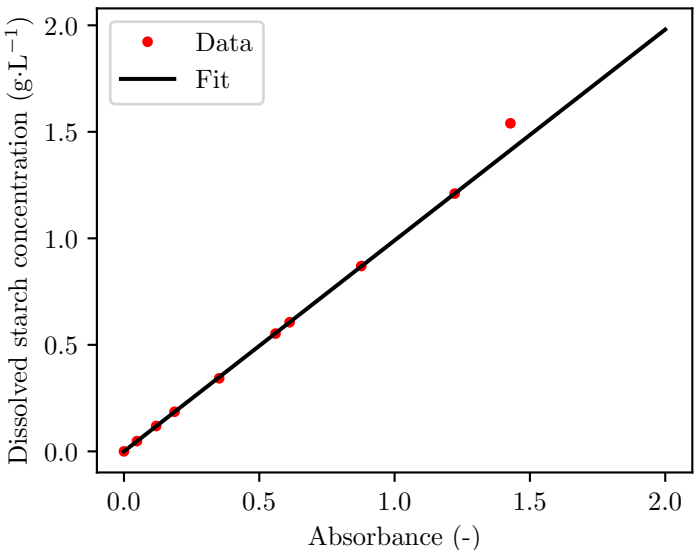

Figure 51: Starch dissolution calibration curve.

The typical dissolution experiment results are scatter plotted in Figure 52 where the fitted model is also displayed. All experiments showed the characteristic fast initial dissolution rate, followed by a continuous decease in the speed of dissolution. Most experiments gave similar repeatability as shown by the closeness of the coloured data points of the experiments. The variability of the experiment is indicated by Figure 53 as a standard deviation error bar of the various fitted rate constants of each individual experiment data set.

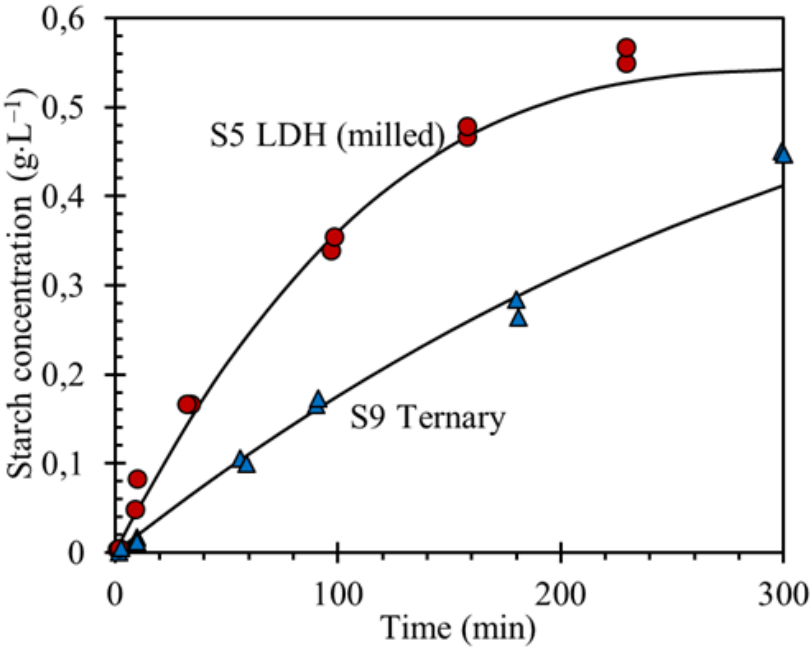

Figure 52: Typical dissolution plots.

The fitted rate constants are also shown in Figure 53. The variability shown as error bars are calculated as the standard deviation of the fitted rate constant for each experimental data set.

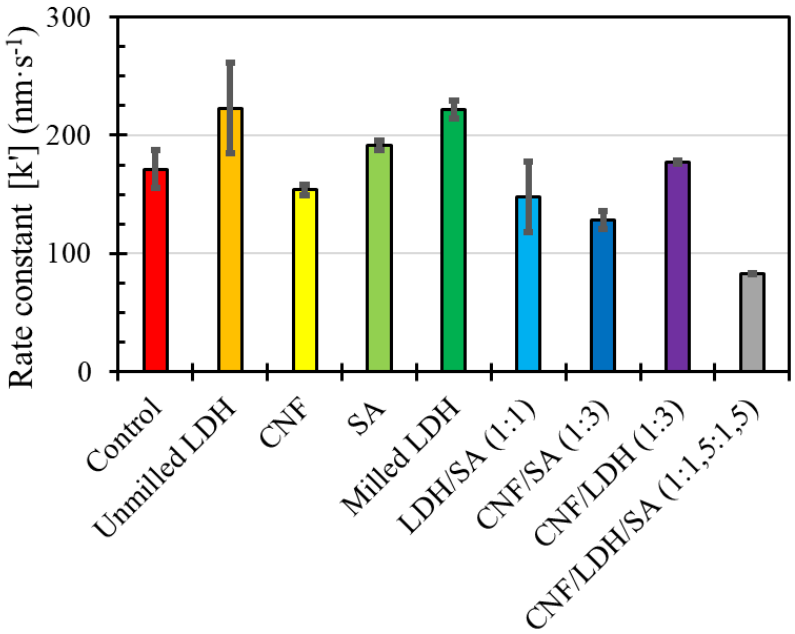

Figure 53: Summary of dissolution rate constants of various TPD composites in water.

There is a clear similarity in dissolution behaviour of the samples containing unmilled LDH (S2) and milled LDH (S5). The fitted rate constants are nearly identical, and

are both higher than that of the control compound (S1). The SA compound (S4) also dissolves faster than S1, but performs far slower when combined with other compounds. When LDH and SA are combined the effect goes in the opposite direction as S6 has a lower rate constant, indicating a synergistic effect between LDH and SA on the thermoplastic starch.

However, when LDH as an additive is combined with CNF and SA (S9), the dissolution rate drops substantially. This is unexpected as the CNF and SA combination (S7) does not perform as slowly as S9, but does lower the dissolution rate more than the SA compound (S4) and the CNF compound (S3), which all also have lower rate constants than the control compound (S1). This may indicate an effect of the glass beads, as both the control compound and S3 contain glass beads. If S3 contained 4 wt.% CNF, the results may have been more spectacular. When CNF is combined with LDH, the dissolution rate is very similar to the control compound.

After modelling the results of the dissolution experiments, the models of each sample were plotted in Figure 54 and Figure 55. These graphs are based on an ideal experiment where 1 g of the TPD of each kind is placed in a 1 L solution of water. To accommodate for spacing, the single additive TPD composites are plotted in Figure 54

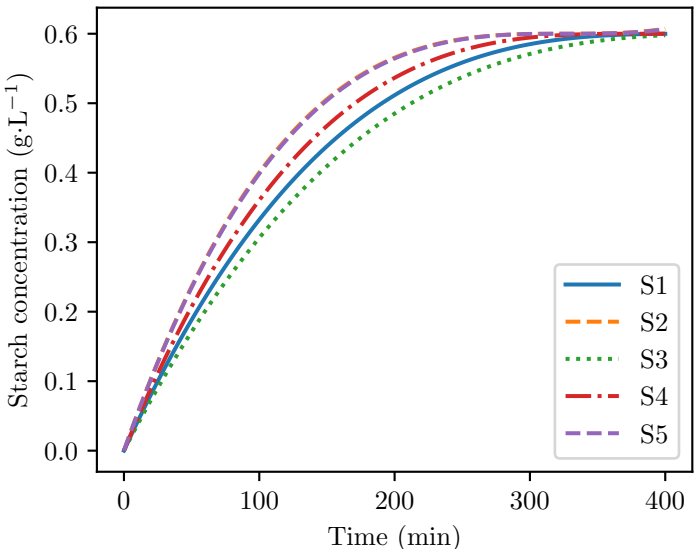

Figure 54: Dissolution plots comparing TPD composites containing single additives.

and the TPD composites containing multiple additives are shown in Figure 55.

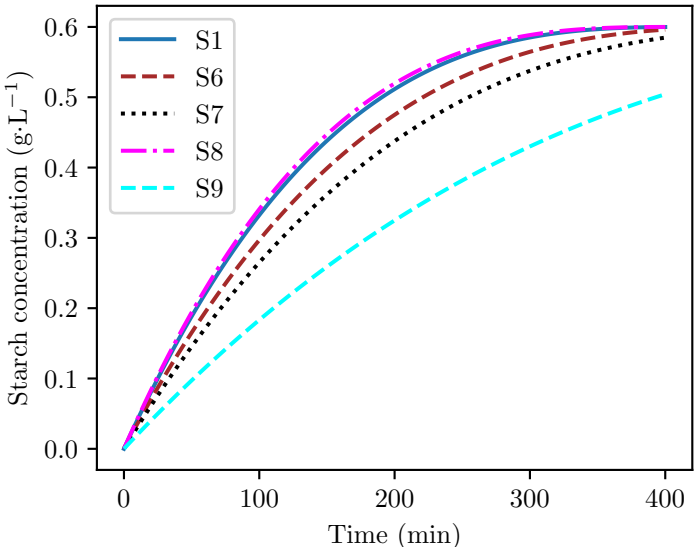

Figure 55: Dissolution plots comparing TPD composites containing multiple additives.

By investigation of Figure 54 and Figure 54, the model predicts that systems with multiple additives will dissolve over a longer period of time. This indicates a possible synergistic behaviours of the additives w.r.t. slowing the dissolution rate. When comparing S6, S8, and S9, an interesting behaviour between the three selected additives occur. The CNF and LDH combination (S8), seems to dissolve faster than the control compound, but slower than the single additive LDH systems (S2 and S5). This is more clearly illustrated in the fitted constants indicated in Figure 53. This multiple additive system however, dissolves faster than the CNF single additive compound (S4). This does not imply synergy, but rather a combination of the observed dissolution properties.

When compounding with both LDH and SA, the dissolution rate of the multiple additive system (S6), is slower than that of both single additive systems (S2-umLDH, S5-mLDH and S4). This implies a synergistic effect as the property of the composite, behaves better than that of both its constituents. The SA and CNF system (S7), also displays similar synergy. When compounding all three additives in the TPD matrix (S9), this proposed synergistic effect is amplified even more. The Particle Size Distributions (PSD) of the relevant composites are discussed in the amitraz Compound Dissolution section.

4.3 Deep eutectic solvents as matrices for solid dosage forms

Two different salt system were investigated as candidates for the fast dissolving solid dosage form. The sytems discussed in this section are:

- urea & 1, 3-dimethylurea eutectic (UDE)
- urea & acetamide eutectic (UAE)

Both systems have been shown to form deep eutectic solvents as discussed in the Deep eutectic salts background subsection. The phase diagram was created by making cooling curves at various concentrations. The eutectic composition and temperature was then used to create casts that can be formed at low temperatures.

4.3.1 Eutectic phase behaviour

Cooling curves

Cooling curves were constructed using methods described in the Salt freezing curves explanation. The typical cooling curve is shown in Figure 56. This specific curve was constructed by the analysis of the UDE system at 70 wt.% urea. There is a clear subcooling of the melt occurring prior to phase change for all compositions of all systems. This phase change is exothermic to such an extent that the temperature of the two phase mixture increases. The peak of this increase was taken as the actual freezing point of the composition.

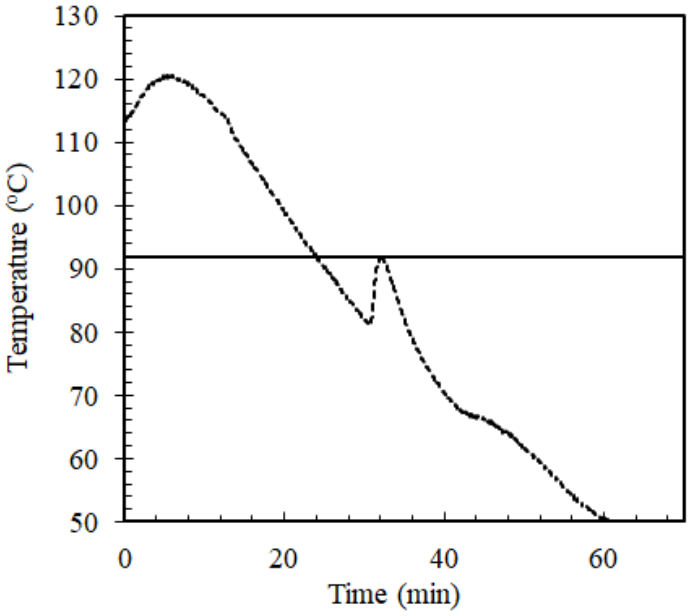

Figure 56: Typical freezing curve indicating the subcooling prior to phase change.

Phase behaviour modelling

After duplicate experiments of the cooling curves, the phase diagram could be created. The eutectic phase model which assumes no interaction is shown in Equation 1. More complex models that model the Gibbs Free Energy of the system are discussed here. The simplest thermodynamic model for a binary system, the Porter interaction model, is shown in Equation 27.

$$ln(\gamma_i) = A_P x_i x_j \tag{27}$$

where A_P is known as the Porter interaction coefficient. Larger values of this coefficient indicates higher levels of interaction between different molecules. A second interaction model, the Margules thermodynamic model for binary systems, is shown in Equation 28

$$ln(\gamma_i) = [A_{i,j} + 2(A_{j,i} - A_{i,j})x_i]x_j^2 \tag{28}$$

where A depicts the Margules interaction coefficient for one component w.r.t. the other. This model is more complex than the Porter model as it predicts different levels of interaction caused by different molecules. The Wilson model is depicted in Equation 29

$$ln(\gamma_i) = -ln(x_i + \Lambda_{i,j}x_j) + x_j\left(\frac{\Lambda_{i,j}}{x_i + \Lambda_{i,j}x_j} - \frac{\Lambda_{j,i}}{x_j + \Lambda_{j,i}x_i}\right) \quad (29)$$

where Λ is similar to A. Values closer to unity indicate less interaction. Standard enthalpies and melting points were obtained from literature and summarised in Table 9.

Table 9: Standard enthalpies and temperatures of fusion of various organic salts.

Compound name	ΔH°_{fus} [J·mol^{-1}]	T°_{fus} [K]	Reference
Urea	14 600	407.2	U Rai & R Rai (1998)
1,3-dimethylurea	13 620	379.5	Della Gatta & Ferro (1987)
Acetamide	15 600	353.0	Domalski & Hearing (1996)

Urea and 1,3-dimethylurea eutectic modelling

Each model is plotted on its own set of axes to avoid confusion. All interaction coefficients were regressed to values shown in Table 10. The ideal eutectic phase model, Equation 1, is plotted along the averaged duplicate data points in Figure 57. This model predicts a eutectic temperature of 60 °C at a composition of 41 wt.% urea (50 mol.%). Suriyanarayanan *et al.* (2019) reported a eutectic composition of 30 wt.% urea which melted at 69 ±3 °C.

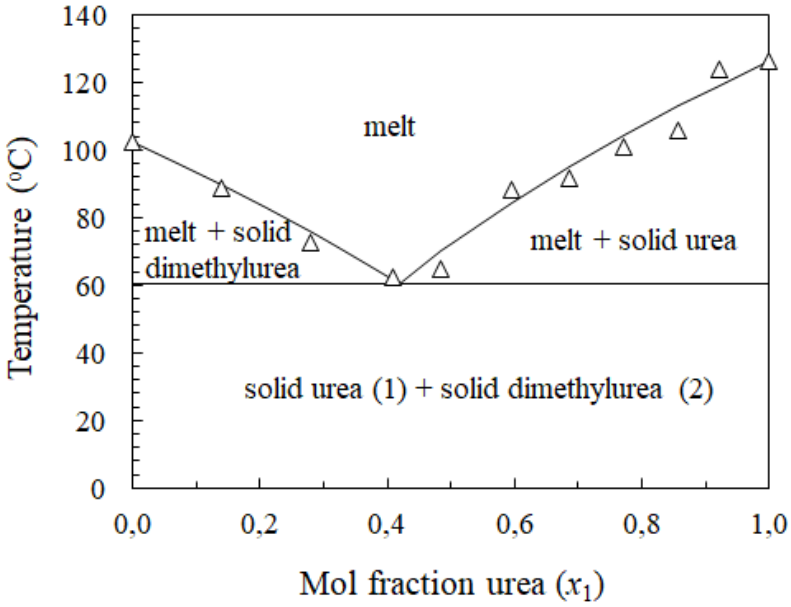

Figure 57: Liquid solid phase diagram for urea and 1,3-dimethylurea without modelling interaction.

The phase diagram predicted by the Porter model is shown in Figure 58. This model predicts a eutectic temperature of 58 °C at a composition of 41 wt.% urea (50 mol.%).

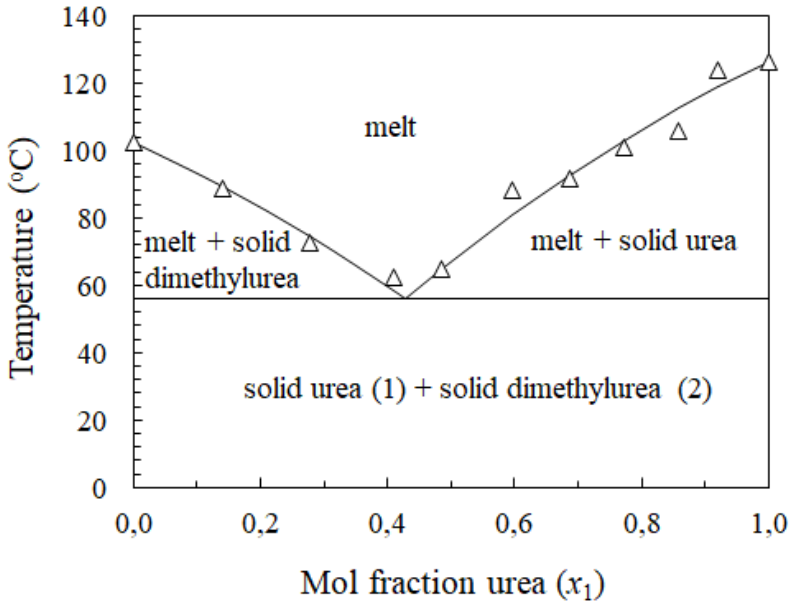

Figure 58: Liquid solid phase diagram for urea and 1,3-dimethylurea modelling interaction with the Porter model.

The Margules model in Equation 28, predicts a eutectic temperature of 59 °C at a composition of 32 wt.% urea (41 mol.%) as shown by Figure 59. A qualitative improvement can be seen by comparing the fits of Figure 58 and Figure 59. This improvement is also displayed in Table 10.

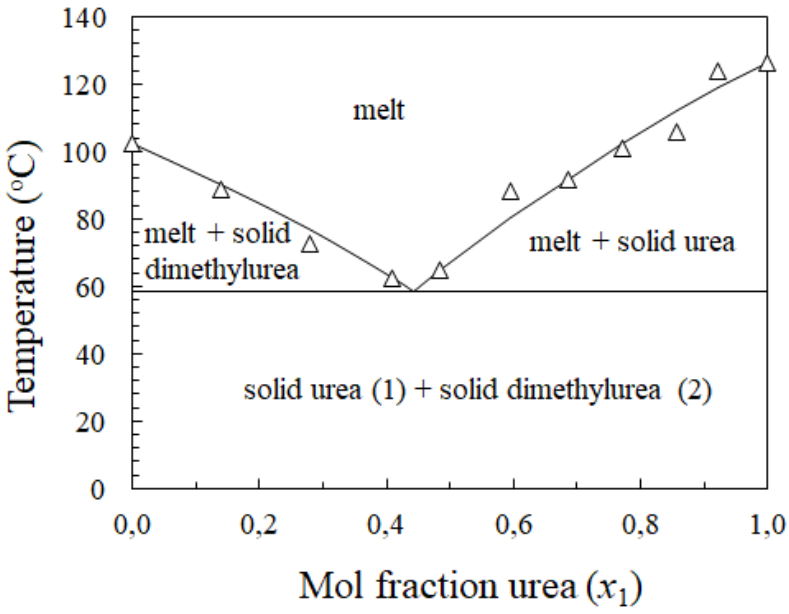

Figure 59: Liquid solid phase diagram for urea and 1,3-dimethylurea modelling interaction with the Margules interaction model.

The Wilson model in Equation 29, predicts a eutectic temperature of 57 °C at a composition of 34 wt.% urea (43 mol.%) as shown by Figure 59. Thus for the added complexity of the phase modelling, no substantial accuracy was gained.

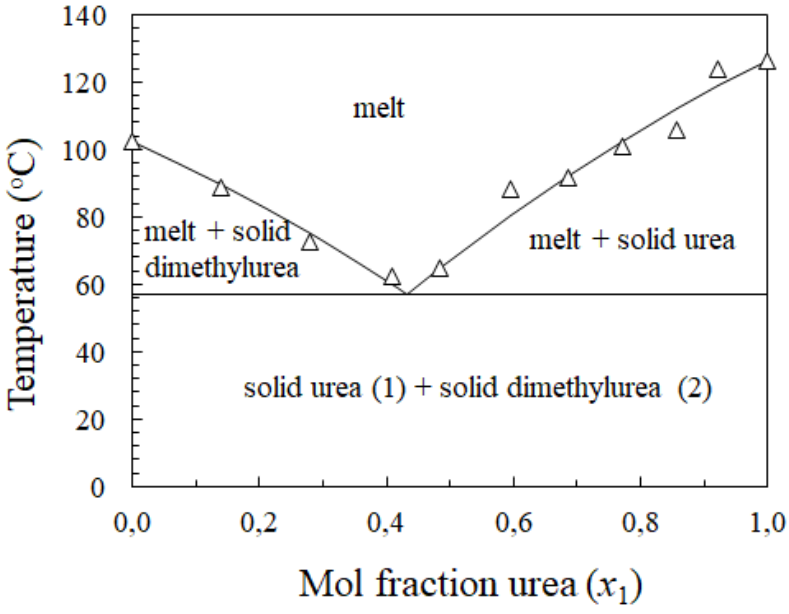

Figure 60: Liquid solid phase diagram for urea and 1,3-dimethylurea modelling interaction with the Wilson thermodynamic model.

Urea & acetamide eutectic modelling

Suriyanarayanan *et al.* (2019) studied the formation of eutectic mixtures of various organic salts including that of urea and acetamide. They found a eutectic composition of 33 wt.% urea (33 mol.%) and a eutectic temperature of 56 °C. Using Equation 1 and data from Table 9 the ideal eutectic phase diagram was plotted along the data points obtained in Figure 61.

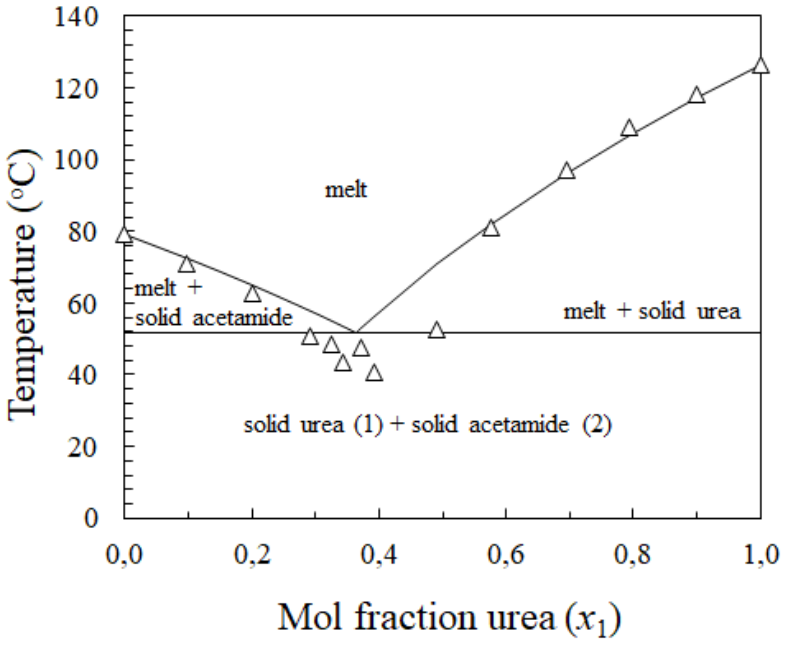

Figure 61: Liquid solid phase diagram for urea and acetamide without modelling interaction.

Figure 61 displays a clear opposing interaction between the compounds indicating the need of a thermodynamic model to more accurately predict the phase diagram. The Margules interaction model, Equation 28, displays a far better fit to the experimental data shown in Figure 62. This model predicts a eutectic melting point of 44 °C at 37 wt.% urea (37 mol.%).

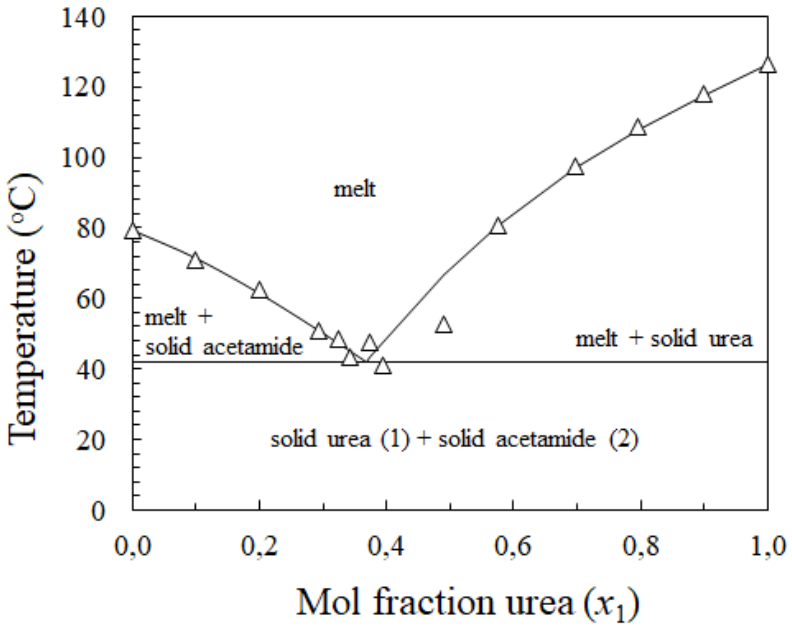

Figure 62: Liquid solid phase diagram for urea and acetamide modelling interaction with the Margules interaction model.

Summary of results

Table 10 summarises the interaction coefficients obtained from regression of the various models used. The table identifies a component 1 (urea) and a component 2 (1, 3-dimethylurea or acetamide). The identity of these components can be found in their respective figures or in the heading of that column.

Table 10: Summary of regressed interaction coefficients of organic salt eutectic systems.

Thermodynamic model	Symbol	UDE	UAE
Porter	A_P	−0.19	−0.98
Margules	$A_{1,2}$	0	−1.05
	$A_{2,1}$	−0.30	−0.22
Wilson	$\Lambda_{1,2}$	1.99	0.89
	$\Lambda_{2,1}$	0.51	2.24

The accuracy of the models where calculated as an R^2 statistical value. Table 11 summarizes these results for each system and each model.

Table 11: Summary of accuracy of various thermodynamic models which model a system's eutectic phase behaviour.

Thermodynamic model	Correlation coefficient (R^2)	
	UDE	UAE
No interaction	0.78	0.72
Porter	0.92	0.81
Margules	0.97	0.94
Wilson	0.97	0.95

Differential Scanning Calorimetry (DSC) of the UDE eutectic composition

The large deviation of the eutectic temperature obtained from experiments and that of literature was hypothesised to be due to the hygroscopicity and hence significant moisture content of the samples. Thus the DSC procedure for the casted samples, described in the Thermal gravimetric analysis (TGA) method section, was used. The "first round" of heating and cooling was meant to remove excess moisture, while the "second round" was used in the analysis shown in Figure 63. A melting endotherm for the eutectic composition of the UDE system was found to lie at 70 °C, similar to that of Suriyanarayanan *et al.* (2019). The melting endotherms of the pure components and that of the eutectic is plotted on Figure 63. The endotherms of the pure components match up well to the melting points stated in Table 9.

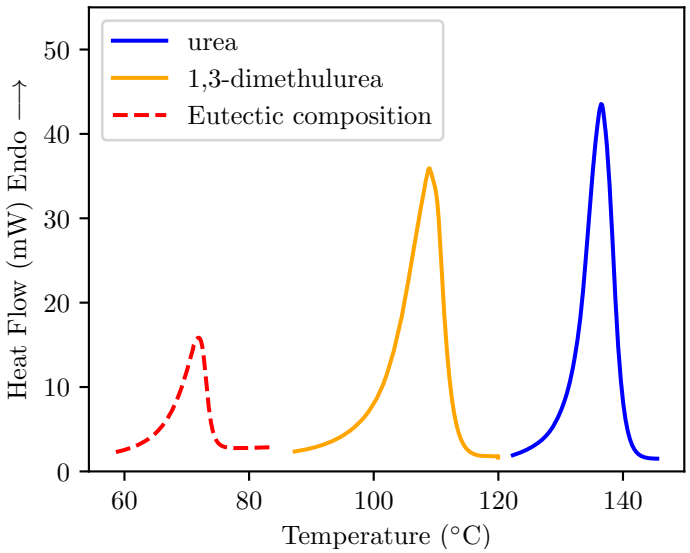

Figure 63: Melting endotherms of urea, 1,3-dimethylurea and the eutectic composition.

4.3.2 Morphology

Morphology of the UDE system

Powder X-ray diffractograms of the UDE system and its constituents are displayed in Figure 64. Each diffractogram shows clear,sharp and distinct reflections, indicating a high crystallinity.

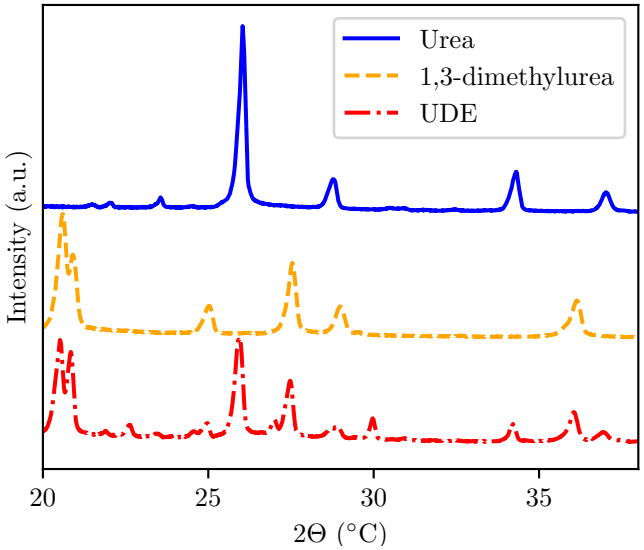

Figure 64: Diffractograms of pure component crystals and eutectic mixture crystals of urea and 1,3-dimethylurea.

All reflections shown on the UDE diffractogram line up well with that of its constituents apart from a minor reflection at 30° and one at 23° indicating a small amount of co-crystallisation of urea and 1,3-dimethylurea. It is hypothesised that this occurred at the grain boundaries where the growing pure component crystals impinged on one another during phase change.

Morphology of the UAE system

The UAE system was also analysed to see if co-crystallisation occurred. The diffractograms are plotted in Figure 65. Again sharp reflections indicate a material with low or no amorphicity. No reflections shown on the eutectic diffractogram are significantly different to a scaled sum of the reflections of its constituents. This indicated that urea and acetamide are insoluble in the solid phase and forms a proper eutectic.

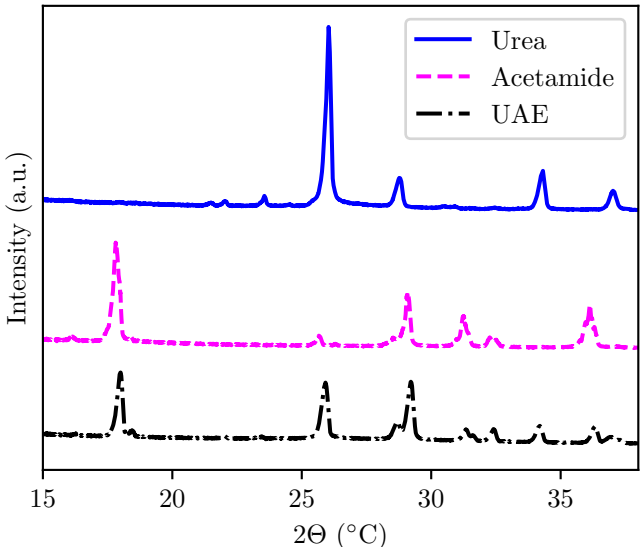

Figure 65: Diffractograms of pure component crystals and eutectic mixture crystals of urea and acetamide.

The high hygroscopicity observed during experiments of the UAE system lead to the decision to use the UDE (urea % 1,3-dimethylurea eutectic) system instead. All dissolution trials of the UDE system are discussed under the Amitraz compounding into dextrin nanocomposite and deep eutectic solvent matrices subsection.

4.4 Amitraz compounding into dextrin nanocomposite and deep eutectic solvent matrices

The objective of this research was to identify suitable matrices for the creation of solid-dosage forms. Amitraz was chosen as active ingredient for compounding with the selected matrices. One TPD system and one deep eutectic solvent system was selected to incorporate amitraz. The TPD composite was chosen based on its superior performance during extrusion, retrogradation and dissolution. The composition of the selected TPD system was that of S7 (containing 60 wt.% dextrin 18 wt.% water 18 wt.% glycerol 3 wt.% stearic acid and 1 wt.% nanocellulose). The organic salt system (urea & 1,3-dimethylurea eutectic) was selected due to its safe use, and limited hydrophilicity when compared to the other candidate system. The phase behaviour of this system was modelled was identified using the Margules interaction model (Equation 28) which predicts a eutectic composition of 32 wt.% urea which melts at 59 °C.

4.4.1 Thermoplastic dextrin composites as matrices for solid dosage forms

The control compound in this part of the investigation (A0) is identical to Sample S7. Sample A10 and A20 contained 10 wt.% and 20 wt.% amitraz respectively, where the remainder of the composite was identical to the ratio's sated for S7. The samples were produced via extrusion methods described in the Thermoplastic dextrin extrusion and film preparation section.

Dissolution

The typical dissolution experiment gave results similar to that obtained by Figure 52. The Hixson Crowell model for spherically shaped solids is given in this section again in Equation 30 and Equation 31 for clarity and ease of reading.

$$\sqrt[3]{M_0} - \sqrt[3]{M} = kt \tag{30}$$

$$k = k' \frac{\sqrt[3]{M_0}}{d_0} \tag{31}$$

The fitted intrinsic dissolution rate constants, k', are summarised in Figure 66.

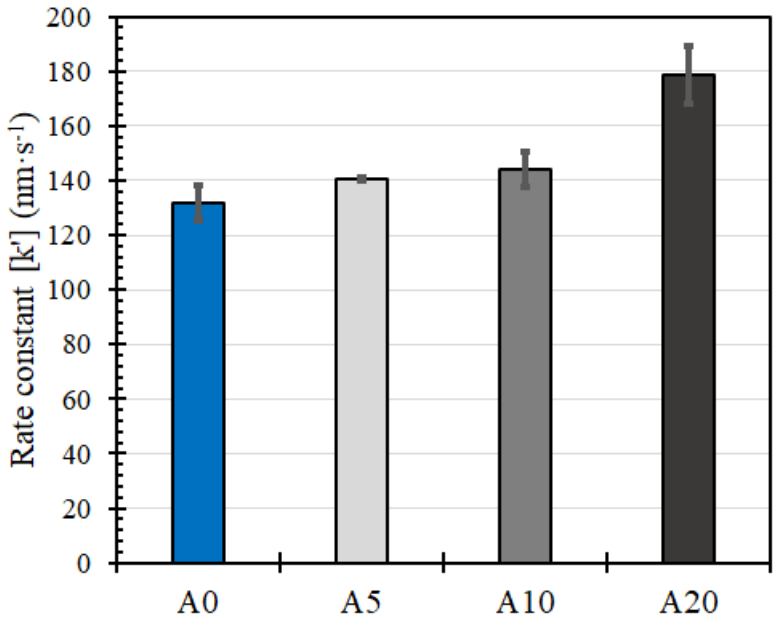

Figure 66: Dissolution rate constant comparison of thermoplastic dextrin incorporated with various amitraz loadings.

A significant effect of the amitraz is observed in the dissolution rate in Figure 66. An upward trend toward larger dissolution rates is indicated. This implies that higher loadings of amitraz increase the dissolution rate. Amitraz is a hydrophobic compound, thus a decrease in the dissolution rate was expected if the dosage form formed a completely homogeneous melt during extrusion. Obviously the chosen active ingredient was not compatible with the matrix enough for this to be the case. The increase in the dissolution rate is speculated to be due to the willingness of the matrix to rather be in solution than in a solid state with the hydrophobic compound.

Figure 67 shows residue particle sizes after dissolution. Sample S0 refers to the TPD compound containing only dextrin and plasticizer. The distribution of dextrin and this compound were both bimodal centred at similar diameters. This indicates that the compounding process, which converted the combination of dextrin, water, and glycerol into a thermoplastic material, did not materially change the D50 particle size observed in the dispersion. The implication is that the dextrin contains a cold-water-insoluble fraction that shows up in the PSD measurements. The CNF PSD was trimodal with a very wide range of particle sizes. It is possible, that the larger particles observed in Figure 67 and Figure 68 for A0 - A20, represent CNF agglomerates .

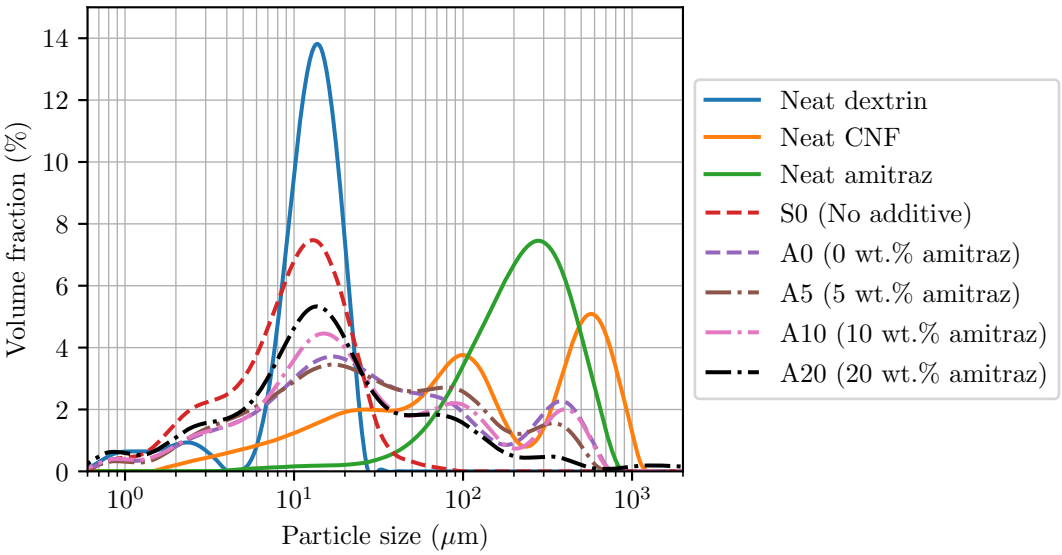

Figure 67: Residue sizes of dextrin thermoplastics compounded with the active ingredient at various loadings and its base components.

All the TPD PSD's in Figure 67 other than S0, are multimodal in nature with the different peaks probably associated with one or more of the constituents. The main peaks for sample A0 are approximately located at particle sizes corresponding to 15, 100, and 400 μm. The first represents, in the main, a contribution from the dextrin as this particle size is also observed for both dextrin and Sample S0.

Figure 68 is a scaled version of Figure 67 which helps to investigate the effect of the addition of amitraz and CNF to thermoplastic dextrin nanocomposites.

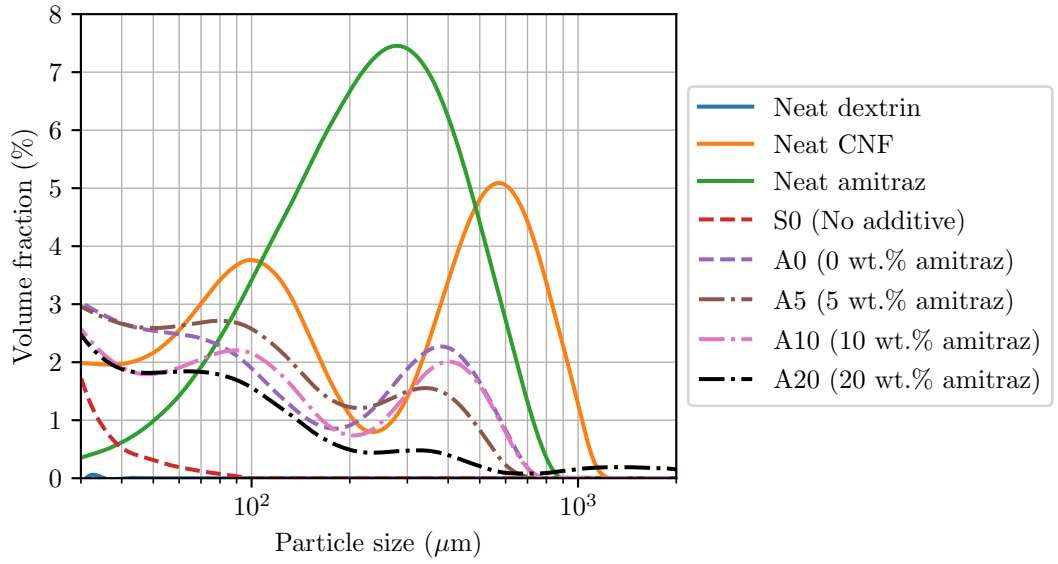

Figure 68: Influence of amitraz and cellulose nanofibres on residue sizes of thermoplastic dextrins.

The two larger sizes are attributed to the CNF as they more or less agree with the CNF peaks in Figure 68. As expected, these peaks all diminish in intensity, whereas the peak centred at ca. 15 μm grows in intensity as the amitraz content of the compound increases. This means that most of the amitraz particles released had that particular size. The implication is that formulating the amitraz into a dextrin-based solid dosage form can facilitate the delivery of particles that are much smaller than the original amitraz powder.

4.4.2 Deep eutectic solvent solid dosage form

As discussed in the Melt casting method, two disc sizes were analysed. The urea & 1,3-dimethylurea eutectic matrix (32 wt.% urea) was first melted at 70 °C, until a homogeneous mixture formed. The amitraz powder was then added to the molten matrix to form a solution containing 20 wt.% amitraz. All casts, prior to freezing were completely translucent. This indicates that the amitraz had melted at 70 °C, far below the stated melting point of 86 °C.

Dissolution rate of eutectic dosage forms

Two different disk sizes were analysed as discussed in the Melt casting method. The larger disk had a diameter of 100 mm and a height of 5 mm, while the smaller disk was 55 mm in diameter and 5 mm in height. Results from the dissolution trials of the urea % 1, 3-dimethylurea (UDE) system, and the amitraz loaded system are shown in Figure 69. The two disk sizes are shown on separate plots. The big disk is shown in Figure 69a), and the small disk in Figure 69b). Data points for the two disk sizes were too close together to logically show error bars.

A clear decrease in the dissolution rate is observed when casting with amitraz. This active ingredient is insoluble in water. The reduction in dissolution rate is attributed to the hydrophobic nature of the selected active ingredient.

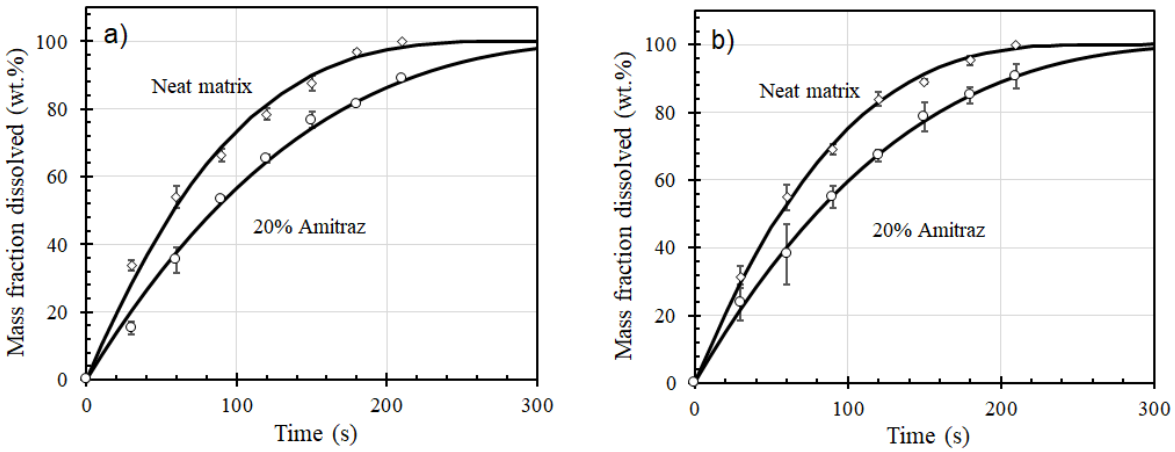

Figure 69: The effect of the incorporation of the hydrophobic active ingredient. The data points and model fit is also shown. Where a) represents the data points and fit of the big disk (ϕ 100 mm) and b), that of the small disk (ϕ 55 mm)

The fitted dissolution curves, based on the Hixson-Crowell model shown in Equation 17 and Equation 19, are shown in Figure 70. The dissolution times for both sizes were very similar. The smaller disk dissolved slightly faster for both compositions.

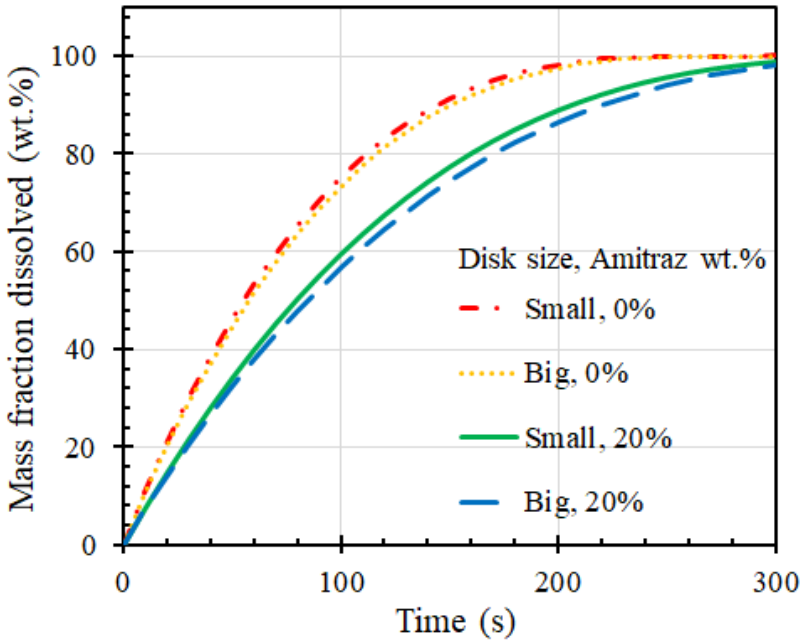

Figure 70: Modelled dissolution curves for big and small disks containing various amounts of amitraz.

As stated in the Melt casting method, the disc thickness was the same in both cases and the aspect ratios (diameter to height ratio) were relatively large (11 and 20). Therefore,

the diameter-independent dissolution time probably indicates that the large exposed area already large enough that external diffusion did not influence the dissolution rate.

The Hixson Crowell model for cylindrically shaped solids is given in this section again in Equation 32 and Equation 33 for clarity and ease of reading.

$$\sqrt[3]{M_0} - \sqrt[3]{M} = kt \tag{32}$$

$$k = k' \frac{\sqrt[3]{M_0}}{\sqrt[3]{H_0 d_0^2}} \tag{33}$$

According to the Hixson-Crowell model, the initial mass plays a key role in the dissolution rate, and dissolution time of solid particles. The fitted intrinsic rate constant for each shape and composition, *k'*, is displayed in Figure 71.

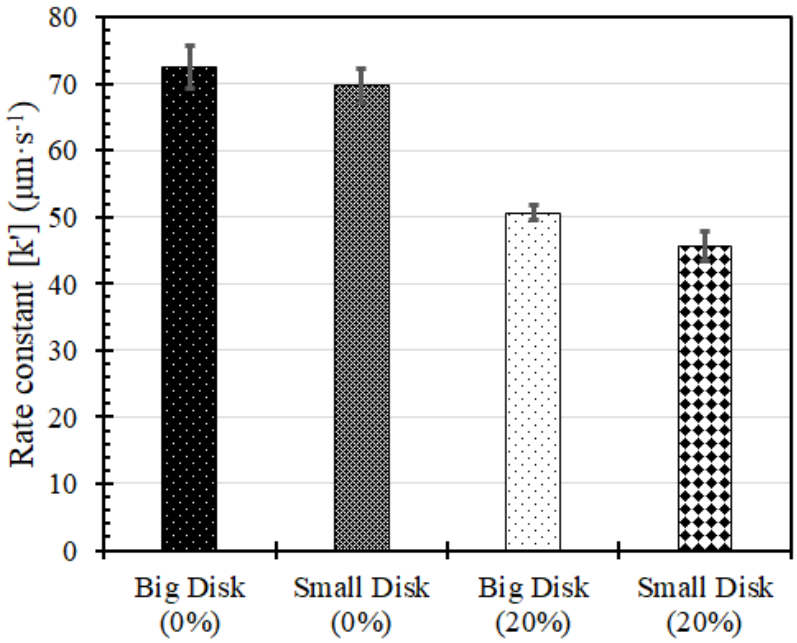

Figure 71: Dissolution rate constant comparison of eutectic disks of various sizes and amitraz loadings.

The dissolution times and dissolution rates of the larger and smaller disks are nearly identical given the error bars indicated on Figure 71. This is due to the high shear rate combined with the large exposed surface area. In conclusion we can safely say that the measurements do not contain any artefacts due to the shape of the matrix and the stirrer speed in the container. The differences between the plots labelled 0% and 20% are due

to different diffusion rates caused by the incorporation of amitraz. This is expected as amitraz is a hydrophobic compound.

Dissolution residue analysis

Figure 72 compares the particle size distributions of the solid dosage form dispersions after dissolution in water with that of the original neat powder. The results are reported in Table 12. The key finding is an almost order-of-magnitude reduction in the amitraz particle size as released from the solid dosage system as compared to the original powder.

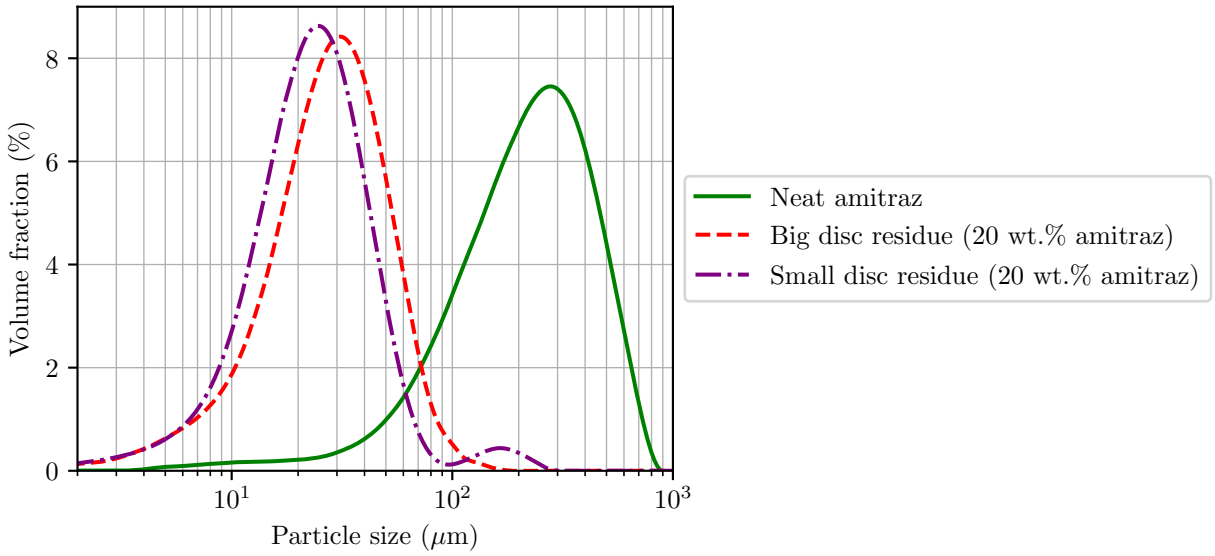

Figure 72: Deep eutectic dosage form dissolution residue analysis curves.

.

Two hypotheses are given for the observed results:

- The large particles indicated by the PSD results of the neat amitraz could in fact have been agglomerates of much smaller constituent particles. It could then be, that the processing of the amitraz-filled eutectic affected their dispersion as free individual particles.
- Solubilisation of the amitraz by the molten deep eutectic solvent presents a second alternative explanation. In this scenario, phase separation occurred during cooling of the homogeneous solution on or before solidification. This resulted in the formation of small amitraz domains that solidified as separate, much smaller particles trapped inside the eutectic matrix. These were subsequently released during the dissolution process.

Table 12: Particle size values for the neat amitraz powder and for dispersions obtained after dissolution of cast discs.

Sample	D10 (μm)	D50 (μm)	D90 (μm)
Amitraz (neat)	80.8 ± 3.7	240 ± 10	511 ± 28
Dispersion from small disc	9.30 ± 0.06	24.2 ± 0.8	49.8 ± 2.1
Dispersion from large disc	10.3 ± 0.3	29.8 ± 2.6	59.7 ± 11.8

The melting points of the casts were investigated to disprove one of the stated hypotheses which could explain the reduction of particle size shown in Figure 72 and quantified and summarized in Table 12. Figure 73 shows that the eutectic, filled with 20 wt.% amitraz, featured only one major endotherm. It is located at a slightly lower temperature range than the one observed for the urea & 1,3-dimethylurea eutectic. This, and the absence of a second endotherm closer to the melting point of the amitraz indicates that the active did indeed dissolve in the deep eutectic solvent which led to a further lowering of the melting point of the compound.

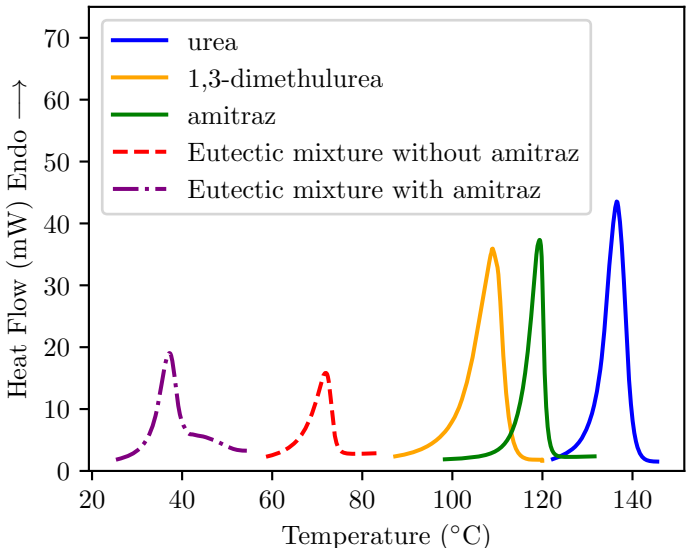

Figure 73: Melting endotherms of the eutectic dosage form and its constituents.

Figure 74 shows microscope images of the amitraz powder. It is clear that the neat active consists of monolithic particles larger that 100 μm in size. There is no clear agglomeration of smaller sizes found in any of the images taken.

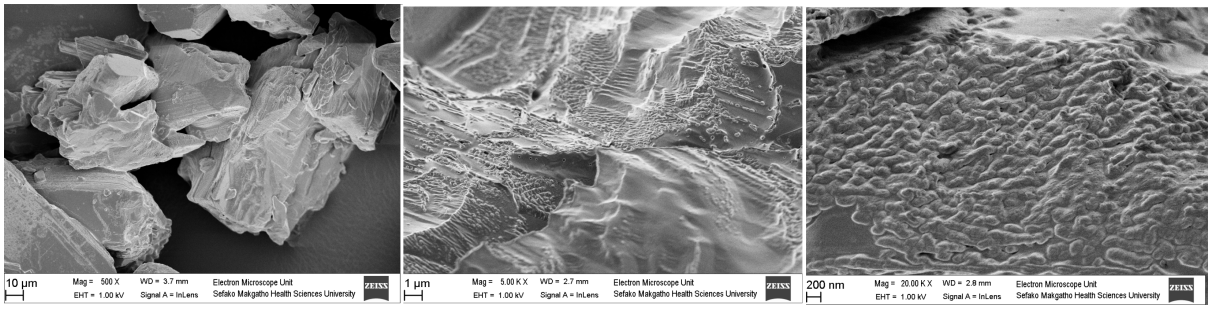

Figure 74: Electron microscope images of raw amitraz powder.

In conclusion, the results of the thermal analysis and imaging investigation proves that the active did dissolve in the matrix of the eutectic. It can also be concluded that the residue particles shown in Figure 72 were derived from the recrystallisation of amitraz from the deep eutectic solvent matrix.

5 Conclusions and recommendations

Two candidate solid dosage form matrix systems were investigated. The intended purpose of the matrix is to contain an active ingredient for agricultural applications. The matrix must be able to dissolve in water over a specified period of time and leave the accompanying insoluble active in the medium. The first candidate was that of thermoplastic dextrin nanocomposites and the second covered that of deep eutectic solvent matrices. The systems were characterised using ease of production, morphological relations, and dissolution rate. A commercially used acaricide, amitraz, was used to investigate how the selected matrix would interact with the addition of an active ingredient.

Water-soluble dextrin-based thermoplastic starch nanocomposites were prepared by melt processing in a twin-screw compounder. These composites contained a 1:1 mixture of water and glycerol as plasticizer in addition to 4.0 wt.% of selected additives or additive mixtures. The additives included cellulose nanofibres, stearic acid, and a layered double hydroxide clay. Cellulose nanofibres, included at 1.0 wt.%, significantly improved the melt strength and surface smoothness of the extruded strand.

The compounds all showed a beta transition close to -57 °C but the glass transition varied from 6 to 32 °C depending on the additives included in the formulation. The inclusion of the cellulose nanofibres at 1.0 wt.% or LDH nanoclays at up to 4.0 wt.% increased the bending modulus by about a factor of around three.

XRD analysis revealed that all samples, except for the one containing only stearic acid as sole additive, suffered from retrogradation on ageing for 98 days at room temperature and 75% relative humidity. HPDSC together with XRD showed the formation of stable amylose-lipid complexes. TPD samples containing LDH hinted at the exfoliation of the nanoclay, except in the presence of stearic acid, and in effect ALC's.

Dissolution trials in water were performed as per the intended purpose of the compound. The dissolution of the TPD granules left only micrometer-sized bio-based residues and followed Hixson–Crowell kinetics. The compound based on 1.0 wt.% cellulose nanofibres and 3.00 wt .% stearic acid was evaluated as the carrier matrix for amitraz. The dissolution time of ca. 5 mm granules was about 12 hours, even at a 20 wt.% active loading. The selected acaricide was released in the form of very fine particles, with a D50 of about 15 μm.

Nonionic deep eutectic solvents show potential as matrix materials useful for formulating rapid release dosage forms for water-insoluble pesticides. Advantages include low temperature ($< °100$ C) processing and mixing of the ingredients; the possibility of direct casting

of the required tablet shapes by pouring the molten mixture into the plastic packaging containers used for storage and transport; rapid release in water media via dissolution of the matrix; the automatic generation of a finely dispersed forms of the active through the process of melting the deep eutectic solvent; the dissolution of the active and its phase separation on cooling and solidification of the eutectic. This implies that fine grinding of the actives might not be necessary. The above features were exemplified using the acaricide, amitraz, incorporated into the urea - 1,3-dimethylurea eutectic.

6 References

Abbott, AP, Ahmed, EI, Prasad, K, Qader, IB and Ryder, KS (2017) "Liquid pharmaceuticals formulation by eutectic formation" *Fluid Phase Equilibria*, *448*, 2–8.

Abe, K, Iwamoto, S and Yano, H (2007) "Obtaining cellulose nanofibers with a uniform width of 15 nm from wood" *Biomacromolecules*, *8*, (10): 3276–3278.

Ahmad, FB and Williams, PA (1999) "Effect of salts on the gelatinization and rheological properties of sago starch" *Journal of Agricultural and Food Chemistry*, *47*, (8): 3359–3366.

Andrady, AL (2011) "Microplastics in the marine environment" *Marine Pollution Bulletin*, *62*, (8): 1596–1605.

APSC (2018) *Mark-Houwink Parameters for Polymers* URL: `http://www.ampolymer.com/Mark-Houwink.html`.

Area, MR, Rico, M, Montero, B, Barral, L, Bouza, R, López, J and Ramírez, C (2019) "Corn starch plasticized with isosorbide and filled with microcrystalline cellulose: Processing and characterization" *Carbohydrate Polymers*, *206*, 726–733.

Atkins, PW, De Paula, J and Keeler, J (2018) *Atkins' physical chemistry*, 11th ed. Oxford University Press, Oxford, UK.

Banker, GS and Rhodes, CT (1990) *Modern pharmaceutics*, 2nd ed. vol. 40 New York: Marcel Dekker, New York.

Battegazzore, D, Bocchini, S, Nicola, G, Martini, E and Frache, A (2015) "Isosorbide, a green plasticizer for thermoplastic starch that does not retrogradate" *Carbohydrate Polymers*, *119*, 78–84.

Bayer Southern Africa (2020) *Cattle Products* URL: `http://animalhealth.bayer.co.za/scripts/pages/en/livestock/cattle/index.php`.

Benelli, G, Maggi, F, Canale, A and Mehlhorn, H (2019) "Lyme disease is on the rise-How about tick repellents? A global view" *Entomologia Generalis*, *39*, (2): 61–72.

Bhatnagar, S and Hanna, MA (1997) "Modification of microstructure of starch extruded with selected lipids" *Starch-Stärke*, *49*, (1): 12–20.

Bica, K, Shamshina, J, Hough, WL, MacFarlane, DR and Rogers, RD (2011) "Liquid forms of pharmaceutical co-crystals: exploring the boundaries of salt formation" *Chemical Communications*, *47*, (8): 2267–2269.

Biliaderis, C, Arvanitoyannis, I, Izydorczyk, M and Prokopowich, D (1997) "Effect of hydrocolloids on gelatinization and structure formation in concentrated waxy maize and wheat starch gels" *Starch-Stärke*, *49*, (7-8): 278–283.

Biliaderis, C and Seneviratne, H (1990) "On the supermolecular structure and metastability of glycerol monostearate-amylose complex" *Carbohydrate Polymers*, *13*, (2): 185–206.

Biliaderis, C and Tonogai, J (1991) "Influence of lipids on the thermal and mechanical properties of concentrated starch gels" *Journal of Agricultural and Food Chemistry*, *39*, (5): 833–840.

Buléon, A, Delage, M, Brisson, J and Chanzy, H (1990) "Single crystals of V amylose complexed with isopropanol and acetone" *International Journal of Biological Macromolecules*, *12*, (1): 25–33.

Cano, A, Jiménez, A, Cháfer, M, Gónzalez, C and Chiralt, A (2014) "Effect of amylose: amylopectin ratio and rice bran addition on starch films properties" *Carbohydrate Polymers*, *111*, 543–555.

Castaño, J, Rodrıguez-Llamazares, S, Contreras, K, Carrasco, C, Pozo, C, Bouza, R, Franco, C and Giraldo, D (2014) "Horse chestnut (Aesculus hippocastanum L.) starch: Basic physico-chemical characteristics and use as thermoplastic material" *Carbohydrate polymers*, *112*, 677–685.

Castro, J and D'Agnes, L (2008) "Fishing for families: Reproductive health and integrated coastal management in the Philippines" *Focus*, *15*,

Chauhan, G, Sharma, P and Bains, G (2003) "Effect of Extrusion Cooking on X-Ray Diffraction Characteristics of Rice and Rice–Legume Blends" *International Journal of Food Properties*, *6*, (1): 127–133.

Cheetham, NW and Tao, L (1998) "Variation in crystalline type with amylose content in maize starch granules: an X-ray powder diffraction study" *Carbohydrate Polymers*, *36*, (4): 277–284.

Chen, L, Tian, Y, McClements, DJ, Huang, M, Zhu, B, Wang, L, Sun, B, Ma, R, Cai, C and Jin, Z (2019) "A simple and green method for preparation of non-crystalline granular starch through controlled gelatinization" *Food Chemistry*, *274*, 268–273.

Cherukuvada, S and Nangia, A (2014) "Eutectics as improved pharmaceutical materials: design, properties and characterization" *Chemical Communications*, *50*, (8): 906–923.

Chiou, WL and Riegelman, S (1971) "Pharmaceutical applications of solid dispersion systems" *Journal of Pharmaceutical Sciences*, *60*, (9): 1281–1302.

Codex Alimentarius (2020) *Pesticide Index* URL: `http://www.fao.org/fao-who-codexalimentarius/codex-texts/dbs/pestres/pesticides/en/`.

Corrigan, O, Murphy, C and Timoney, R (1979) "Dissolution properties of polyethylene glycols and polyethylene glycol-drug systems" *International Journal of Pharmaceutics*, *4*, (1): 67–74.

Corta, E, Bakkali, A, Berrueta, L, Gallo, B and Vicente, F (1999) "Kinetics and mechanism of amitraz hydrolysis in aqueous media by HPLC and GC-MS" *Talanta*, *48*, (1): 189–199.

Czuchajowska, Z, Sievert, D and Pomeranz, Y (1991) "Enzyme-resistant starch. IV. Effects of complexing lipids" *Cereal Chemistry*, *68*, (5): 537–542.

D'Silva, TV, Taylor, JR and Emmambux, MN (2011) "Enhancement of the pasting properties of teff and maize starches through wet–heat processing with added stearic acid" *Journal of Cereal Science*, *53*, (2): 192–197.

De Blaey, C and Van der Graaff, H (1977) "Dissolution kinetics of soluble nondisintegrating disks" *Journal of Pharmaceutical Sciences*, *66*, (12): 1696–1699.

Delgado, CL (2003) *Fish to 2020: Supply and demand in changing global markets*, vol. 62 WorldFish, Washington D.C., USA.

Della Gatta, G and Ferro, D (1987) "Enthalpies of fusion and solid-to-solid transition, entropies of fusion for urea and twelve alkylureas" *Thermochimica Acta*, *122*, (1): 143–152.

Dobler, G (2018) "Tick-borne encephalitis and its global importance" *Microbiology Australia*,

Domalski, ES and Hearing, ED (1996) "Heat capacities and entropies of organic compounds in the condensed phase. Volume III" *Journal of Physical and Chemical Reference Data*, *25*, (1): 1–525.

Dong, S, Jia, Y, Xu, X, Luo, J, Han, J and Sun, X (2019) "Crystallization and properties of poly (ethylene terephthalate)/layered double hydroxide nanocomposites" *Journal of Colloid and Interface Science*, *539*, 54–64.

Dufresne, A, Dupeyre, D and Vignon, MR (2000) "Cellulose microfibrils from potato tuber cells: processing and characterization of starch–cellulose microfibril composites" *Journal of Applied Polymer Science*, *76*, (14): 2080–2092.

Fahmy, R, Marnane, B, Bensley, D and Hollenbeck, RG (2002) "Dissolution test development for complex veterinary dosage forms: oral boluses" *AAPS PharmSci*, *4*, (4): 137–144.

Fahy, GM (2010) "Cryoprotectant toxicity neutralization" *Cryobiology*, *60*, (3): S45–S53.

Ferreira, F, Pinheiro, I, Gouveia, R, Thim, G and Lona, L (2018) "Functionalized cellulose nanocrystals as reinforcement in biodegradable polymer nanocomposites" *Polymer Composites*, *39*, E9–E29.

Ferrero, C, Martino, M and Zaritzky, N (1993) "Effect of freezing rate and xanthan gum on the properties of corn starch and wheat flour pastes" *International Journal of Food Science & Technology*, *28*, (5): 481–498.

Fisher, JR and Dowling, AP (2010) "Modern methods and technology for doing classical taxonomy" *Acarologia*, *50*, (3): 395–409.

Frost, K, Kaminski, D, Kirwan, G, Lascaris, E and Shanks, R (2009) "Crystallinity and structure of starch using wide angle X-ray scattering" *Carbohydrate Polymers*, *78*, (3): 543–548.

Fu, Z, Chen, J, Luo, SJ, Liu, CM and Liu, W (2015) "Effect of food additives on starch retrogradation: A review" *Starch-Stärke*, *67*, (1-2): 69–78.

Funami, T, Kataoka, Y, Omoto, T, Goto, Y, Asai, I and Nishinari, K (2005) "Food hydrocolloids control the gelatinization and retrogradation behavior of starch. 2b. Functions of guar gums with different molecular weights on the retrogradation behavior of corn starch" *Food Hydrocolloids*, *19*, (1): 25–36.

García, NL, Ribba, L, Dufresne, A, Aranguren, M and Goyanes, S (2011) "Effect of glycerol on the morphology of nanocomposites made from thermoplastic starch and starch nanocrystals" *Carbohydrate Polymers*, *84*, (1): 203–210.

Garrido, EM, Delerue-Matos, C, Lima, J and Brett, AO (2004) "Electrochemical methods in pesticides control" *Analytical letters*, *37*, (9): 1755–1791.

Garrozzo, D, Impallomeni, G, Spina, E, Sturiale, L and Zanetti, F (1995) "Matrix-assisted laser desorption/ionization mass spectrometry of polysaccharides" *Rapid Communications in Mass Spectrometry*, *9*, (10): 937–941.

Geyer, R, Jambeck, JR and Law, KL (2017) "Production, use, and fate of all plastics ever made" *Science Advances*, *3*, (7): e1700782.

Gong, G, Mathew, AP and Oksman, K (2011) "Strong aqueous gels of cellulose nanofibers and nanowhiskers isolated from softwood flour" *TAPPI Journal*, *10*, (2): 42565.

Grandin, T (2010) *Explanation of Dip Vat Entrance Design* URL: `https://www.grandin.com/design/blueprint/enter.dipvat.html`.

Greene, SA (2013) *Sittig's handbook of pesticides and agricultural chemicals*, 2nd ed. William Andrew.

Greenspan, L (1977) "Humidity fixed points of binary saturated aqueous solutions" *Journal of Research of the National Bureau of Standards*, *81*, (1): 89–96.

Gudmundsson, M (1992) "Effects of an added inclusion-amylose complex on the retrogradation of some starches and amylopectin" *Carbohydrate Polymers*, *17*, (4): 299–304.

Gudmundsson, M and Eliasson, AC (1990) "Retrogradation of amylopectin and the effects of amylose and added surfactants/emulsifiers" *Carbohydrate Polymers*, *13*, (3): 295–315.

Hansen, M (2013) *EPA should ban arsenic-containing pesticides* URL: https://advocacy.consumerreports.org/press_release/epa-should-ban-arsenic-containing-pesticides/.

Hardee, GE and Baggo, JD (1998) *Development and formulation of veterinary dosage forms*, 2nd ed. CRC Press.

Hasnain, S (1998) "Review on sustainable thermal energy storage technologies, Part II: cool thermal storage" *Energy Conversion and Management*, *39*, (11): 1139–1153.

Heng, D, Cutler, DJ, Chan, HK, Yun, J and Raper, JA (2008) "What is a suitable dissolution method for drug nanoparticles?" *Pharmaceutical research*, *25*, (7): 1696–1701.

Hess, H (1985) *Pharmaceutical dosage forms and their use*, 1st ed. Hans Huber Publishers, Bern.

Hibino, T and Kobayashi, M (2005) "Delamination of layered double hydroxides in water" *Journal of Materials Chemistry*, *15*, (6): 653–656.

Hietala, M, Mathew, AP and Oksman, K (2013) "Bionanocomposites of thermoplastic starch and cellulose nanofibers manufactured using twin-screw extrusion" *European Polymer Journal*, *49*, (4): 950–956.

Hülsmann, S, Backensfeld, T, Keitel, S and Bodmeier, R (2000) "Melt extrusion–an alternative method for enhancing the dissolution rate of 17β-estradiol hemihydrate" *European Journal of Pharmaceutics and Biopharmaceutics*, *49*, (3): 237–242.

ILO (2020) *Amitraz* URL: http://www.ilo.org/dyn/icsc/showcard.display?p_version=2&p_card_id=0098.

Ilo, S, Tomschik, U, Berghofer, E and Mundigler, N (1996) "The effect of extrusion operating conditions on the apparent viscosity and the properties of extrudates in twin-screw extrusion cooking of maize grits" *LWT-Food Science and Technology*, *29*, (7): 593–598.

Iwamoto, S, Abe, K and Yano, H (2008) "The effect of hemicelluloses on wood pulp nanofibrillation and nanofiber network characteristics" *Biomacromolecules*, *9*, (3): 1022–1026.

Jiménez, A, Fabra, MJ, Talens, P and Chiralt, A (2012) "Effect of sodium caseinate on properties and ageing behaviour of corn starch based films" *Food Hydrocolloids*, *29*, (2): 265–271.

Jiménez, A, Fabra, MJ, Talens, P and Chiralt, A (2013) "Phase transitions in starch based films containing fatty acids. Effect on water sorption and mechanical behaviour" *Food Hydrocolloids*, *30*, (1): 408–418.

Jiugao, Y, Ning, W and Xiaofei, M (2005) "The effects of citric acid on the properties of thermoplastic starch plasticized by glycerol" *Starch-Stärke*, *57*, (10): 494–504.

Jongejan, F and Uilenberg, G (2004) "The global importance of ticks" *Parasitology*, *129*, (S1): S3–S14.

Jovanovich, G and Añón, MC (1999) "Amylose–lipid complex dissociation. A study of the kinetic parameters" *Biopolymers: Original Research on Biomolecules*, *49*, (1): 81–89.

Jung, JY, Yoo, SD, Lee, SH, Kim, KH, Yoon, DS and Lee, KH (1999) "Enhanced solubility and dissolution rate of itraconazole by a solid dispersion technique" *International journal of pharmaceutics*, *187*, (2): 209–218.

Junquera, P (2015) *Dipping livestock to control ticks, flies, mites, lice, blowfly strike and other parasites on cattle, sheep, goats, pig and poultry* URL: `https://parasitipedia.net/index.php?option=com_content&view=article&id=2427&Itemid=2683`.

Keszei, S, Szabó, A, Marosi, G, Anna, P and Nagy, S (2006) "Use of thermoplastic starch in continuous pharmaceutical process" in: *Macromolecular Symposia* vol. 239 1 Wiley Online Library: pp. 101–104.

Khanna, S and Tester, RF (2006) "Influence of purified konjac glucomannan on the gelatinisation and retrogradation properties of maize and potato starches" *Food Hydrocolloids*, *20*, (5): 567–576.

Kunz, S and Kemp, D (1994) "Insecticides and acaricides: resistance and environmental impact" *Revue Scientifique et Technique-Office International des Epizooties*, *13*, (4): 1249–1286.

Kvien, I, Sugiyama, J, Votrubec, M and Oksman, K (2007) "Characterization of starch based nanocomposites" *Journal of Materials Science*, *42*, (19): 8163–8171.

Law, D, Wang, W, Schmitt, EA, Qiu, Y, Krill, SL and Fort, JJ (2003) "Properties of rapidly dissolving eutectic mixtures of poly (ethylene glycol) and fenofibrate: the eutectic microstructure" *Journal of Pharmaceutical Sciences*, *92*, (3): 505–515.

Lendvai, L, Kmetty, Á and Karger-Kocsis, J (2017) "Preparation and properties of thermoplastic starch/bentonite nanocomposites" in: *Materials Science Forum* vol. 885 Trans-Tech Publications: pp. 129–134.

Lendvai, L, Sajó, I and Karger-Kocsis, J (2019) "Effect of storage time on the structure and mechanical properties of starch/bentonite nanocomposites" *Starch-Stärke*, *71*, (1-2): 1800123.

Li, Y, Ye, F, Wang, A, Wang, D, Yang, B, Zheng, Q, Sun, G and Gao, X (2016) "Chronic arsenic poisoning probably caused by arsenic-based pesticides: findings from an investigation study of a household" *International Journal of Environmental Research and Public Health*, *13*, (1): 133.

Liu, H, Xie, F, Yu, L, Chen, L and Li, L (2009) "Thermal processing of starch-based polymers" *Progress in Polymer Science*, *34*, (12): 1348–1368.

Liu, H, Yu, L, Xie, F and Chen, L (2006) "Gelatinization of cornstarch with different amylose/amylopectin content" *Carbohydrate Polymers*, *65*, (3): 357–363.

Liu, H, Eskin, NM and Cui, SW (2003) "Interaction of wheat and rice starches with yellow mustard mucilage" *Food Hydrocolloids*, *17*, (6): 863–869.

Liu, Q and Thompson, DB (1998) "Effects of moisture content and different gelatinization heating temperatures on retrogradation of waxy-type maize starches" *Carbohydrate Research*, *314*, (3-4): 221–235.

Lobell, DB, Burke, MB, Tebaldi, C, Mastrandrea, MD, Falcon, WP and Naylor, RL (2008) "Prioritizing climate change adaptation needs for food security in 2030" *Science*, *319*, (5863): 607–610.

López, CA, Vries, AH de and Marrink, SJ (2012) "Amylose folding under the influence of lipids" *Carbohydrate Research*, *364*, 1–7.

Magnarelli, LA (2009) "Global importance of ticks and associated infectious disease agents" *Clinical Microbiology Newsletter*, *31*, (5): 33–37.

Margarit, MV, Rodriguez, IC and Cerezo, A (1994) "Physical characteristics and dissolution kinetics of solid dispersions of ketoprofen and polyethylene glycol 6000" *International Journal of Pharmaceutics*, *108*, (2): 101–107.

Mateescu, M, Ispas-Szabo, P and Assaad, E (2015) "Starch and derivatives as pharmaceutical excipients: From nature to pharmacy" *Controlled Drug Delivery*, 21–84.

Maurer, HW (2009) "Chapter 18 - Starch in the Paper Industry", in: *Starch*, BeMiller, J and Whistler, R (Eds.), 3rd ed. Food Science and Technology Academic Press, San Diego: pp. 657–713.

Maurice, T, Slade, L, Sirett, R and Page, C (1985) "Polysaccharide-water interactions—thermal behavior of rice starch", in: *Properties of Water in Foods*, pp. 211–227.

Mayersohn, M and Gibaldi, M (1966) "New method of solid-state dispersion for increasing dissolution rates" *Journal of Pharmaceutical Sciences*, *55*, (11): 1323–1324.

Mercier, C, Charbonniere, R, Grebaut, J and De la Gueriviere, J (1980) "Formation of amylose-lipid complexes by twin-screw extrusion cooking of manioc starch" *Cereal Chemistry*, *57*, (1): 4–9.

Mullen, GR and Durden, LA (2009) *Medical and veterinary entomology*, Academic Press.

Nafchi, AM, Moradpour, M, Saeidi, M and Alias, AK (2013) "Thermoplastic starches: Properties, challenges, and prospects" *Starch-Stärke*, *65*, (1-2): 61–72.

National Center for Biotechnology Information (2020) *Amitraz* URL: `https://pubchem.ncbi.nlm.nih.gov/compound/Amitraz`.

Nindiyasari, F, Griesshaber, E, Zimmermann, T, Manian, AP, Randow, C, Zehbe, R, Fernandez-Diaz, L, Ziegler, A, Fleck, C and Schmahl, WW (2016) "Characterization and mechanical properties investigation of the cellulose/gypsum composite" *Journal of Composite Materials*, *50*, (5): 657–672.

Ning, W, Jiugao, Y, Xiaofei, M and Ying, W (2007) "The influence of citric acid on the properties of thermoplastic starch/linear low-density polyethylene blends" *Carbohydrate Polymers*, *67*, (3): 446–453.

No bite is right (2017) *What are ticks?* URL: https://www.nobiteisright.ca/en/parasites/ticks/.

Obiro, WC, Sinha Ray, S and Emmambux, MN (2012) "V-amylose structural characteristics, methods of preparation, significance, and potential applications" *Food Reviews International*, *28*, (4): 412–438.

Ojijo, V and Ray, SS (2013) "Processing strategies in bionanocomposites" *Progress in Polymer Science*, *38*, (10-11): 1543–1589.

Oliveira, LC, Barros, JH, Rosell, CM and Steel, CJ (2017) "Physical and thermal properties and X-ray diffraction of corn flour systems as affected by whole grain wheat flour and extrusion conditions" *Starch-Stärke*, *69*, (9-10): 1600299.

Onteniente, JP, Abbès, B and Safa, LH (2000) "Fully biodegradable lubricated thermoplastic wheat starch: mechanical and rheological properties of an injection grade" *Starch-Stärke*, *52*, (4): 112–117.

Ottenhof, MA and Farhat, I (2004) "The effect of gluten on the retrogradation of wheat starch" *Journal of Cereal Science*, *40*, (3): 269–274.

Panyoo, AE and Emmambux, MN (2017) "Amylose–lipid complex production and potential health benefits: A mini-review" *Starch-Stärke*, *69*, (7-8): 1600203.

Pelletier, DL, Frongillo Jr, EA, Schroeder, DG and Habicht, JP (1995) "The effects of malnutrition on child mortality in developing countries." *Bulletin of the World Health Organization*, *73*, (4): 443.

Pérez, S and Bertoft, E (2010) "The molecular structures of starch components and their contribution to the architecture of starch granules: A comprehensive review" *Starch-Stärke*, *62*, (8): 389–420.

Piesman, J and Eisen, L (2008) "Prevention of tick-borne diseases" *Annual Review of Entomology*, *53*, 323–343.

Pohorecka, K, Kiljanek, T, Antczak, M, Skubida, P, Semkiw, P and Posyniak, A (2018) "Amitraz marker residues in honey from honeybee colonies treated with Apiwarol" *Journal of veterinary research*, *62*, (3): 297–301.

Porter, R, Norman, R and Gilbert, L (2011) "Controlling tick-borne diseases through domestic animal management: a theoretical approach" *Theoretical Ecology*, *4*, (3): 321–339.

Przybyłek, M and Cysewski, P (2018) "Distinguishing cocrystals from simple eutectic mixtures: phenolic acids as potential pharmaceutical coformers" *Crystal Growth & Design*, *18*, (6): 3524–3534.

Rai, U and Rai, R (1998) "Physical chemistry of organic eutectics" *Journal of Thermal Analysis and Calorimetry*, *53*, (3): 883–893.

Raniya, A (2014) *Comparison between Starch, Glycogen and Cellulose* URL: `https://www.bankofbiology.com/2014/07/comparison-between-starch-glycogen-and.html`.

Raphaelides, S, Arsenoudi, K, Exarhopoulos, S and Xu, ZM (2010) "Effect of processing history on the functional and structural characteristics of starch–fatty acid extrudates" *Food Research International*, *43*, (1): 329–341.

Raphaelides, S, Dimitreli, G, Exarhopoulos, S, Kokonidis, G and Tzani, E (2011) "Effect of processing history on the physicochemical and structural characteristics of starch–fatty acid extrudates plasticized with glycerol" *Carbohydrate Polymers*, *83*, (2): 727–736.

Rodriguez-Gonzalez, F, Ramsay, B and Favis, B (2003) "High performance LDPE/thermoplastic starch blends: a sustainable alternative to pure polyethylene" *Polymer*, *44*, (5): 1517–1526.

Rodriguez-Gonzalez, F, Ramsay, B and Favis, B (2004) "Rheological and thermal properties of thermoplastic starch with high glycerol content" *Carbohydrate Polymers*, *58*, (2): 139–147.

Russell, PL (1987) "Gelatinisation of starches of different amylose/amylopectin content. A study by differential scanning calorimetry" *Journal of Cereal Science*, *6*, (2): 133–145.

Samutsri, W and Suphantharika, M (2012) "Effect of salts on pasting, thermal, and rheological properties of rice starch in the presence of non-ionic and ionic hydrocolloids" *Carbohydrate Polymers*, *87*, (2): 1559–1568.

Sekiguchi, K and Obi, N (1961) "Studies on Absorption of Eutectic Mixture. I. A Comparison of the Behavior of Eutectic Mixture of Sulfathiazole and that of Ordinary Sulfathiazole in Man." *Chemical and Pharmaceutical Bulletin*, *9*, (11): 866–872.

Shi, J, Shan, Y, Tian, Y, Wan, Y, Zheng, Y and Feng, Y (2016) "Hydrophilic sulfonic acid-functionalized micro-bead silica for dehydration of sorbitol to isosorbide" *RSC Advances*, *6*, (16): 13514–13521.

Shi, R, Zhang, Z, Liu, Q, Han, Y, Zhang, L, Chen, D and Tian, W (2007) "Characterization of citric acid/glycerol co-plasticized thermoplastic starch prepared by melt blending" *Carbohydrate Polymers*, *69*, (4): 748–755.

Smith, B (2015) "Solubility and Dissolution" *Remington Education: Physical Pharmacy*, 31–50.

Stoler, E and Warner, JC (2015) "Non-covalent derivatives: cocrystals and eutectics" *Molecules*, *20*, (8): 14833–14848.

Stott, PW, Williams, AC and Barry, BW (1998) "Transdermal delivery from eutectic systems: enhanced permeation of a model drug, ibuprofen" *Journal of Controlled Release*, *50*, (1-3): 297–308.

Sun, J, Zhao, R, Zeng, J, Li, G and Li, X (2010) "Characterization of destrins with different dextrose equivalents" *Molecules*, *15*, (8): 5162–5173.

Suriyanarayanan, S, Olsson, GD, Kathiravan, S, Ndizeye, N and Nicholls, IA (2019) "Non-Ionic Deep Eutectic Liquids: Acetamide–Urea Derived Room Temperature Solvents" *International Journal of Molecular Sciences*, *20*, (12): 2857.

Tanetrungroj, Y and Prachayawarakorn, J (2015) "Effect of starch types on properties of biodegradable polymer based on thermoplastic starch process by injection molding technique" *Songklanakarin Journal of Science and Technology*, *37*, (2): 193–199.

Tian, J and Guo, Q (2014) "Thermal decomposition of hydrocalumite over a temperature range of 400–1500 °C and its structure reconstruction in water" *Journal of Chemistry*, *2014*, (17).

Tokiwa, Y, Calabia, BP, Ugwu, CU and Aiba, S (2009) "Biodegradability of plastics" *International Journal of Molecular Sciences*, *10*, (9): 3722–3742.

US Department of Health & Human Services (2019a) *How ticks survive* URL: `https://www.cdc.gov/ticks/life_cycle_and_hosts.html`.

US Department of Health & Human Services (2019b) *RMSF: deadly, but preventable* URL: `https://www.cdc.gov/features/rmsf/index.html`.

Vaezi, K, Asadpour, G and Sharifi, H (2019) "Effect of ZnO nanoparticles on the mechanical, barrier and optical properties of thermoplastic cationic starch/montmorillonite biodegradable films" *International Journal of Biological Macromolecules*, *124*, 519–529.

Vähäsalo, L and Holmbom, B (2004) "Reliable spectrophotometric determination of starch concentration in papermaking process waters" *Nordic Pulp & Paper Research Journal*, *19*, (1): 75–77.

Van Hung, P, Vien, NL and Phi, NTL (2016) "Resistant starch improvement of rice starches under a combination of acid and heat-moisture treatments" *Food Chemistry*, *191*, 67–73.

Van Soest, J, Hulleman, S, De Wit, D and Vliegenthart, J (1996) "Crystallinity in starch bioplastics" *Industrial Crops and Products*, *5*, (1): 11–22.

Van Soest, J and Kortleve, P (1999) "The influence of maltodextrins on the structure and properties of compression-molded starch plastic sheets" *Journal of Applied Polymer Science*, *74*, (9): 2207–2219.

Villermaux, E, Pistre, V and Lhuissier, H (2013) "The viscous Savart sheet" *Journal of Fluid Mechanics*, *730*, 607–625.

Villiers, MM de, Eeden, CM van, Liebenberg, W, Song, M, Kolling, WM and Caira, MR (2004) "Structural characterization, physicochemical properties, suspension stability, and adsorption properties of four solid forms of amitraz" *Journal of agricultural and food chemistry*, *52*, (24): 7362–7369.

Walbrugh, L (2007) "Amitraz Solid Dosage Form" Master's Dissertation, University of Pretoria.

Wang, J, Tan, Z, Peng, J, Qiu, Q and Li, M (2016) "The behaviors of microplastics in the marine environment" *Marine Environmental Research*, *113*, 7–17.

Wang, Q and O'Hare, D (2012) "Recent advances in the synthesis and application of layered double hydroxide (LDH) nanosheets" *ChemicalRreviews*, *112*, (7): 4124–4155.

Wang, S, Li, C, Copeland, L, Niu, Q and Wang, S (2015) "Starch retrogradation: A comprehensive review" *Comprehensive Reviews in Food Science and Food Safety*, *14*, (5): 568–585.

Wang, S, Wang, J, Yu, J and Wang, S (2016) "Effect of fatty acids on functional properties of normal wheat and waxy wheat starches: A structural basis" *Food Chemistry*, *190*, 285–292.

Wootton, M and Bamunuarachchi, A (1979) "Application of differential scanning calorimetry to starch gelatinization. I. Commercial native and modified starches" *Starch-Stärke*, *31*, (6): 201–204.

Xia, H, Li, Y and Gao, Q (2016) "Preparation and properties of RS4 citrate sweet potato starch by heat-moisture treatment" *Food Hydrocolloids*, *55*, 172–178.

Yoo, SH and Jane, Jl (2002) "Structural and physical characteristics of waxy and other wheat starches" *Carbohydrate Polymers*, *49*, (3): 297–305.

Yu, L and Christie, G (2005) "Microstructure and mechanical properties of orientated thermoplastic starches" *Journal of Materials Science*, *40*, (1): 111–116.

Yu, L and Christie, G (2001) "Measurement of starch thermal transitions using differential scanning calorimetry" *Carbohydrate Polymers*, *46*, (2): 179–184.

Zobel, H (1988) "Molecules to granules: a comprehensive starch review" *Starch-Stärke*, *40*, (2): 44–50.